RESEARCH ON ELECTRICALLY AND THERMALLY DRIVEN SPIN-DEPENDENT TRANSPORTS IN FERROMAGNETIC/NONMAGNETIC HYBRID NANOSTRUCTURES

胡, 少杰

https://doi.org/10.15017/1500745

RESEARCH ON ELECTRICALLY AND THERMALLY DRIVEN SPIN-DEPENDENT TRANSPORTS IN FERROMAGNETIC/NONMAGNETIC HYBRID NANOSTRUCTURES

By
Shaojie Hu

SUBMITTED IN PARTIAL FULFILLMENT OF THE
REQUIREMENTS FOR THE DEGREE OF
DOCTOR OF PHILOSOPHY
AT
KYUSHU UNIVERSITY
FUKUOKA, JAPAN
DECEMBER 22, 2014

KYUSHU UNIVERSITY

GRADUATE SCHOOL OF INFORMATION SCIENCE AND ELECTRICAL ENGINEERING

The undersigned hereby certify that they have read and recommend to the Faculty of Graduate Studies for acceptance a thesis entitled "**Research on electrically and thermally driven Spin-dependent transports in ferromagnetic/nonmagnetic hybrid nanostructures**" by **Shaojie Hu** in partial fulfillment of the requirements for the degree of **Doctor of Philosophy**.

Dated: December 22, 2014

Examing Committee:

Prof. Takashi Kimura, Supervisor

Prof. Tanemasa Asano

Prof. Kimihide Matsuyama

KYUSHU UNIVERSITY

Date: **December 22, 2014**

Author: **Shaojie Hu**

Title: **Research on electrically and thermally driven Spin-dependent transports in ferromagnetic/nonmagnetic hybrid nanostructures**

Department: **Graduate School of Information Science and Electrical Engineering**

Degree: **Ph.D.** Convocation: Year:

Permission is herewith granted to Kyushu University to circulate and to have copied for non-commercial purposes, at its discretion, the above title upon the request of individuals or institutions.

Signature of Author

To My Family

Table of Contents

Table of Contents **v**

List of Figures **viii**

Abstract **xiv**

Acknowledgements **xvi**

1 Introduction **1**
1.1 Background 1
1.2 Outline 2

2 Basic theory of electrically and thermally driven charge and spin transport **9**
2.1 Introduction 9
2.2 Electrically driven charge transport 9
2.2.1 Charge current and electrochemical potential 9
2.2.2 Anisotropic magnetoresistance 10
2.2.3 Anomalous Hall effect 11
2.3 Thermally-driven charge transport 12
2.3.1 Seebeck effect 12
2.3.2 Anomalous Nernst effect 13
2.4 Electrically driven spin transport 14
2.4.1 Spin dependent conductivity 14
2.4.2 Spin diffusion equation 14
2.4.3 Electrically driven spin accumulation 16
2.4.4 Detection of spin accumulation 17
2.5 Thermally driven spin transport 19
2.5.1 Spin dependent Seebeck coefficient 19
2.5.2 Thermally driven spin accumulation and detection 19

3 Device fabrication and transport measurement **24**
3.1 Introduction . . . 24
3.2 Device fabrication process . . . 26
3.3 Structure observation . . . 27
3.4 Transport measurement setup . . . 28
3.4.1 Lock-in setup . . . 28
3.4.2 DC bias current dependent measurement . . . 29
3.4.3 Evaluation of resistance for junction interface and ferromagnetic wires 30

4 Spin transport in conventional Py/Cu LSVs **32**
4.1 Introduction . . . 32
4.2 DC bias current dependence of spin signal in Py/Cu LSVs . . . 33
4.2.1 Geometry of the evaluated device . . . 33
4.2.2 Results and Discussion . . . 35
4.2.3 Additional evidence for the anomalous Nernst effect . . . 40
4.3 Summary . . . 41

5 Spin transport in CoFeAl/Cu LSVs **45**
5.1 Introduction . . . 45
5.2 Evaluation of CoFeAl thin film . . . 46
5.3 Electrically driven spin injection in CoFeAl/Cu LSVs . . . 48
5.3.1 Influence of interface in the CFA/Cu LSVs . . . 48
5.3.2 Evaluation of the spin polarization of CoFeAl . . . 49
5.4 DC bias current dependence of spin signal in CoFeAl/Cu LSVs . . . 51
5.5 Summary . . . 56

6 Thermally driven spin transport **59**
6.1 Introduction . . . 59
6.2 Conceptual figures of thermally driven spin injection . . . 60
6.3 Evaluation of thermal spin injection . . . 62
6.3.1 Evaluation of spin dependent Seebeck coefficient . . . 62
6.3.2 Numerical simulation of temperature profile . . . 66
6.3.3 Confirmation of detected thermal spin signal without electrical spin injection contribution . . . 66
6.3.4 Thermal spin injection in LSV with different materials . . . 67
6.3.5 Temperature evaluation of thermal spin signal . . . 69
6.4 Detection of the magnetic orientation by thermal spin current . . . 71
6.4.1 Geometry of device . . . 71
6.4.2 Results and discussion . . . 71
6.5 Summary . . . 76

7 Novel LSV structures for giant pure spin current generation 80
7.1 Introduction 80
7.2 Multi-terminal lateral spin valves 81
7.2.1 Multi-terminal lateral spin valve with Py injectors 81
7.2.2 Multi-terminal lateral spin valve with CoFe injectors 83
7.2.3 Multi-terminal lateral spin valve with CoFeAl injectors 85
7.3 Nanopillar based lateral spin valves 87
7.3.1 Fabrication of Nanopillar with different materials 87
7.3.2 Evaluation of nonlocal spin transport 88
7.4 Summary 91

8 Conclusion 95

List of Figures

1.1 Structure of this thesis. 5

2.1 (a) Anisotropic magnetoresistance measurement. (b) Resistance as a function of sweeping external field. Blue curve corresponds to the resistance of current parallel to magnetization state. While the red curve corresponds to the resistance of current perpendicular to magnetization state. 11
2.2 Illustration of Anomalous Hall effect 12
2.3 Illustration of Seebeck effect. 13
2.4 Illustration of Anomalous Nernst effect in ferromagnet. 14
2.5 Illustration of the spin dependent conductivity.[5] 15
2.6 Schematic of the spin chemical potential distribution under a constant current flowing F/N transparent interface 16
2.7 (a) Illustration of generation of pure spin current driven by electrical current. (b) One typical non-local spin signal was measured in LSV 18
2.8 Illustration of thermal spin accumulation. The spin dependent chemical potential has been off set by contribution of conventional seebeck effect 20

3.1 Flow diagram of the experimental process. 25
3.2 SEM image of one typical lateral spin valve. 28
3.3 Schematic of lock-in measurement system. 29
3.4 Probe configuration of the crossing junction resistance measurement. . . . 30

4.1 (a) Scanning electron microscope (SEM) image of the measured LSV and the probe configuration for the nonlocal spin valve measurement using the dual spin injection. (b) Schematic illustration of the temperature distribution in the device under the nonlocal spin injection and the temperature gradient in the vicinity of the nonlocal detecting junction. 34
4.2 Field dependencies of the nonlocal spin valve signal under various dc bias currents, (a) +3.5 mA, (b) 0 mA, and (c) -3.5mA. Solid and dotted curves correspond to the forward and backward field sweeps, respectively. Py . . . 35
4.3 Bias current dependencies of (a) R_{S},(b) ΔR_{AS},and (c) $R_{\mathrm{Avg.}}$ Solid lines are obtained by fitting the plots on the parabolic or linear dependence. 37
4.4 (a) Schematic illustration of the nonlocal spin valve measurement for the interchanged probe configura- tion. Observed nonlocal spin valve signals for (b) +2.5 mA and (c) -2.5 mA 39
4.5 Transverse field dependence of the non- local signal under the bias curren- t injection with the magnitude of +5 mA. The inset shows the schematic illustration for the measurement with the probe configuration 40

5.1 M-H curve observed for CoFeAl thin films with different composition. . . . 46
5.2 (a)AMR measurement for well defined CoFeAl wire. (b)FMR spectrum in CFA film with thickness of 30 nm under magnetic field of 225 Oe 48
5.3 (a) The typical electron spin signal for device A. (b) The typical electron spin signal for device B. 49
5.4 Evaluation of electrical spin polarization. (a) Scanning electron microscope image of the CoFeAl (CFA)/Cu lateral spin valve (LSV) in the present study and a schematic figure of the nonlocal spin valve measurement to evaluate the electrical spin polarization. (b) Room temperature nonlocal spin signals for the CoFeAl/Cu (black curve) and permalloy (Py)/Cu (red curve) LSVs at the centercenter distance L of 200nm. The dotted and solid curves denote the forward and backward field sweeps, respectively. (c) Room-temperature spin signal as a function of interval distance (L) for CoFeAl/Cu (solid dots) and Py/Cu (solid triangles) LSVs. The red lines are fitted curves based on Eq. (2.4.7) with λ_{Cu}=450 nm at room temperature. 50

5.5 (a) $\sim$ (c) The detected first harmonic spin signal under various DC bias current by sweeping external filed under the small AC current. The insets show the value of DC bias currents. (d) First harmonic spin signal $R_{\mathrm{S}}^{1\mathrm{f}}$ as a function of DC bias current (I_{dc}) in CFA/Cu LSV with the interval distance 400 nm. The solid line is obtained by fitting Eq.(5.4.3) 53

5.6 (a) $\sim$ (c) The second harmonic voltage spin signal under various AC bias current for the same CFA/Cu LSV. The insets are the exactly value of AC currents. (d-e) The second harmonic spin voltage $V_{\mathrm{S}}^{2\mathrm{f}} = V_{\mathrm{P}}^{2\mathrm{f}} - V_{\mathrm{AP}}^{2\mathrm{f}}$ and base voltage of second harmonic $V_{\mathrm{B}}^{2\mathrm{f}} = (V_{\mathrm{P}}^{2\mathrm{f}} + V_{\mathrm{AP}}^{2\mathrm{f}})/2$ as a function of AC bias current (I_0), respectively. The solid red curves are corresponding to the parabolic fitting. 55

5.7 First harmonic spin signal $R_{\mathrm{S}}^{1\mathrm{f}}$ as a function of DC bias current (I_{dc}) in Py/Cu LSV. The solid blue line is obtained by fitting Eq.(5.4.3). The inset shows the typical lateral spin signal under 0 DC bias current in this LSV device. 55

6.1 Conceptual figures of highly efficient thermal spin injection. (a) Schematic illustration of the spin-dependent DOSs for a conventional ferromagnetic metal at high (left) and low (right) temperatures. Both the up-spin and down-spin electrons diffuse from the left-hand side (the high temperature) to the right-hand side (the low temperature). (b) Charge and spin current flow in the conventional ferromagnet/nonmagnet junction under the temperature gradient. The generation and injection efficiencies are quite low because both the up-spin and down-spin electrons move along the same direction. (c) Schematic illustration of the spin-dependent DOSs for a highly spin-polarized ferromagnetic metal at high (left) and low (right) temperatures. The small DOS for the minority spin around the Fermi level reverses the moving direction of the electrons under the temperature gradient. As a result, the moving direction for the down-spin electrons is opposite that for the up-spin electrons. (d) Charge and spin current flow in the highly spin-polarized ferromagnet/nonmagnet junction under the temperature gradient. The spin current is efficiently generated and injected into the nonmagnet . 61

6.2 Giant spin accumulation due to thermal spin injection. (a) Schematic illustration of the thermal spin injection and detection using the LSV structure. Thermally excited spin current is generated by flowing a large current in a ferromagnetic wire (F1), which is then detected by the ferromagnetic detector (F2) with the second harmonic voltage detection technique. (b) Numerically simulated result of the spatial distribution of the temperature around the C-FA/NM injecting junction under a large current of 0.78 mA. Here, the current value corresponds to the root-mean square. It is clearly confirmed that the Joule heating induced by the current flow in the ferromagnetic wire produces a temperature gradient across the FM/NM interface. (c) Field dependence of second harmonic voltage under the thermal spin injection for CoFeAl/Cu LSV (black line) with a 200 nm interval distance under a bias current of 0.78 mA, together with the second harmonic signal for the Py/Cu LSV with the same sample dimensions under a bias current of 1.08 mA. The asymmetric field dependence is induced by the anomalous Nernst effect in the Py detector. (d) Bias current dependence of the second harmonic spin voltage V^{2f} for the CFA/Cu LSV. The red line is the fitting curve assuming the parabolic dependence. (e) The thermal spin signal, defined as $\Delta R_s^{2f} = \Delta V_s^2/I^2$, as a function of interval distance L for CFA/Cu LSV at room temperature. The solid red line is a fitted curve based on Eq. (2) assuming λ_{Cu}=450 nm. . . . 63

6.3 Numerically simulated spatial distributions of the temperature in the whole device (a) and in the vicinity of the CFA/Cu junction (b) under the bias current of 0.78 mA. The temperature gradient from CFA1 to Cu is clearly confirmed 65

6.4 Thermal spin resistance under the thermal spin injection. (a) The first-harmonic spin valve signal under the thermal spin injection together with the schematic of the measurement probe configuration for CoFeAl/Cu lateral spin valve. Here, the interval distance between ferromagnetic wires is 300nm and (b) those under the reversed current injection. 67

6.5 Thermal spin signal in the lateral spin valve consisting of Py and CFA wires which are separated by 500 nm between center to center. (a) Thermal spin signal observed for injector of CFA and detector of Py as shown in the right schematic of measurement configuration. (c) The thermal spin signal with measurement configuration for injector of Py and detector of CoFeAl. . . . 68
6.6 Temperature evaluation of thermal spin signal. (a) Thermal spin signal as a function of external field at 5.5 K under bias current of 0.78 mA both for CFA/Cu and Py/Cu LSVs. (b) Temperature dependence of thermal spin resistances for Py/Cu and CFA/Cu LSVs, respectively. 70
6.7 SEM image with the schematic of present LSV structure consisting of 3 CFA wires. 71
6.8 Typical electrical spin signal with various measurement configurations in the left. 73
6.9 (a)Measurement configuration and the schematic of thermal spin injection for this device. (b) Second harmonic voltage as a function of sweeping field. 74
6.10 Schematic configuration and thermal spin signal of detection the magnetization of embedded CFA dot. 75

7.1 (a) SEM image of the multi-terminal spin injection device. (b) Spin signal at near zero bias for each Py injectors. (c) Schematics for signal, double, triple and quadruple spin injections. (d) DC bias current dependence of the normalized spin signals for each injections. 82
7.2 (a) SEM image of the multi-terminal spin injection device with CoFe injectors. (b) Quadruple spin signal for CoFe and Py injectors at room temperature. (c) Spin signal at 4.6K for CoFe injectors. 84
7.3 (a) SEM image of Multi-terminal lateral spin valve with CoFeAl injectors and the measurement configuration. (b) Typical nonlocal spin signal at room temperature and 2.4 K. 86
7.4 (a) Illustration of the switching of magnetization by spin transfer torque of pure spin current. (b) Resistance jumping as sweeping DC bias current at the temperature of 2.4 K. DC bias current is started to sweep from zero to positive value of 10 mA and go back to negative 10 mA, then reduce to zero. 87

7.5 Fabrication process and measurement method (a) Top view of the resist pattern. (b) Schematic of shadow evaporation in a view of the crossing section. (c) SEM of the closed located ribbons. (d) SEM image of one device (e) Schematic of the measurement configuration 89
7.6 (a) Typical spin signal for the present device measured at 295 K (red) and 35 K (blue). (b) The spin signal as a function of temperature. (c) Switching field as a function of temperature for CFA (Solid black dot) and Py (Solid red dot) respectively. 90
7.7 The illustration of the spin reservoir effect in the pillar based lateral spin valve. 91

Abstract

Spintronics initiated by the discovery of the giant magneto resistance effect (GMR) has been considered as the core domain in the next generation nano-electronics owing to their numerous potential applications such as nonvolatile memory and logic device with low power consumption. Moreover, unique characteristics originating from the quantum nature of spin degree of freedom provide a lot of fascinating fundamental physics and surprising possibilities. Especially, the concept of the spin current, a flow of the spin angular momentum, opens up the innovation in the operation of the spintronic devices and provides a new aspect in the charge and spin transport in a solid state.

Laterally configured ferromagnetic/nonmagnetic multi-terminal hybrid structures enable us to create a spin current without accompanying a charge current, namely pure spin current by mean of nonlocal spin injection technique. The pure spin current efficiently transmits the spin information with the absence of the Joule heating and allows us to observe novel spin-related phenomena such as spin Hall effect and spin Seebeck effect owing to the reduction of the spurious signals induced by the charge current. However, the application feasibility of the pure spin currents was quite low because of their extremely low generation efficiency in spite of its high energy efficiency for propagating the spin information. Thus, the drastic enhancement in the generation efficiency of the pure spin current should be achieved. For this purpose, in the present thesis, novel methods for the efficient generation and manipulation of the pure spin current have been developed.

Firstly, the existence of the thermal current was confirmed even in nonlocally induced pure spin current. The thermal current was found to induce the large thermoelectric effect under the high bias current in the nonlocal configurations using the conventional ferromagnetic electrodes. Secondly, a significant enhancement of the efficiency in the electrical

generation of the pure spin current has been demonstrated by using spin-polarized ferromagnetic electrodes based on polycrystalline CoFeAl. Moreover, the CoFeAl electrodes were found to generate the pure spin current by using the heat rather than using the electricity because of its favorable band structure for the thermal spin injection. Then, by mixing the electrical and thermal generation of the pure spin current, a highly efficient generation of the pure spin current has been achieved. In addition, by extending the efficient thermal spin injection, a novel method for detecting the spin direction has been demonstrated. Finally, in order to generate a giant pure spin current, two methods, using multi-terminal spin injectors and nano-pillar-shaped spin injector, have been demonstrated.

These innovative demonstrations open a new route for spin-device integration and its applications, leading to the realization of functional spin devices utilizing pure spin currents with an extremely low power consumption.

Acknowledgements

I would like to acknowledge all the people who gave me the fruitful, helpful and valuable comments, discussions, collaborations and continuous support during the whole PhD research period. This thesis could not be made possible without the help of many people.

First, I would like to address my sincere gratitude to all the members in the defense committee, Prof. Tanemasa Asano, Prof. Kimihide Matsuyama and Prof. Takashi Kimura for all their contributions, advices and valuable comments. Especially, I would like to express my gratitude to my supervisor Takashi Kimura for giving me the chance to do a PhD in his research group and for always appreciating the work which have been done by me. I am grateful to him not only for his valuable suggestions and constant support during the whole period of my research, but also for his enthusiasm and passion for perusing the fascinating physical science. Besides, he also presents friendly research environment and advanced scientific equipment for experimental research regarding to spintronics. At the beginning, it takes time for me to learning all the experimental equipment. But I managed to use them quickly with the patiently guidance and help of Prof. Kimura and other group members.

Speaking of the equipment, I would like to thank our excellent technician Kenjo-San who helps to maintain and improve the equipment. He is also a fashion guy and interested into all kinds of new electronic products. I admire his attitude to life and want to be a person like him when I am getting old.

Besides, I am also thankful to our previous assistant professor Satoshi Yakata for his guidance on learning the experimental equipment and analysis software at the beginning of my PhD research. I would also like to address my special thanks to our current assistant professor Kohei Ohnishi for constructing the low temperature measurement system so that it enables temperature controlling detection which is a part of important contribution for my thesis.

I also want to mention that we have the most wonderful secretary, who is a sweet and friendly young woman. She always offers me help for my living in Japan and brings delicious snacks for us.

I am grateful to all the other members (especially the funny guy Tastuya Nomura) in my group for their support on my experiment and living.

It is a pleasure to thank to all the other (former) group members. I thank M. Miyata, S. Nonoguchi, Kohei Kiseki and other members for teaching me to operate the fabrication machines and helping in living. I also send my thanks to my cooperators S.R. Bakaul and Congpu Mu.

Besides, special thanks Prof. K. Matsuyama and assistant professor T. Tanaka for the using of VSM system. I also would like to thank Prof. Miyao and Associate Prof. Sadoh and his lab members for helping me to do EDX for my samples.

Here I also want to acknowledge that my living in Japan was supported by the China Scholarship of Council for Young Scientist. Thanks to this great scholarship, I could have the chance to study in Japan for my PhD whereby I gained abundant unique knowledge. What's more, it enriches my vision to see the world and specifically to the frontier research of spintronics.

I am grateful to my mother for her patience and understanding. Without her support, this work would never have come into existence (literally). And most of all, I thank my wife Sady for her support, encouragement, patience and unwavering love. I was amazed by her willingness to proof read the countless pages and the grammar check for my work.

I could not have completed my research without the support of all these wonderful people.

Fukuoka, Japan Shaojie Hu
December 8, 2014

Chapter 1

Introduction

1.1 Background

The discovery of giant magneto resistance (GMR) effect in 1988 done by A. Fert and P. Grünberg [1, 2], who are the Nobel Prize winners in 2007, opens up an emerging field of spintronics, in which the spin degree of freedom plays a main role in the electron transports instead of the electron charge. The birth of spintronics enables us not only to develop magnetic storage device but also to propose an innovative micro and/or nano electrical devices such as magnetic random access memory (MRAM) and spin transistor [3, 4]. The performance of these novel devices has been extensively improved by the demonstration of the room-temperature tunnel magneto resistance (TMR) [5, 6] and was further enhanced by the discovery of the giant TMR effect [7–9]. Apart from the spin-dependent transports, the concept of the spin-transfer torque has been verified in 1998 and 1999 [10, 11]. These innovative demonstrations open up a new paradigm for controlling the magnetization orientation without the use of the magnetic field. Thus, recent development in spintronics requires good understanding of spin transfer torque of spin current.

However,the charge current and spin current are mixed together in the most common structures in the spintronics, such as vertical heterostructures, which regulates our understanding regards to the spin-transfer torque effect. The pure spin current, which is a flow of

spin angular momentum without accompanying a charge current offers a route to efficiently transmit the spin information and observe novel spin-related phenomena. One approach which can create the pure spin current by using non-local geometry in lateral spin valve was first reported by Johnson and Silsbee in 1985 [12]in micro-structure. The method had not drawn more attention until the developing of nano fabrication technology from the early of 21 Century. Prof. Van Wees' group in Groningen reported the generation and detection of pure spin current in all-metal lateral spin valve at room temperature in 2001 [13]. 6 years later, Prof. Otani's group in Tokyo realized the switching of magnetization in nano-particle using the spin transfer torque effect of pure spin current in lateral spin valve at low temperature [14]. Spin transfer torque of pure spin current induced in non-local lateral spin valve structures has attracted great interest both in the fundamental study and technological application. So the application of pure spin current becomes promising in the next generation device [15–17]. So far, the efficiency of generating pure spin current is quite low at room temperature. Therefore, it's a urgent issue to enhance the generation efficiency of pure spin current.

1.2 Outline

This thesis aims to efficiently generate and manipulate pure spin current. The experiment results are divided into four chapters and located between Chapter 3 and Chapter 8 as shown in flow diagram in figure 1.1. In the list below, a briefly summarization for each chapter is given:

- Chapter 1 provides the introduction and motivation of the thesis.
- Chapter 2 reviews the basic theory of the electrically and thermally driven charge and spin transport in metal.

- Chapter 3 firstly briefly introduces the fabrication techniques of conventional lateral spin valves. Then, the measurement setup will be introduced for evaluating the transport of charge and spin.

- Chapter 4 systematically studies the influence of the heat current in conventional Py/Cu LSVs by evaluating the bias current dependence of spin signal. The large current was found that it not only reduces the generation efficiency of the pure spin current but also induces unconventional asymmetric field dependence of nonlocal spin signal due to anomalous Nernst effect. The developed multi-terminal and pillar based LSVs can improve the generation efficiency and prevent the Anomalous Nernst Effect. But the magnitude of pure spin current is still low using the conventional ferromagnet. It gives rise to an urgency for searching high performance materials.

- Chapter 5 is devoted to the discussion of the excellent ferromagnetic material CoFeAl. Here, special attention was paid to seeking promising CoFe-based ferromagnetic materials with higher spin injection efficiency by using simple deposition technique (electron beam evaporation deposition). An excellent ferromagnetic material CoFeAl was obtained, which enables 10 times larger spin signal in the CFA LSV than that with Py, indicating high efficient generation of pure spin current. Surprisingly, the spin signal was found to enhance under high bias current. This had been well explained by the mixing of electrically and thermally driven spin injection. It's naturally to ask how large of the thermally driven spin injection.

- Chapter 6 focuses on the evaluation of thermally driven spin injection. Firstly, The spin current injection was investigated by only using the heat current by employing the optimized CoFeAl ferromagnetic materials. A heat generated spin voltage with approximately 100 times larger than the conventional ferromagnetic injector was

successfully obtained under room temperature using CoFeAl electrodes. This innovative demonstration may open a new route for spin-device integration and its future applications.

- Chapter 7 discusses the spin transport properties by employing novel structures such as multi-terminal LSVs and Pillar-based LSVs with excellent material. The giant pure spin current has been achieved in the multi-terminal LSVs. The switching of the nanomagnet have been demonstrated by spin transfer torque of giant pure spin current.

- Chapter 8 closes this thesis with the conclusion.

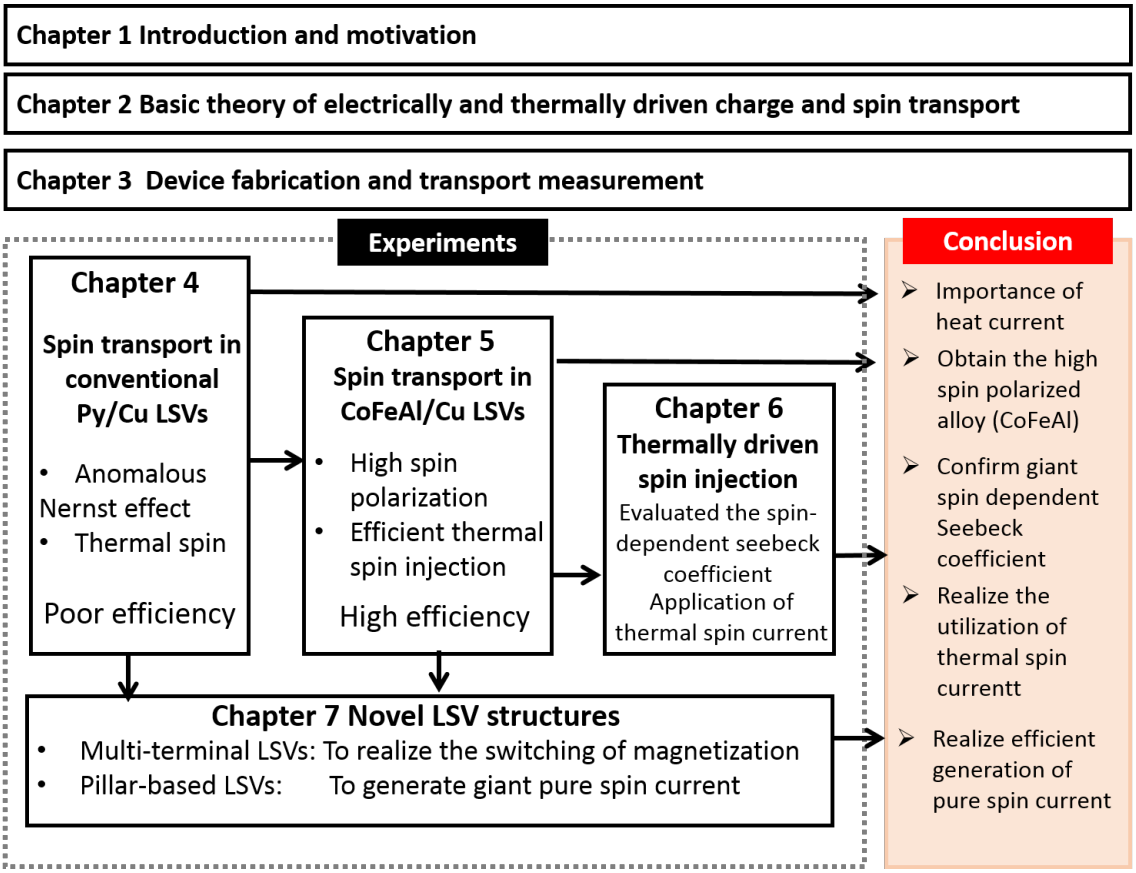

Figure 1.1: Structure of this thesis.

Bibliography

[1] M. N. Baibich, J. M. Broto, A. Fert, F. Nguyen Van Dau, and F. Petroff. Giant Magnetoresistance of (001)Fe/(001)Cr Magnetic Superlattices. *Physical Review Letters*, 61(21):2472–2475, November 1988.

[2] G. Binasch, P. Grünberg, F. Saurenbach, and W. Zinn. Enhanced magnetoresistance in layered magnetic structures with antiferromagnetic interlayer exchange. *Physical Review B*, 39(7):4828–4830, March 1989.

[3] S. A. Wolf, D D Awschalom, R. A. Buhrman, J M Daughton, S von Molnár, M L Roukes, A. Y. Chtchelkanova, and D M Treger. Spintronics: a spin-based electronics vision for the future. *Science (New York, N.Y.)*, 294(5546):1488–95, November 2001.

[4] Igor Žutić and S. Das Sarma. Spintronics: Fundamentals and applications. *Reviews of Modern Physics*, 76(2):323–410, April 2004.

[5] J. S. Moodera, Lisa R. Kinder, Terrilyn M. Wong, and R. Meservey. Large Magnetoresistance at Room Temperature in Ferromagnetic Thin Film Tunnel Junctions. *Physical Review Letters*, 74(16):3273–3276, April 1995.

[6] T. Miyazaki and N. Tezuka. Giant magnetic tunneling effect in Fe/Al2O3/Fe junction. *Journal of Magnetism and Magnetic Materials*, 139(3):L231–L234, January 1995.

[7] S. S. P. Parkin, K. P. Roche, M. G. Samant, P. M. Rice, R. B. Beyers, R. E. Scheuerlein, E. J. OSullivan, S. L. Brown, J. Bucchigano, D. W. Abraham, Yu Lu, M. Rooks, P. L.

Trouilloud, R. a. Wanner, and W. J. Gallagher. Exchange-biased magnetic tunnel junctions and application to nonvolatile magnetic random access memory (invited). *Journal of Applied Physics*, 85(8):5828, 1999.

[8] S Tehrani, J.M. Slaughter, E Chen, M. Durlam, J Shi, and M. DeHerren. Progress and outlook for MRAM technology. *IEEE Transactions on Magnetics*, 35(5):2814–2819, 1999.

[9] S. Tehrani, B. Engel, J.M. Slaughter, E. Chen, M. DeHerrera, M. Durlam, P. Naji, R. Whig, J. Janesky, and J. Calder. Recent developments in magnetic tunnel junction MRAM. *IEEE Transactions on Magnetics*, 36(5):2752–2757, 2000.

[10] M. Tsoi, a. Jansen, J. Bass, W.-C. Chiang, M. Seck, V. Tsoi, and P. Wyder. Excitation of a Magnetic Multilayer by an Electric Current. *Physical Review Letters*, 80(19):4281–4284, May 1998.

[11] E. B. Myers, D.C. Ralph, J.A. Katine, R.N. Louie, and R.A. Buhrman. Current-Induced Switching of Domains in Magnetic Multilayer Devices. *Science*, 285(5429):867–870, August 1999.

[12] Mark Johnson and R. H. Silsbee. Interfacial charge-spin coupling: Injection and detection of spin magnetization in metals. *Physical Review Letters*, 55(17):1790–1793, October 1985.

[13] F J Jedema, a T Filip, and B J van Wees. Electrical spin injection and accumulation at room temperature in an all-metal mesoscopic spin valve. *Nature*, 410(6826):345–8, March 2001.

[14] T. Kimura, Y. Otani, and J. Hamrle. Switching Magnetization of a Nanoscale Ferromagnetic Particle Using Nonlocal Spin Injection. *Physical Review Letters*, 96(3):1–4, January 2006.

[15] Tao Yang, Takashi Kimura, and Yoshichika Otani. Giant spin-accumulation signal and pure spin-current-induced reversible magnetization switching. *Nature Physics*, 4(11):851–854, October 2008.

[16] J. Z. Sun, M. C. Gaidis, E. J. OSullivan, E. a. Joseph, G. Hu, D. W. Abraham, J. J. Nowak, P. L. Trouilloud, Yu Lu, S. L. Brown, D. C. Worledge, and W. J. Gallagher. A three-terminal spin-torque-driven magnetic switch. *Applied Physics Letters*, 95(8):083506, 2009.

[17] Behtash Behin-Aein, Deepanjan Datta, Sayeef Salahuddin, and Supriyo Datta. Proposal for an all-spin logic device with built-in memory. *Nature nanotechnology*, 5(4):266–70, April 2010.

Chapter 2

Basic theory of electrically and thermally driven charge and spin transport

2.1 Introduction

Manifestation of the conduction electrons in a solid state is one of the most important aspects for the electrical transports in the condensed matter physics. It is well known that an electron, which is a subatomic particle, has an elementary negative electric charge and an intrinsic spin angular momentum. While the charge of the electron is the basis of the electricity, the spin of the electron is the origin of the magnetism. In ferromagnetic metals, these two quantities interact each other and induce the intriguing phenomena through the spin-dependent scattering. Moreover, the heat in the ferromagnet is found to induce the spin-dependent phenomena. In this chapter, the basic theory for the electrically-driven and thermally-driven charge and spin tranposrts are introduced.

2.2 Electrically driven charge transport

2.2.1 Charge current and electrochemical potential

The total density of current $\boldsymbol{j}$ in conductors includes drift current $\boldsymbol{j}_{\mathrm{drift}}$ which is driven by the electric field $\boldsymbol{E}$ and diffusion current $\boldsymbol{j}_{\mathrm{diffusion}}$ which arises from the gradient of local

electron density deviation from the equilibrium ($\nabla\delta n$).

$$\boldsymbol{j} = \boldsymbol{j}_{\text{drift}} + \boldsymbol{j}_{\text{diffusion}} = \sigma\boldsymbol{E} - eD\nabla\delta n, \tag{2.2.1}$$

where, σ and D are the electrical conductivity and diffusion constant. According to $\delta n = N\delta\varepsilon$ (N is the density of states in the subband and $\delta\varepsilon$ is the shift in the chemical potential of electrons from its equilibrium value), Einstein relation $\sigma = e^2ND$ in metal,

$$\boldsymbol{j} = -\frac{\sigma}{e}\nabla(\delta\varepsilon + e\Phi), \tag{2.2.2}$$

Where Φ is electrical potential. Therefore, the current density can be expressed by the defined electrochemical potential (ECP) $\mu = \delta\varepsilon + e\Phi$,

$$\boldsymbol{j} = -\frac{\sigma}{e}\nabla\mu, \tag{2.2.3}$$

This relation expresses the fact that the driving force for the total current is the gradient of the eletrochemical potential.

2.2.2 Anisotropic magnetoresistance

Anisotropic magnetoresistance (AMR) which was discovered by Thomson in 1856 explains electrical resistance in ferromagnet depends on the angle (θ) between the direction of electric current (**I**) and direction of magnetization (**M**) as shown in figure 2.1 (a). By defining the resistances $R_{\parallel}$ for current parallel to the magnetization, $I \parallel M$, and $R_{\perp}$ for $I \perp M$, the AMR effect is defined as

$$AMR = \frac{\Delta R}{R_{\text{avg.}}} = \frac{R_{\parallel} - R_{\perp}}{(R_{\parallel} + 2R_{\perp})/3} \tag{2.2.4}$$

For example, the obtained AMR for NiFe(Py) thin film was shown in figure 2.1(b). The resistance is highest when the magnetization M is parallel to the direction of current

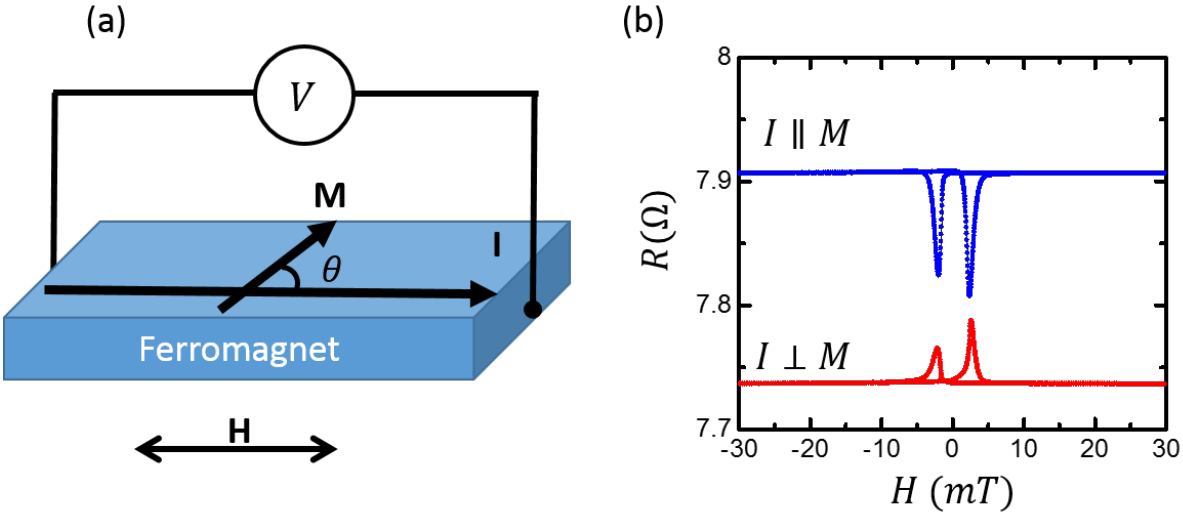

Figure 2.1: (a) Anisotropic magnetoresistance measurement. (b) Resistance as a function of sweeping external field. Blue curve corresponds to the resistance of current parallel to magnetization state. While the red curve corresponds to the resistance of current perpendicular to magnetization state.

$R_{\parallel}$ and lowest when it is perpendicular $R_{\perp}$. The AMR ratio is about 2.18% for present Py film using the Eq. (2.2.4).

2.2.3 Anomalous Hall effect

The anomalous Hall effect (AHE) which was discovered in 1881 by Hall explains an addition contribution Hall resistivity is observed in ferromagnetic materials, which depends directly on the magnetization of the material, and is often much larger than the ordinary Hall effect.

The detection of AHE is described as flow: when one current flows in the ferromagnet without magnetic field, one can obtain the static electric field (E) in transverse direction as shown in figure 2.2. The generated electron field is given by the following equation:

$$\mathbf{E} = \rho \mathbf{I} \times \mathbf{M} \tag{2.2.5}$$

Where, ρ is Hall resistivity, $\mathbf{M}$ is the magnetization.

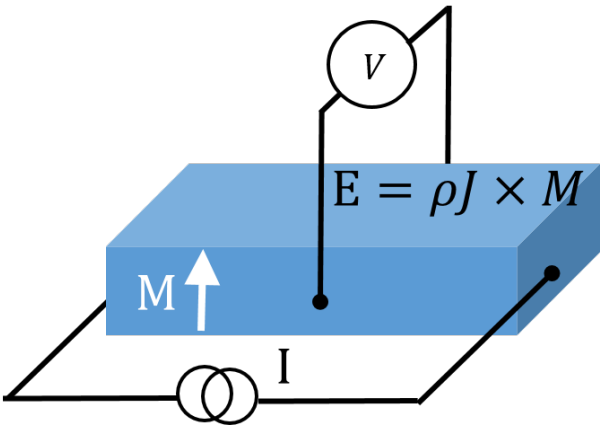

Figure 2.2: Illustration of Anomalous Hall effect

The anomalous Hall effect is an important phenomenon for the charge transport in ferromagnetic materials.

2.3 Thermally-driven charge transport

2.3.1 Seebeck effect

The classical Seebeck effect is the conversion of temperature gradient into a electric voltage in the materials as shown in figure 2.3. The relationship of Seebeck voltage and temperature difference is given by equation:

$$\Delta V = -S\Delta T \tag{2.3.1}$$

Where, S is defined as Seebeck coefficient which is strongly correlated to the band structure around the Fermi level in conductors.

For simple approximation in metals, the Seebeck coefficient can be well described by Mott' formula:

$$S = -eL_0T(\frac{\partial ln\sigma}{\partial E})_{E=E_F} \tag{2.3.2}$$

Where $L_0 = (\pi^2/3)(k_B/e)^2$ is Lorenz constant, σ is the energy dependent conductivity around the Fermi energy E_F.

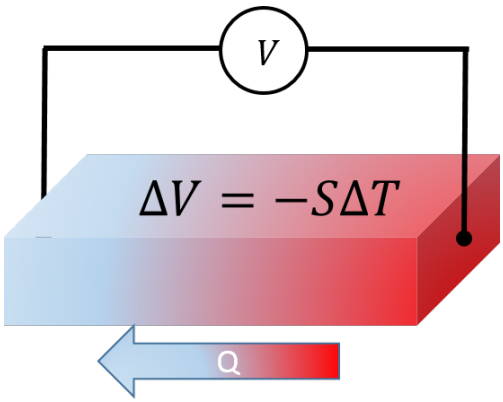

Figure 2.3: Illustration of Seebeck effect.

The Seebeck coefficient is about a dozen of micro volt per Kelvin in conventional ferromagnet at room temperature. And the generated Seebeck voltage which is in a range of micro voltage is comparable to the electrical signal in nano-device. Thus, Seebeck effect becomes inneglectable problem especially in nano structures.

2.3.2 Anomalous Nernst effect

Another well known thermo-electron effect is anomalous Nernst effect (ANE) which describes that a temperature gradient could induce electron field in the direction of perpendicular to temperature gradient and magnetic field direction in ferromagnet as shown in Figure 2.4. The generated electric field is given by the following equation:

$$\mathbf{E} = S_A \nabla T \times \mathbf{M} \tag{2.3.3}$$

Where S_A is defined as the anomalous Nernst coefficient. $\mathbf{M}$ is the magnetization of ferromagnet.

In the experiment of spin related thermal effect, such as spin dependent effect, they always accompany the obstacle of Anomalous Nernst signal[1–3]. It is important to clarify such effect in the thermal spin transparent experiment.

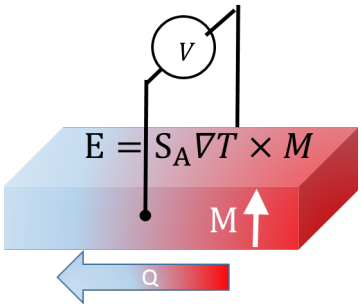

Figure 2.4: Illustration of Anomalous Nernst effect in ferromagnet.

2.4 Electrically driven spin transport

2.4.1 Spin dependent conductivity

The electrical conductivity which is contributed by the number of electrons (n) is proportional to the density of states at Fermi energy in metal. The low conductivity of the transition metals is produced by the strongly scattering of s state electron on the d hole state as shown in figure 2.5. The more d states are available, the stronger is selective spin scattering [4]. Because the density of empty states near E_F is larger for the spin down than the spin up channel, the scattering probability for the spin down is larger, or the conductivity for the spin down is lower. Therefore, the conductivity can be treated as independent for up and down spin states. This indicates the conductivities can be separated to two channels and added in series.

$$\sigma = \sigma_\uparrow + \sigma_\downarrow = ne^2\tau_\uparrow/m_e + ne^2\tau_\downarrow/m_e \tag{2.4.1}$$

2.4.2 Spin diffusion equation

Now, we consider the spin dependent transport. The electrical current density $\boldsymbol{j}_{\uparrow,\downarrow}$ for spin up and down channels is expressed as

$$\boldsymbol{j}_{\uparrow,\downarrow} = -\frac{\sigma_{\uparrow,\downarrow}}{e}\nabla\mu_{\uparrow,\downarrow}, \tag{2.4.2}$$

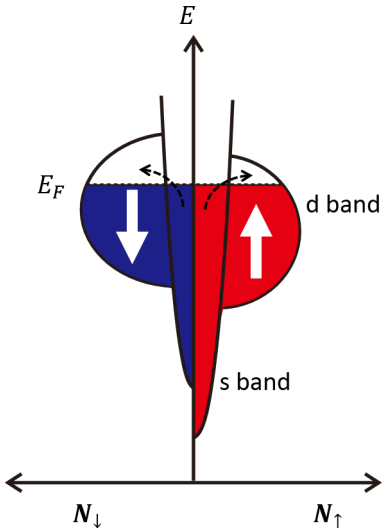

Figure 2.5: Illustration of the spin dependent conductivity.[5]

Where, $\mu_{\uparrow,\downarrow} = \varepsilon_{\uparrow,\downarrow} + e\Phi$ is the spin-dependent electrochemical potential. Here, a charge current $\boldsymbol{j}_c = \boldsymbol{j}_\uparrow + \boldsymbol{j}_\downarrow$ and a spin current $\boldsymbol{j}_s = \boldsymbol{j}_\uparrow - \boldsymbol{j}_\downarrow$. The continuity equations for charge and spin in the steady state are

$$\nabla \boldsymbol{j}_c = 0, \tag{2.4.3}$$

$$\nabla \boldsymbol{j}_s = e\frac{\boldsymbol{n}_\uparrow - \bar{\boldsymbol{n}}_\uparrow}{\tau_{\uparrow\downarrow}} - e\frac{\boldsymbol{n}_\downarrow - \bar{\boldsymbol{n}}_\downarrow}{\tau_{\uparrow\downarrow}}, \tag{2.4.4}$$

Where, $\bar{\boldsymbol{n}}_{\uparrow,\downarrow}$ is the equilibrium carrier density and $\tau_{\uparrow\downarrow}(\tau_{\downarrow\uparrow})$ is the scattering time of an electron from spin state $\uparrow$ ($\downarrow$) to $\downarrow$ ($\uparrow$). The detailed balance principle imposes that $N_\uparrow/\tau_{\uparrow\downarrow} = N_\downarrow/\tau_{\uparrow\downarrow}$, so there isn't net spin scattering in equilibrium. $N_\uparrow(N_\downarrow)$ is the spin dependent density of states at Fermi energy. So one obtains the basic equations for ECP

$$\nabla^2(\sigma_\uparrow\mu_\uparrow + \sigma_\downarrow\mu_\downarrow) = 0, \tag{2.4.5}$$

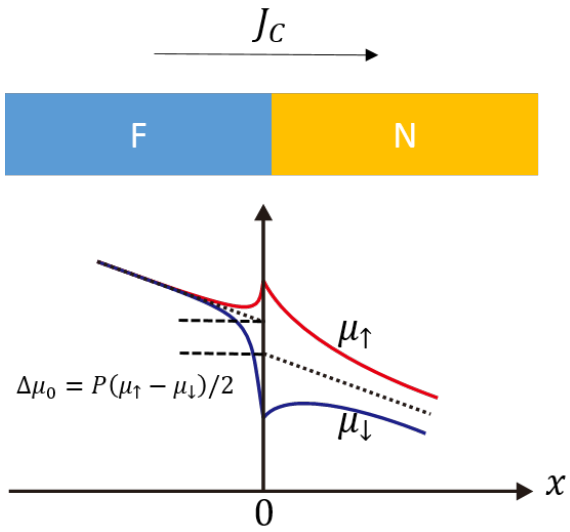

Figure 2.6: Schematic of the spin chemical potential distribution under a constant current flowing F/N transparent interface

$$\nabla^2(\mu_\uparrow - \mu_\downarrow) = \frac{1}{\lambda^2}(\mu_\uparrow - \mu_\downarrow), \tag{2.4.6}$$

Where, $\lambda = \sqrt{D\tau_{sf}}$ is the spin-diffusion length, with the spin-relaxation time τ_{sf} and diffusion constant D, which is given by: $1/\tau_{sf} = 1/\tau_{\uparrow\downarrow} + 1/\tau_{\downarrow\uparrow}, 1/D = (N_\uparrow/D_\downarrow + N_\downarrow/D_\uparrow)/(N_\uparrow + N_\downarrow)$

2.4.3 Electrically driven spin accumulation

If one constant circulate current is applied between the ohmic interface F/N, one charge current with density of $\boldsymbol{j}_c$ flows from F to N along the x direction, as shown on the figure 2.7. The applied current could induce the electrochemical potential difference around the interface for the tow spin channels. The difference of electrochemical potential for up and down spins around the interface is called spin accumulation ($\mu_s = \mu_\uparrow - \mu_\downarrow$) which obeys Eq.(2.4.6) from the non-equilibrium state to equilibrium state in the steady state in the non-magnet.

A splitting of averaged chemical potentials ($\Delta\mu_0$) which can generate a directly detected

voltage will be yielded by solving the continuity equations of the charge and spin currents in a steady state at the interface. The electrical conductivity satisfies the following relationship in Ferromagnetic and nonmagnetic: $\sigma_{\mathrm{F}} = \sigma_{\uparrow} + \sigma_{\downarrow}, \sigma_{\mathrm{N}} = 2\sigma_{\uparrow}^{\mathrm{N}} = 2\sigma_{\downarrow}^{\mathrm{N}}$ and defined the polarization $P = \frac{\sigma_{\uparrow} - \sigma_{\downarrow}}{\sigma_{\uparrow} + \sigma_{\downarrow}}$ in ferromagnetic.

Therefore, the relationship of splitting of averaged chemical potential and the spin accumulation could be obtained at interface as: $\Delta\mu_0 = P(\mu_{\uparrow} - \mu_{\downarrow})/2 = P\mu_s/2$.

2.4.4 Detection of spin accumulation

The spin accumulation information could be evaluated in conventional lateral spin valve as shown in Figure 2.7. When one electron current flows from the F1 to the left side of nonmagnet (N), the accumulation of spins will be built up at the interface and diffuse in tow directions. The diffusion process from the nonequilibrium into the equilibrium state induces the motion of the electrons. Since the chemical potential of up spin is higher in the left side, up spins diffuse towards the right side. On the other hand, down spins chemical potential which is lower in the left side induces the incoming flow of the down spins, opposite to the motion of the up spins. Thus, a pure spin current, which carries the spin angular momentum without electric charges, can be generated in right side of N channel.

The generated pure spin current can be detected by using another ferromagnetic (F2) voltage probe. When the pure spin current is injected into the F2, a splitting of average chemical potential in the F2 is induced because of the spin-dependent conductivity. The sign of the potential splitting depends on the relative angle between the spin direction of the injecting spin current and the magnetization direction. When the direction of the injecting spin is parallel to the majority (minority) spin of the spin detector, the electrostatic potential of the spin detector shifts positively (negatively). Therefore, when the voltage between the ferromagnet and the right-hand side of the nonmagnet is measured by sweeping the magnetic field, one observes a voltage change. The difference of voltages for the parallel

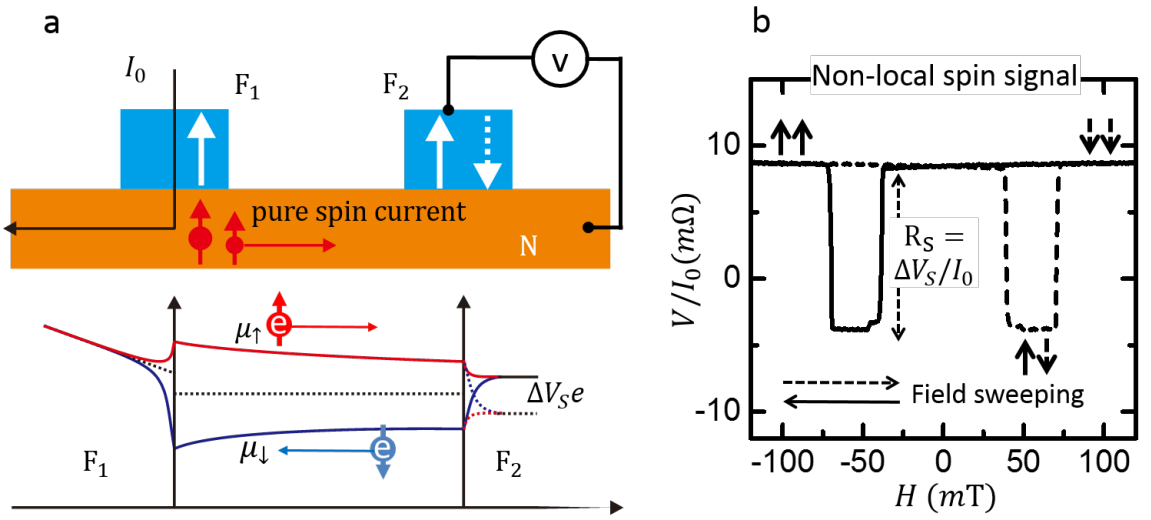

Figure 2.7: (a) Illustration of generation of pure spin current driven by electrical current. (b) One typical non-local spin signal was measured in LSV

and antiparallel ($\Delta V_S = V_P - V_{AP}$) is defined as spin voltage which determines the magnitude of pure spin current. The voltage normalized by the injecting current is known as the spin signal as shown in figure 2.7(b).

In the transparent interface lateral spin valve, the value of the detected spin signal (R_S) can be derived by solving the spin diffusion equation (2.4.5) and (2.4.6) in one-dimensional model [6–8].

$$R_S = \frac{P_F^2 R_F^2 R_N}{2R_F(R_F + R_N)(cosh(L/\lambda_N) + sinh(L/\lambda_N)) + R_N^2 sin(L/\lambda_N)} \tag{2.4.7}$$

where, P_F is the spin polarization for the ferromagnet and λ_N is the spin diffusion length for the nonmagnet. R_F and R_N are the spin resistances for the ferromagnet and nonmagnet, respectively. The spin resistance is defined as $2\rho\lambda/((A(1-P^2))$, where P, ρ, and λ are the spin polarization, the electrical resistivity, and the spin diffusion length, respectively. For a nonmagnet, P should be zero. A is the effective cross section for the spin current. For the ferromagnet, since the spin diffusion length is known to be quite short, the effective cross

section is given by the area of the ferromagnetic/nonmagnetic junction.

2.5 Thermally driven spin transport

2.5.1 Spin dependent Seebeck coefficient

The conductivity is independent for two spin states in the ferromagnetic metals. Since the Seebeck coefficient is proportional to the energy derivative of the napierian logarithm conductivity at Fermi level. The spin dependent seebeck coefficient can be expressed as following:

$$S_{\uparrow,\downarrow} = -eL_0T(\frac{\partial ln\sigma_{\uparrow,\downarrow}}{\partial E})_{E=E_F} \tag{2.5.1}$$

Where, $S_{\uparrow,\downarrow}$ is the Seebeck coefficients for up-spin and down-spin. $L_0 = (\pi^2/3)(k_B/e)^2$ is Lorenz constant, $\sigma_{\uparrow,\downarrow}$ is the energy dependent conductivity around the Fermi energy E_F for up and down spins.

2.5.2 Thermally driven spin accumulation and detection

The model of thermally driven spin accumulation, which is spin dependent seebeck effect will be briefly introduced. When one heat current flows in the ferromagnet and the temperature gradient is ∇T_{F} in F, the spin dependent current in F can be described by the following equation.

$$I_{(\uparrow,\downarrow)} = -\sigma_{(\uparrow,\downarrow)}A(\nabla\mu_{(\uparrow,\downarrow)}/e + S_{(\uparrow,\downarrow)}\nabla T_{\mathrm{F}}) \tag{2.5.2}$$

Here, $\mu_\uparrow$ and $\mu_\downarrow$ are the spin-chemical potential for up-spin and down-spin, respectively. A is the area of crossing section of heat current.

Therefore, the generated spin current can be described as follows:

$$I_{\mathrm{S}} = I_\uparrow - I_\downarrow = A\nabla T_{\mathrm{F}}[S(\sigma_\uparrow - \sigma_\downarrow) + (\sigma_\uparrow S_\uparrow - \sigma_\downarrow S_\downarrow)] = (1-P^2)A\sigma S_{\mathrm{S}}\nabla T_{\mathrm{F}}/2 \tag{2.5.3}$$

Here, S_{S} is the spin-dependent Seebeck coefficient defined by $S_\uparrow - S_\downarrow$. P is the electrical spin polarization defined by $(\sigma_\uparrow - \sigma_\downarrow)/(\sigma_\uparrow + \sigma_\downarrow)$. When one heat current Q flows

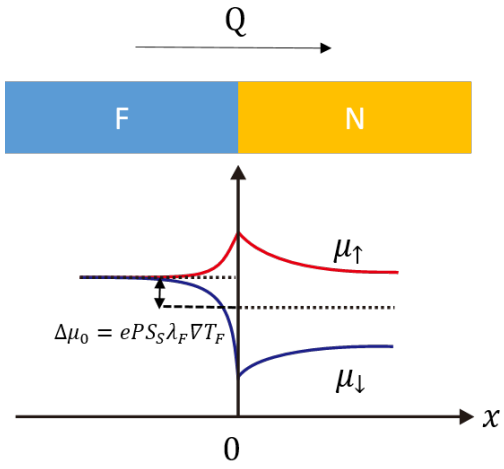

Figure 2.8: Illustration of thermal spin accumulation. The spin dependent chemical potential has been off set by contribution of conventional seebeck effect

through the ferromagnet/nonmagnet interface as shown in Figure 2.8, the spin current given by Eq. 2.5.3 is generated at the interface, depending on the temperature gradient in the ferromagnet. The generated spin current is injected into the nonmagnet and induces the non-equilibrium spin accumulation. The spin accumulation at the interface could be given by using the boundary condition. In the Ohmic junction($R_{\mathrm{SF}} \gg R_{\mathrm{I}}$), the splitting of average chemical potential could be written as $\Delta\mu_0 = eP\lambda_{\mathrm{F}}S_{\mathrm{S}}\nabla T_{\mathrm{F}}$ as shown in Figure 2.8. This spin accumulation diffuses not only into the nonmagnet but also back to the ferromagnet.

The thermally excited spin current can be treated similarly to the electrically generated spin current in the lateral hybrid structure. In this case, the position dependence of the spin signal due to spin accumulation is simply obtained by replacing the value of P on Eq. 2.4.7. Finally, the interval dependence of the thermal spin voltage due to thermal spin injection could be expressed as:

$$\Delta V_{\mathrm{S}} = \frac{P_F R_N \lambda_F \nabla T_F S_s}{2R_F(R_F + R_N)(cosh(L/\lambda_N) + sinh(l/\lambda_N)) + R_N^2 sinh(l/\lambda_N)} \tag{2.5.4}$$

Here, ∇T_F and S_s are the temperature gradient in the ferromagnet around the interface and the spin-dependent Seebeck coefficient for the ferromagnetic injector, respectively.

Bibliography

[1] S. Y. Huang, W. G. Wang, S. F. Lee, J. Kwo, and C. L. Chien. Intrinsic spin-dependent thermal transport. *Phys. Rev. Lett.*, 107:216604, Nov 2011.

[2] Abraham Slachter, Frank Lennart Bakker, and Bart Jan van Wees. Anomalous Nernst and anisotropic magnetoresistive heating in a lateral spin valve. *Physical Review B*, 84(2):1–4, July 2011.

[3] Masaki Mizuguchi, Satoko Ohata, Ken-ichi Uchida, Eiji Saitoh, and Koki Takanashi. Anomalous Nernst Effect in an $L1_0$-Ordered Epitaxial FePt Thin Film. *Applied Physics Express*, 5(9):093002, August 2012.

[4] A. Fert and I. Campbell. Two-Current Conduction in Nickel. *Physical Review Letters*, 21(16):1190–1192, October 1968.

[5] J. Stöhr H.C. Siegmann. *Magnetism from Fundamental to Nanoscale Dynamics*. Spinger, 2006.

[6] T Valet and A Fert. Theory of the perpendicular magnetoresistance in magnetic multilayers. *Physical Review B*, 48(10):7099–7113, September 1993.

[7] S. Takahashi and S. Maekawa. Spin injection and detection in magnetic nanostructures. *Physical Review B*, 67(5):052409, February 2003.

[8] T. Kimura, J. Hamrle, and Y. Otani. Estimation of spin-diffusion length from the

magnitude of spin-current absorption: Multiterminal ferromagnetic/nonferromagnetic hybrid structures. *Physical Review B*, 72(1):1–6, July 2005.

Chapter 3

Device fabrication and transport measurement

3.1 Introduction

With the rapid development of science and technology, the fabrication of nanoscale devices and detection of extremely small signals can be easily realized nowadays. All the nano-sized devices discussed in this thesis are fabricated and evaluated using all the facilities in Advanced Electronics Research Division of INAMORI Frontier Research Center. Before starting fabrication of the device, a full 5-inch Si wafer with 100 nm thickness of thermally oxidized Si is cut into 10 mm $\times$ 10 mm pieces. Then the devices are fabricated on such a substrate using two or three steps electron-beam lithography combined with physical evaporation techniques. After observing the structures of device by scanning electron microscopy (SEM), the substrate is cut and divided into suitable pieces. The wanted devices will be glued on the chip. The probes of device are bonded with pins on the chip by Al wire using the bonder made by WEST BOND. Finally, the transport properties have been evaluated by temperature controlled lock-in measurement system. Besides, one flow diagram of experimental process is presented in figure 3.1.

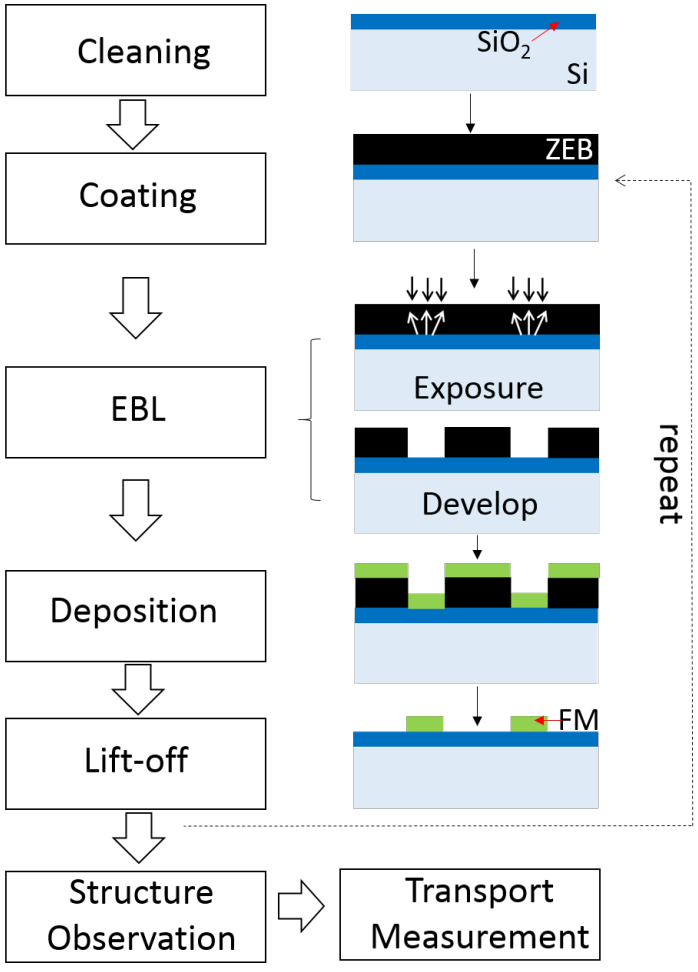

Figure 3.1: Flow diagram of the experimental process.

3.2 Device fabrication process

Cleaning substrate

- The substrate is cleaned in Acetone and isopropyl alcohol (IPA) for few ten seconds by high power ultrasonic.
- The substrate is cleaned in semiconductor cleaning liquid and Milli-Q water for few minutes by high power ultrasonic. After drying it, the condition of surface will be checked by using optical microscopy. If there are still some dusts, the substrate should be cleaned several times only by using Milli-Q water until no dusts remaining.

Coating resist

- Here, the positive photoresist has been used in our fabrication process. The thickness of the photoresist is adjusted by changing the spin speed of the spinner.
- After coating the resist, the substrate with the potoresist should be baked on hot plate.

Electron beam lithography (EBL)

- The exposure is performed in the ELIONIX ELS-7800 electron beam lithography system. The patterns are written with an accelerated voltage 80 kV and beam current 0.2 nA for fine patterns and 4 nA for coarse patterns. The total exposed dose is 200 μ C/cm^2 for both case.
- The exposed patterns are developed in O-xylene for 1 minute and quickly rinsed in IPA for few ten seconds. Then, the remained IPA is blown off by using nitrogen gas gun.

Deposition by electron beam evaporation

- Alloy sources: The alloy sources (Py, CoFeAl) had been melted by arc furnace in the Ar atmosphere. Py is made by the NiFe wires. CoFeAl alloy are made by pure elementary substance of Co,Fe and low dose of Al. In order to obtain uniform alloy, the melting and quenching procedures are operated over 10 times for each alloy source.

- Deposited condition: Usually, the deposited rate is about 0.5 - 0.9 A/s which can be controlled by emitted current under the pressure of 1.0×10^{-5} Pa.

Deposition by joule evaporation

- The Cu channel and probes of devices are deposited using Joule heating evaporating at the pressure $< 3.0 \times 10^{-5}$ Pa. In order to get clean interface between ferromagnet and Cu, the surfaces are well cleaned by low dose Ar^+ ion milling in the same chamber. The deposition rate of Cu is about 6.0 A/s.

Lift-off

- The sample with thin ferromagnet is bathed in the ZDMAC (N,N-Dimethylacetamide) and the remained resist can be easily shook off. In order to completely remove the resist, low power sonic cleaning should be performed.

- The thick film (over 100 nm) should be bathed in the ZDMAC with more than 2 hours shaking. Finally, the low power sonic cleaning should be performed.

3.3 Structure observation

The nano-structures were observed by Scanning electron microscope (SEM). Figure 3.2 shows one image of the typical lateral spin valve consisting of two ferromagnetic wires

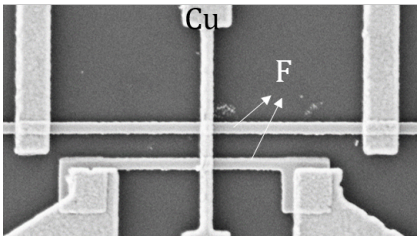

Figure 3.2: SEM image of one typical lateral spin valve.

bridged by a Cu strip. Here, one ferromagnetic wire has large pads connected to its edges to facilitate the domain wall nucleation while the other one has a flat end. This enables us to control the magnetization configuration by adjusting the magnetic field.

3.4 Transport measurement setup

3.4.1 Lock-in setup

Lock-in amplifier is an extremely important and powerful measuring tool to detect very small signal-all the way down to a few nanovolts. In this thesis, most of the experiments are performed using lock-in measurement setup. The schematic of standard lock-in measurement setup is shown as in figure 3.3.

When one AC current I(t)=$\sqrt{2}I_0$sin(ωt), with frequency ω and room mean square value I_0, is applied in the device. The detected voltage can be expressed as: $V^{in}(t) = R_1I(t) + R_2I^2(t) + R_3I^3(t) + R_4I^4(t) + \cdots$. The output voltage of a lock-in amplifier at a set phase φ is given by:

$$V_n^{out}(t) = \frac{\sqrt{2}}{T}\int_{t-T}^{T} sin(n\omega s + \varphi)V^{in}(s)ds \tag{3.4.1}$$

where, V^{in}(s) is the input voltage, the V_n^{out}(t) is the output harmonic voltage. It should be noted that the displayed harmonic voltage V^{nf} is the rms value of the output voltage by lock-in amplifier in this thesis. If we just consider a voltage response up to 3rd order, the

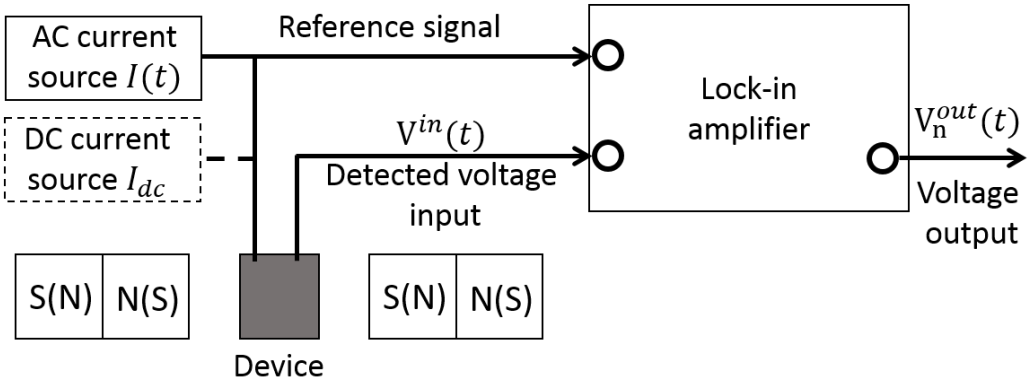

Figure 3.3: Schematic of lock-in measurement system.

harmonic voltage can be calculated as flowing:

$$V^{1f} = R_1 I_0 + \frac{3}{2} R_3 I_0^3, \qquad (\varphi = 0) \tag{3.4.2}$$

$$V^{2f} = \frac{\sqrt{2}}{2} R_2 I_0^2, \qquad (\varphi = -\pi/2) \tag{3.4.3}$$

$$V^{3f} = -\frac{1}{2} R_3 I_0^3, \qquad (\varphi = 0) \tag{3.4.4}$$

The electrically driven spin injection is evaluated by measuring the first harmonic spin voltage V^{1f} with supplying low bias AC current which is confirmed in the linear responding range of I-V curve. The heat current is arising from the local Joule heating by flowing one AC current. Because of the heat current $Q \propto I^2(t)$, the thermal driven spin injection effect could be performed by measuring the second harmonic responding.

3.4.2 DC bias current dependent measurement

During the dc bias current dependent measurement, the current source is a constant small ac current I(t) superimposed on the dc bias current I_{dc}. So the detected voltage is given as

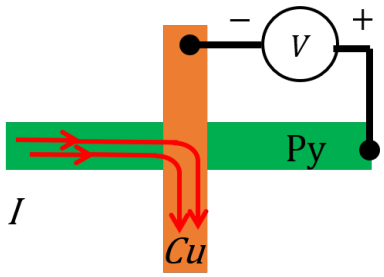

Figure 3.4: Probe configuration of the crossing junction resistance measurement.

following:

$$V^{\mathrm{in}}(t) = R_1[I(t) + I_{\mathrm{dc}}] + R_2[I(t) + I_{\mathrm{dc}}]^2 + R_3[I(t) + I_{\mathrm{dc}}]^3 + R_4[I(t) + I_{\mathrm{dc}}]^4 + \cdots \quad (3.4.5)$$

By assuming the 3rd order is valid, the first harmonic voltage can be calculated as:

$$V^{1\mathrm{f}} = R_1 I_0 + 2R_2 I_0 I_{\mathrm{dc}} + 3R_3 I_0 I_{\mathrm{dc}}^2 \quad (3.4.6)$$

Therefore, the spin and heat transports in the lateral spin valve are also evaluated by measuring first harmonic voltage under the dc bias current.

3.4.3 Evaluation of resistance for junction interface and ferromagnetic wires

Before evaluating the spin transport properties, the measurements of resistivity for the in junction interface and wires have been introduced.

Since the interface conditions could significantly affect the spin injection, such as resistivity mismatching, impurity of interface by oxidation and vacuum gap. Before measuring the spin signal, all of the crossing junction resistances were checked by local four probes measurement as shown in figure 3.4. And all of them are below the spin resistance in the Cu, which indicates our devices are transparent interface. So some interface scattering

effects could be ruled out and the evaluated spin polarization of Py is much closer to the bulk of ferromagnet.

Another important parameter is the resistivity of ferromagnetic wires. In this thesis, all of the resistivity of ferromagnetic wires are evaluated by four probe measurement in our well-defined wires with the same batch of devices.

Chapter 4

Spin transport in conventional Py/Cu LSVs

4.1 Introduction

Efficient manipulation of the spin current is a central issue for developing spintronics as well as understanding the underlying physics of spin transport.[1–3] Pure spin current, a flow of spin angular momentum without a flow of electric charge, is known as an ideal tool for investigating the spin-current-induced phenomena. Nonlocal electrical spin injection,[4, 5] spin Hall effect,[6–9] and spin pumping[10, 11] are representative methods for producing pure spin currents. Recently, in such methods the thermal current, a flow of heat, was found to be generated in addition to the spin current.[7, 12–16] Since the heat also plays an important role for the spin transport, especially in nanostructures, utilizing the thermal current may open a new avenue for the efficient manipulation of the spin current.[17] However, there are still numerous controversial and unknown phenomena related to the thermoelectric effects in nanostructured spintronic devices. Slight deviation from the ideal experimental condition produces undesired spurious signals mimicking spin-current-induced phenomena.[18, 19] Therefore, the preparation of a reliable experimental situation is key for understanding the correlation between the spin and heat currents.

To investigate the precise influence of the thermal current on the spin current, the

nonlocal spin valve signal which is one of the most reliable and well-established methods for evaluating the spin transport has been considered. A conventional metallic lateral spin valve consists of two ferromagnetic wires bridged by a nonmagnetic strip. To produce a pure spin current, the electric current flows across the ferromagnetic-nonmagnetic metal interface. Simultaneously, a thermal current can be generated by two effects.[14] One is the Peltier effect originating from the difference in the Peltier coefficients between the ferromagnetic injector and the nonmagnetic strip. This is known to induce the background offset signal in the nonlocal spin valve configuration under the low bias current. The other one is Joule heating due to the current flowing in each metallic wire. Since the ferromagnetic metals have relatively high resistivity compared to the nonmagnetic metals, the heating mainly occurs in the ferromagnetic wire. The heat locally generated in the ferromagnetic injector produces the thermal current in the device according to their thermal conductivities and was recently found to induce the thermal spin injection.[13, 20] In the present chapter, the nonlocal spin signals had been systematically investigated under various bias currents. Unconventional features are induced in the nonlocal spin valve signal because of the thermal current under high bias current.

4.2 DC bias current dependence of spin signal in Py/Cu LSVs

4.2.1 Geometry of the evaluated device

Figure 4.1(a) shows a scanning electron microscope (SEM) image of the sample used for the present study. Two Py wires, 150 nm wide and 30 nm thick, are separated as 500 nm from the center-center. Then, a Cu channel is 300 nm wide and 120 nm thick. wires.

When the dc current flows, the local heating generates not only in the Py wire but also in the vicinity of the injecting junction. The heating produces the thermal current diffusing

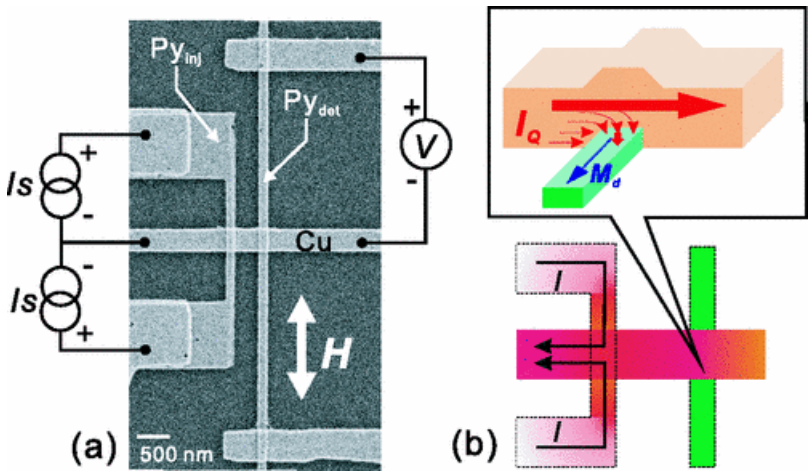

Figure 4.1: (a) Scanning electron microscope (SEM) image of the measured LSV and the probe configuration for the nonlocal spin valve measurement using the dual spin injection. (b) Schematic illustration of the temperature distribution in the device under the nonlocal spin injection and the temperature gradient in the vicinity of the nonlocal detecting junction.

in the nonmagnetic Cu wire and reaches the Py detector, as shown in figure 4.1(b).[13] This has a possibility for inducing an additional spin-dependent or independent thermal effect even in the nonlocal configuration. It also should be noted that the thermal current can be conducted via the substrate. Although the thermal current density in the substrate is much smaller than that in the Cu wire because of much smaller heat conductance of the SiO_2 layer, the contact area between the substrate and the Py wire, in which the current flows, is much larger than the Py-Cu injecting junction. This heat flows into the substrate may reduce the temperature rise in the device. However, the main heat transports in the vicinity of the Py-Cu detection junction is dominated by the heat flow via the Cu wire. To create a large thermal current, we use the dual spin injection geometry, as shown in figure 4.1(a). In this configuration, the maximum allowable current across the interface, which is limited by the maximum tolerance current in a ferromagnetic spin injector, increases two fold because the current is divided into two segments in the ferromagnetic injector.[21] Moreover, the spurious voltage due to the inhomogeneous current distribution in the injecting junction is

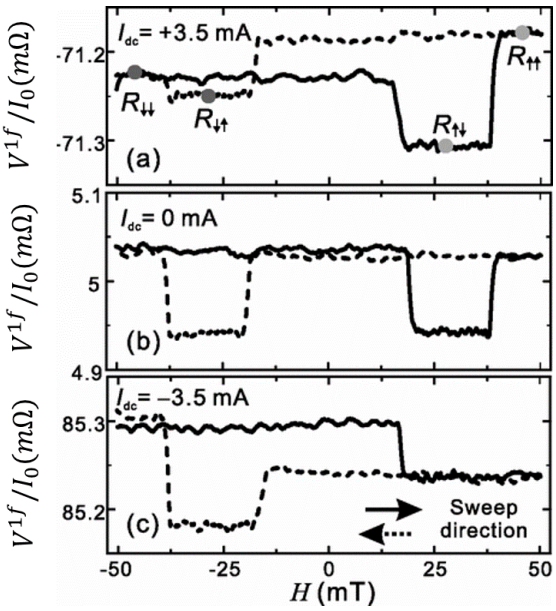

Figure 4.2: Field dependencies of the nonlocal spin valve signal under various dc bias currents, (a) +3.5 mA, (b) 0 mA, and (c) -3.5mA. Solid and dotted curves correspond to the forward and backward field sweeps, respectively. Py

minimized by this configuration.[22] In the present study, the dc current was changed from -3.5 mA to 3.5 mA. Here, the positive current corresponds to a case in which the current (electron) is injected from the Py (Cu) to the Cu (Py), as shown in figure 4.1(a). The measurements were performed in air at room temperature.

4.2.2 Results and Discussion

In figure 4.2(a)-(c), the nonlocal spin valve curves are shown for various bias dc currents (+3.5, 0, and -3.5 mA). In the absence of the dc current, a typical room-temperature nonlocal spin valve signal with the magnitude of 0.2 mΩ is clearly observed. Here, the negative resistance jump at lower magnetic field corresponding to the switching of the Py injector and positive one at higher field is the switching of the Py detector. When the dc current is superimposed, the field dependence of the spin signal becomes unexpectedly asymmetric with respect to the sweep direction of the magnetic field. For the positive

current, the signal shows higher value under the positive magnetic field [figure 4.2(a)]. For the negative current, the field dependence of the asymmetric component seems to be reversed [figure 4.2(c)]. By carefully observing the field dependence of the signals under the dc bias current, we found that the resistance change due to the switching of the Py detector (positive resistance jump) depends on the sweep direction, although that of the Py injector (negative resistance jump) does not show the sweep direction dependence. In other words, the asymmetric component in the spin signal under the dc bias current is related only to the magnetization direction of the Py detector. Since the dc current creates the thermal current as explained in figure 4.1(b), this implies that the observed asymmetric signal is induced by the interaction between the thermal current and the magnetization of Py detector. To explore the detailed origin of the bias dependence of the nonlocal spin valve signal, we define the following values:

$$R_{\mathrm{S}} \equiv R_{\uparrow\uparrow} - R_{\downarrow\uparrow} \approx R_{\downarrow\downarrow} - R_{\uparrow\downarrow}, \tag{4.2.1}$$

$$\Delta R_{\mathrm{AS}} \equiv R_{\uparrow\uparrow} - R{\downarrow\downarrow} \approx R_{\downarrow\uparrow} - R_{\uparrow\downarrow}, \tag{4.2.2}$$

$$R_{\mathrm{Avg.}} \equiv \frac{R_{\uparrow\uparrow} + R_{\downarrow\downarrow} + R_{\downarrow\uparrow} + R_{\uparrow\downarrow}}{4}. \tag{4.2.3}$$

Here, $R_{\uparrow\uparrow}, R_{\downarrow\downarrow}, R_{\downarrow\uparrow}, and R_{\uparrow\downarrow}$ are the four resistance states depending on the magnetization configuration in the nonlocal spin valve signal. The first and second arrows in the subscripts correspond to the magnetization directions for the injector and the detector, respectively. R_{S} corresponds to the resistance changes due to the magnetization switching of the Py injector in the forward or backward sweep. ΔR_{AS} is the resistance asymmetry in the parallel or antiparallel state. $R_{\mathrm{Avg.}}$ corresponds to the average resistance value for four states.

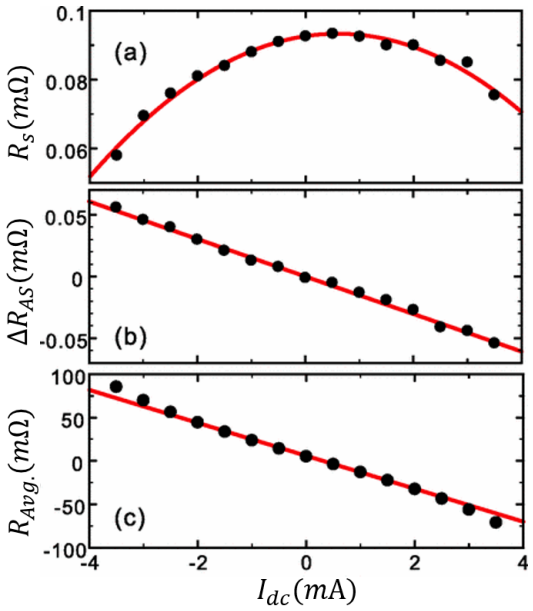

Figure 4.3: Bias current dependencies of (a) R_{S},(b) ΔR_{AS},and (c) $R_{\mathrm{Avg.}}$ Solid lines are obtained by fitting the plots on the parabolic or linear dependence.

Figure 4.3(a) shows the bias current dependencies of R_{S}. As explained above, this change does not depend on the field sweep direction and depends only on the relative magnetization configuration between the injector and detector. This means thatR_{S} corresponds to the spin signal induced by the spin accumulation. As shown in figure 4.3(a), the signal seems to decrease parabolically with increasing the magnitude of the dc current. This can be understood by the temperature change due to the Joule heating and Peltier effect or thermal spin injection, which originate from the dc bias current. The relationship between the temperature change ΔT and the current I can be described by $\Delta T = aI + bI^2$. Since the spin signal is known to decrease linearly with increasing temperature around room temperature, the current dependence of the spin signal should be given by $R_{\mathrm{S0}}[1 - r(aI + bI^2)]$, where, ΔR_{S0} is the spin signal at zero dc bias current. As can be seen in figure 4.3(a), the dependence is well fitted by the relationship $R_{\mathrm{S}} = \Delta R_{\mathrm{S0}} - (AI + BI^2)$, meaning that the effective temperature is really modified by the Joule heating, the Peltier effect and thermal

spin injection. Moreover, the Joule heating is found to be a dominant contribution of the heating above 1 mA. We then discuss the bias dependence of $\Delta R_{\rm AS}$ shown in figure 4.3(b). As describe above, the asymmetric signal change is caused by the magnetization switching of the Py detector, meaning that the $\Delta R_{\rm AS}$ does not depend on the relative magnetization configuration. Moreover, $\Delta R_{\rm AS}$ linearly decreases with increasing the dc bias current. These facts indicate that $\Delta R_{\rm AS}$ is induced by the interaction between the thermal current and the magnetization of the Py detector. As mentioned above, the thermal current $I_{\rm Q}$ along the Cu wire, schematically shown in in figure 4.1(b), is mainly induced by the Joule heating. Although the thermal current flows mainly in the Cu because of the high thermal conductivity of the Cu, a finite thermal current is injected into the Py detector. Here, the flow direction of the thermal current should be normal to the Py-Cu interface in the vicinity of the junction, as shown in the inset of figure 4.1(b). Since the thermal current in the ferromagnetic metal with the magnetization $\rm M_{\it d}$ is known to produce the transverse voltage along the direction given by $I_{\rm Q} \times M_{\rm d}$ because of the anomalous Nernst effect, the transverse voltage along the y direction is induced in the vicinity of the detecting junction. This additionally induced voltage can be detected by the nonlocal voltage probes, similarly to the measurement of anomalous Hall voltage in a ferromagnetic narrow wire.

As described in the previous paragraph, the voltage induced by the the anomalous Nernst effect is proportional to the thermal current $I_{\rm Q}$, which is given by $aI+bI^2$. Since the current I is given by $I_{\rm dc}$ $+I_{\rm ac}$ $\sin(\omega {\rm t})$, the contribution to the nonlocal spin valve signal $V_{\rm ac}/I_{\rm ac}$ from the anomalous Nernst effect is proportional to $a + 2bI_{\rm dc}$ corresponding to the coefficient of $I_{\rm ac}$ $\sin(\omega {\rm t})$ in $aI + bI^2$. As seen in figure 4.3(b), the strong linear dependence is clearly confirmed. This indicates that the additional asymmetric nonlocal voltage is induced by the anomalous Nernst effect in the lateral spin valve structures under the dc bias current.

We also discuss the bias dependence of $R_{\rm Avg.}$ shown in figure 4.3(c), The origin of $R_{\rm Avg.}$ in the absence of the dc current is now explained as follows. The heat induced by the

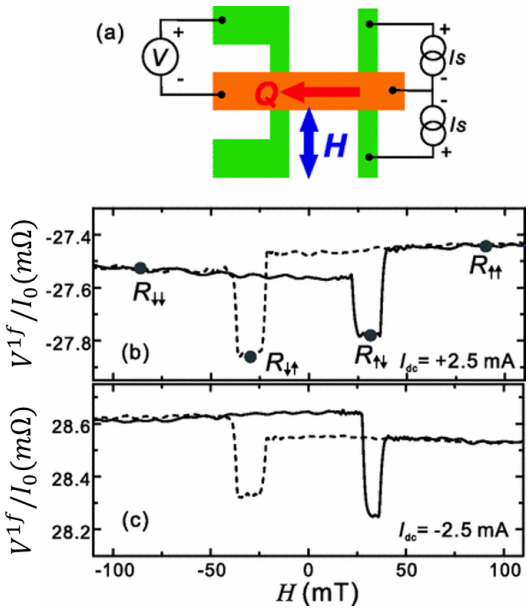

Figure 4.4: (a) Schematic illustration of the nonlocal spin valve measurement for the inter- changed probe configura- tion. Observed nonlocal spin valve signals for (b) +2.5 mA and (c) -2.5 mA

Peltier effect in the injecting junction propagates to the detecting junction and induces the temperature change at the detecting junction. The temperature change at the interface can be detected by the nonlocal voltage probe via the Seebeck effect, similar to the functioning of a thermocouple. Therefore, the finite $R_{\mathrm{Avg.}}$ in the absence of the bias dc current can be explained by the interplay between the Peltier and Seebeck effects. $R_{\mathrm{Avg.}}$ decreases with increasing the dc current. As described in the previous paragraph, the dc bias current induces the additional temperature change mainly due to the Joule heating. Therefore, the linear increase of the background signal is simply understood by the scenario similar to the bias dependence of R_{AS}. The slight deviation from the linear relationship may be caused by the temperature dependencies of the electrical resistivities and the Seebeck coefficients.

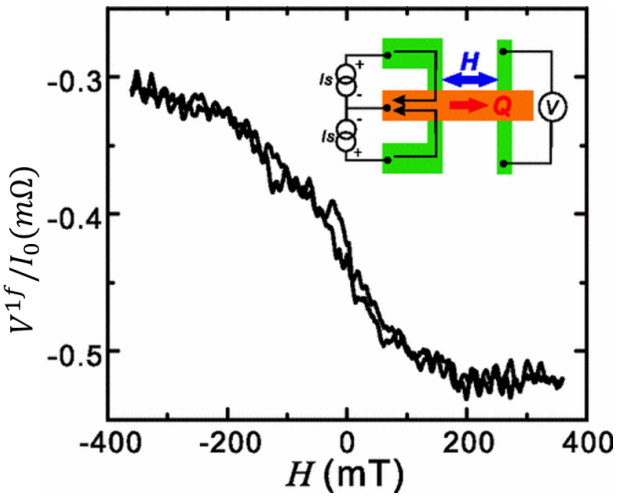

Figure 4.5: Transverse field dependence of the non- local signal under the bias current injection with the magnitude of +5 mA. The inset shows the schematic illustration for the measurement with the probe configuration

4.2.3 Additional evidence for the anomalous Nernst effect

As further evidence for the anomalous Nernst effect in the nonlocal spin valve configurations, we measure the nonlocal spin valve signal under the high bias current while interchanging the voltage and current probe configuration. Here, we used a similarly designed lateral spin Hall device with a different sample dimension. As shown in figure 4.4(a) and (b), we also confirmed that the asymmetric signal change was caused by the magnetization switching of the Py wire with the pad. We also investigate the thermoelectric transports in the lateral spin valve under the transverse magnetic field along the y direction. As mentioned above, the thermal current flows along the z direction in the vicinity of the interface. Therefore, when the magnetization of the Py detector is aligned with the y direction, the voltage along x direction is induced by the anomalous Nernst-Ettingshausen effect. This voltage can be detected by measuring the voltage difference along the $Py_{det.}$ wire, as shown in the inset of figure 4.5. Figure 4.5 shows the induced nonlocal signal under the bias current injection with the magnitude of +5 mA. As we expected, the signal varies in proportion to the y

component of the magnetization for $Py_{det.}$. It was also confirmed that the overall resistance change shows the linear dependence of the dc bias current, as in figure 4.3(b). These facts strongly support that the anomalous Nernst-Ettingshausen effect can be detected under high dc bias current injection even in the nonlocal configurations.

4.3 Summary

The influence of the dc bias current on the nonlocal spin valve signal had been systematically investigated. The dc bias current was found to induce not only the reduction of the spin signal but also the asymmetric field dependence of the nonlocal spin signal with respect to the sweep direction. These unconventional features are well explained by considering the thermal current mainly induced by the Joule heating at the injecting junction and the anomalous Nernst effect in the nonlocal Py detector. The proper treatments of the thermoelectric effects using reliable experimental situations are indispensable for investigating the emerging field of the spin caloritronics. Besides, the efficiency of generation pure spin current by reducing or utilizing heat current may be got much more enhancement.

The Py is not the best material for generate the giant pure spin current. So it's emergency to search the excellent materials.

Bibliography

[1] Igor Žutić and S. Das Sarma. Spintronics: Fundamentals and applications. *Reviews of Modern Physics*, 76(2):323–410, April 2004.

[2] Claude Chappert, Albert Fert, and Frédéric Nguyen Van Dau. The emergence of spin electronics in data storage. *Nature materials*, 6(11):813–23, November 2007.

[3] E. Saitoh T. Kimura S. Maekawa, S.O. Valenzuela. *Spin Current*. Oxford University Press, Oxford, 2012.

[4] Mark Johnson and R. H. Silsbee. Interfacial charge-spin coupling: Injection and detection of spin magnetization in metals. *Physical Review Letters*, 55(17):1790–1793, October 1985.

[5] F J Jedema, a T Filip, and B J van Wees. Electrical spin injection and accumulation at room temperature in an all-metal mesoscopic spin valve. *Nature*, 410(6826):345–8, March 2001.

[6] T. Kimura, Y. Otani, T. Sato, S. Takahashi, and S. Maekawa. Room-Temperature Reversible Spin Hall Effect. *Physical Review Letters*, 98(15):1–4, April 2007.

[7] Takeshi Seki, Yu Hasegawa, Seiji Mitani, Saburo Takahashi, Hiroshi Imamura, Sadamichi Maekawa, Junsaku Nitta, and Koki Takanashi. Giant spin Hall effect in

perpendicularly spin-polarized FePt/Au devices. *Nature materials*, 7(2):125–9, February 2008.

[8] Tomas Jungwirth, Jörg Wunderlich, and Kamil Olejník. Spin Hall effect devices. *Nature materials*, 11(5):382–90, May 2012.

[9] Luqiao Liu, Chi-Feng Pai, Y Li, H W Tseng, D C Ralph, and R a Buhrman. Spin-torque switching with the giant spin Hall effect of tantalum. *Science (New York, N.Y.)*, 336(6081):555–8, May 2012.

[10] E. Saitoh, M. Ueda, H. Miyajima, and G. Tatara. Conversion of spin current into charge current at room temperature: Inverse spin-hall effect. *Applied Physics Letters*, 88(18):–, 2006.

[11] R. Urban, G. Woltersdorf, and B. Heinrich. Gilbert damping in single and multilayer ultrathin films: Role of interfaces in nonlocal spin dynamics. *Phys. Rev. Lett.*, 87:217204, Nov 2001.

[12] K Uchida, S Takahashi, K Harii, J Ieda, W Koshibae, K Ando, S Maekawa, and E Saitoh. Observation of the spin Seebeck effect. *Nature*, 455(7214):778–81, October 2008.

[13] A. Slachter, F. L. Bakker, J-P. Adam, and B. J. van Wees. Thermally driven spin injection from a ferromagnet into a non-magnetic metal. *Nature Physics*, 6(11):879–882, September 2010.

[14] F. L. Bakker, A. Slachter, J.-P. Adam, and B. J. van Wees. Interplay of Peltier and Seebeck Effects in Nanoscale Nonlocal Spin Valves. *Physical Review Letters*, 105(13):136601, September 2010.

[15] Abraham Slachter, Frank Lennart Bakker, and Bart Jan van Wees. Anomalous Nernst

and anisotropic magnetoresistive heating in a lateral spin valve. *Physical Review B*, 84(2):1–4, July 2011.

[16] F. L. Bakker, J. Flipse, and B. J. van Wees. Nanoscale temperature sensing using the Seebeck effect. *Journal of Applied Physics*, 111(8):084306, 2012.

[17] Gerrit E W Bauer, Eiji Saitoh, and Bart J van Wees. Spin caloritronics. *Nature materials*, 11(5):391–9, May 2012.

[18] S. Bosu, Y. Sakuraba, K. Uchida, K. Saito, T. Ota, E. Saitoh, and K. Takanashi. Spin seebeck effect in thin films of the heusler compound co_2mnsi. *Phys. Rev. B*, 83:224401, Jun 2011.

[19] S. Y. Huang, W. G. Wang, S. F. Lee, J. Kwo, and C. L. Chien. Intrinsic spin-dependent thermal transport. *Phys. Rev. Lett.*, 107:216604, Nov 2011.

[20] Mikhail Erekhinsky, Fe‘lix Casanova, Ivan K. Schuller, and Amos Sharoni. Spin-dependent Seebeck effect in non-local spin valve devices. *Applied Physics Letters*, 100(21):212401, 2012.

[21] S. Nonoguchi, T. Nomura, Y. Ando, and T. Kimura. Electrical manipulation of spin polarization and generation of giant spin current using multi terminal spin injectors. *Journal of Applied Physics*, 111(7):07C505, 2012.

[22] Mark Johnson and R. H. Silsbee. Calculation of nonlocal baseline resistance in a quasi-one-dimensional wire. *Phys. Rev. B*, 76:153107, Oct 2007.

Chapter 5

Spin transport in CoFeAl/Cu LSVs

5.1 Introduction

Numerous reports concerning the detection of the spin signal in spin based devices with half-metal such as Heusler alloy has been developed and accordingly remarkable progress has been achieved because of their high polarization. However, special technique to grow the ordered crystal materials is required for the preparation of Heusler alloy, which is a complicate process. Therefore, special attention was paid to seeking promising CoFe-based ferromagnetic materials with higher spin injection efficiency by using simple deposition technique (electron beam evaporation deposition). The experiment of fabrication lateral spin valve by using CoFeAl alloy have been first reported by G.Bridoux[1]. The spin signal is 10 times larger than the LSV with CoFe injector. In this chapter, the magnetic properties of the CoFeAl thin film have been evaluated. Also the electrically spin transport properties will be investigated in CoFeAl/Cu lateral spin valves. Then the DC bias current dependence of spin signal is systemically evaluated and analyzed by one dimensional spin diffusion equation.

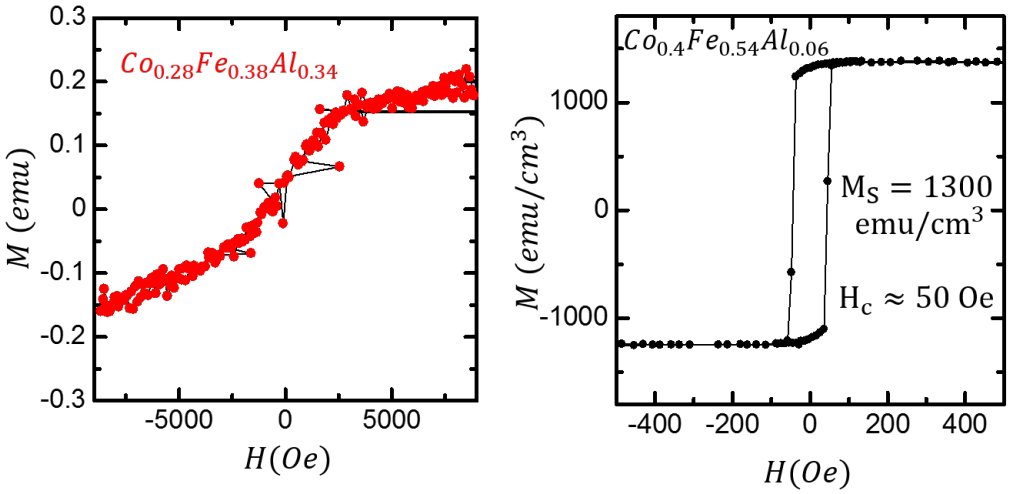

Figure 5.1: M-H curve observed for CoFeAl thin films with different composition.

5.2 Evaluation of CoFeAl thin film

The CoFeAl thin film is deposited by electron-beam evaporation from a CoFeAl ingot produced by Arc furnace. The composition of the evaporated film and its uniformity were confirmed by the Energy Dispersive X-ray (EDX) detector in a scanning electron microscope system. The obtained composition from EDX analysis is almost same with the ingot. This indicates the film composition can be easily controlled by adjusting the element composition of ingot.

The magnetic properties of CoFeAl are very sensitive with the dose of Al. In order to evaluate the influence of Al composition in this alloy, several kinds composition alloys film had been prepared. The static magnetic properties of films were evaluated by the magnetic hysteresis loop (M-H) curve using a vibrating sample magnetometer (VSM) measurement. Figure 5.1(a) shows a M-H loop obtained in the 30 nm thick CoFeAl film deposited using source composition Co:Fe:Al=36:45:19 (wt%). It looks like a typical paramagnetic alloy properties, because it does not retain the magnetic properties when the external field is

removed. If the Al ratio reduces to 4wt%, one significant different M-H loop has been observed in figure 5.1(b). The saturation of magnetization (M_s) is about 1300 emu/cm^3 for present thin film. This value is comparable to the film growing on crystal substrate. However, the coercive field (H_{C}) is about 50 Oe. which is almost 2 times larger than film growing on crystal[2]. This special property is probably due to the polycrystal structure which has low anisotropic effect. For the purpose of further understanding this point, the anisotropic magnetoresistance (AMR) of CFA was evaluated as shown in figure 5.2(a). Here, the value of AMR is about 0.176%. As we know, the microscopic origin of the AMR effect arises the second order in the spin-orbit coupling. This indicates the CFA film probably has low spin-orbit coupling. We can see that the switching field is quite broad from the red curve. This result is also in accordance with the static magnetic properties, such as large saturation magnetization field and high coercivity.

The value of coercive field has strongly relationship to the damping parameter in the dynamic properties[3]. The dynamic properties of CFA film have been evaluated by ferromagnetic resonance (FMR) measurment using a coplanar wave guide. As shown in figure 5.2(b), a clear FMR spectra has been obtained. Then, the damping constant for this film has been roughly evaluated by using the following equation:

$$\alpha = \sqrt{3}\frac{2\pi\Delta f_{\mathrm{pp}}}{\gamma}\frac{1}{2H_{\mathrm{R}} + 4\pi M_{\mathrm{s}}} \tag{5.2.1}$$

Where, γ is the gyromagnetic ratio and M_{s} is the saturation magnetization in CFA film, Δf_{pp} is the line width of the Lorentzian curve fitting and H_R is the external magnetic field. Finally, the value of damping constant is about 0.052, which is a quite large value comparing with 0.008 of Py.

In the next subsection, the spin transport properties will be introduced in lateral spin valve with CoFeAl fabricated from the source with composition of (Co:Fe:Al=48:48:4 wt%).

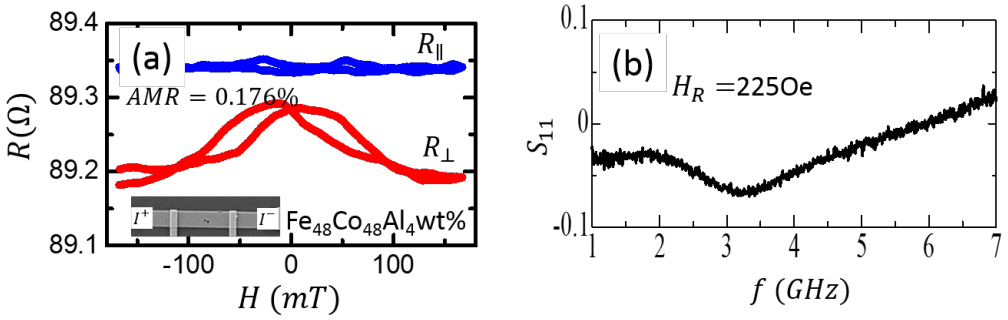

Figure 5.2: (a)AMR measurement for well defined CoFeAl wire. (b)FMR spectrum in CFA film with thickness of 30 nm under magnetic field of 225 Oe

5.3 Electrically driven spin injection in CoFeAl/Cu LSVs

5.3.1 Influence of interface in the CFA/Cu LSVs

One conventional processing has been performed to fabricate the CoFeAl/Cu lateral spin valve. Here, There are two batches of lateral spin valve devices with different milling time for cleaning ferromagnet interface. The pre-milling time is 20 second for device A and 30 s for B.

First, the junction resistances and nonlocal spin signal have been evaluated at room temperature. The junction resistance ($R_{CFA/Cu}$) for A device is 79.3Ω ($114f\Omega m^2$) and $-26m\Omega$ ($0.0374f\Omega m^2$) for B device. The high junction resistance indicates the interface of device A is not clean enough. This probably comes from the oxidation of CFA. The corresponding spin signal of device A is quite low value ($0.09m\Omega$) for interval distance 600 nm. However, the spin signal is about $3.92m\Omega$ for B device with small junction resistance. This indicates large resistance with high interface scattering, which generally dominates the device properties from quantum mechanical calculations[4, 5]. So I will keep the pre-milling time for this kind lateral spin valve to obtain the transparent interface.

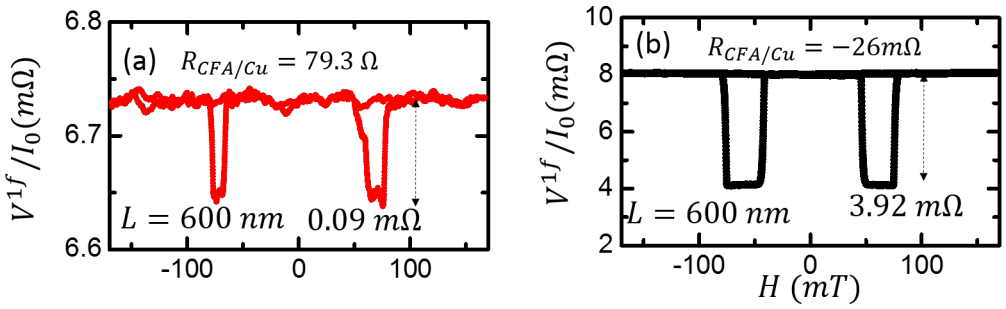

Figure 5.3: (a) The typical electron spin signal for device A. (b) The typical electron spin signal for device B.

5.3.2 Evaluation of the spin polarization of CoFeAl

The spin polarization of CoFeAl could be evaluated by electrically driven nonlocal spin signal. Figure 5.4(a) gives us one SEM image and the geometry information of the CoFeAl (CFA)/Cu LSV used in the present study.

First, the typical nonlocal spin signals have been shown in figure 5.4(b) for the CoFeAl/Cu (black curve) and permalloy (Py)/Cu (red curve) LSVs at the center–center distance L of 200 nm, respectively. We confirmed that the spin signal for the CFA/Cu LSV was almost ten times larger than that for the Py/Cu LSV, indicating the superior properties of our developed CFA injector. To elucidate the main mechanism for the significant enhancement of the spin signal in the CFA/Cu LSV, we measured the interval dependence of the spin signals for both the CFA/Cu and Py/Cu LSVs. As shown in figure 5.4(c), the room-temperature spin signals as a function of interval distance (L) for CoFeAl/Cu (solid dots) and Py/Cu (solid triangles) LSVs are plotted. For the purpose to calculate spin polarization, the resistivity for the CFA wire was evaluated from the four terminal resistance of the well-defined wire in the same batch and was estimated to be $4.5 \pm 0.2 \times 10^{-7}$ Ωm at room temperature. If we assume that the spin diffusion lengths for the CFA and Py are the same value of 2 nm [6], the dependences of the spin signal on the interval L for both devices were well fitted by

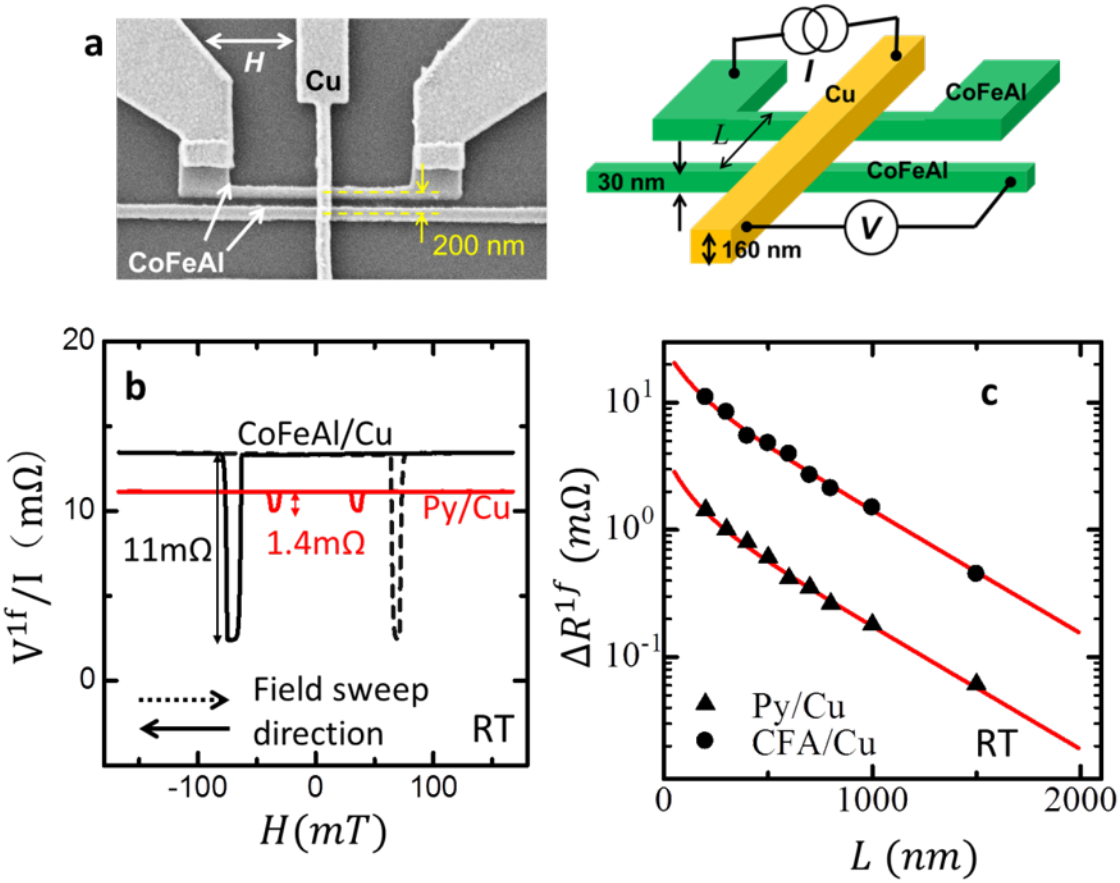

Figure 5.4: Evaluation of electrical spin polarization. (a) Scanning electron microscope image of the CoFeAl (CFA)/Cu lateral spin valve (LSV) in the present study and a schematic figure of the nonlocal spin valve measurement to evaluate the electrical spin polarization. (b) Room temperature nonlocal spin signals for the CoFeAl/Cu (black curve) and permalloy (Py)/Cu (red curve) LSVs at the centercenter distance L of 200nm. The dotted and solid curves denote the forward and backward field sweeps, respectively. (c) Room-temperature spin signal as a function of interval distance (L) for CoFeAl/Cu (solid dots) and Py/Cu (solid triangles) LSVs. The red lines are fitted curves based on Eq. (2.4.7) with λ_{Cu}=450 nm at room temperature.

the one-dimensional spin diffusion equation (2.4.7) by using the spin polarizations 0.62 and 0.36 for the CFA and Py, respectively. It should be noted that the spin diffusion lengths for the Cu obtained from the fittings in both CFA/Cu and Py/Cu LSVs were estimated to be the same value of 450 nm. Thus, the strong enhancement of the spin signal by a factor of 10 is attributed to the efficient generation and detection of the spin current due to the large spin polarization and the significant reduction of the back flow of the spin current [7]. The obtained spin polarization of the present CFA is close to the previous reported values, although the Al content and electrical resistivity are notable different, which suggests that our CFA has a different crystal structure from those in the previous reports.

5.4 DC bias current dependence of spin signal in CoFeAl/Cu LSVs

Here, the DC bias current dependence of spin signal is also systematically measured and analyzed. Since a large current induces a nonlinear voltage, the detected voltage includes higher-order terms, namely $V = R_1 I + R_2 I^2 + R_3 I^3 + R_4 I^4 + \cdots$. The contribution of the spin-dependent term can be extracted from the voltage difference between the parallel and anti-parallel states, namely,

$$V_{\rm S} \equiv V_{\rm P} - V_{\rm AP} = R_{\rm S1} I + R_{\rm S2} I^2 + R_{\rm S3} I^3 + R_{\rm S4} I^4 + \cdots \tag{5.4.1}$$

where $R_{{\rm S}i}$ is the spin dependent component defined by the difference between the parallel and antiparallel state, $R_{i{\rm P}} - R_{i{\rm AP}}$.

Then, the first harmonic spin signal $R_{\rm S}^{\rm 1f}$ was systematically investigated under the DC bias current as shown in figure 5.5(a)$\sim$(c). Here, the first harmonic spin signal $R_{\rm S}^{\rm 1f}$ is defined as $\Delta V_{\rm S}^{\rm 1f}/I_0 = (V_{\rm P}^{\rm 1f} - V_{\rm AP}^{\rm 1f})/I_0$, which is the normalized voltage difference between parallel and antiparallel states. $R_{\rm S}^{\rm 1f}$ shows the largest value of 7.66 mΩ at $I_{\rm dc} = 1$ mA while it takes the smallest value of 5.28 mΩ at $I_{dc} = -1$ mA. Figure 5.5(d) shows $R_S^{\rm 1f}$ as a

function of $I_{\rm dc}$. Overall signal change from -1 mA to 1mA is 2.38 mΩ, which exceeds 30 % of $R_{\rm S}^{\rm 1f}$ at $I_{\rm dc} = 0$. Thus, the spin signal $R_{\rm S}^{\rm 1f}$ is found to be strongly modulated by $I_{\rm dc}$. Especially, the enhancement of the spin signal under the positive high bias current is an attractive characteristic from the view point of the spin injection.

To understand the heating effect quantitatively, we consider higher order effects in the first harmonic voltages under the ac and dc currents $I = I_{\rm ac} + I_{\rm dc}$. If we consider the second, third and fourth order effects in Eq. (5.4.1), the first harmonic spin-dependent voltage $\Delta V_{\rm S}^{\rm 1f}$ and spin signal $R_{\rm S}^{\rm 1f} \equiv \Delta V_S^{1f}/I_0$ are obtained by the following equations.

$$\Delta V_{\rm S}^{\rm 1f} = (R_{\rm S1} + 2R_{\rm S2}I_{\rm dc} + 3R_{\rm S3}I_{\rm dc}^2 + 4R_{\rm S4}I_{\rm dc}^3)I_0 \tag{5.4.2}$$

$$R_{\rm S}^{\rm 1f} = R_{\rm S1} + 2R_{\rm S2}I_{\rm dc} + 3R_{\rm S3}I_{\rm dc}^2 + 4R_{\rm S4}I_{\rm dc}^3, \tag{5.4.3}$$

Importantly, the dc current dependence of $R_{\rm S}^{\rm 1f}$ observed in 5.5(d) is well reproduced by Eq.(5.4.3) with $R_{\rm S1} = 6.96$ mΩ, $R_{\rm S2} = 0.60$ mΩ/mA, $R_{\rm S3} = -0.16$ mΩ/mA^2 and $R_{\rm S4} = -0.02$ mΩ/mA^3.

We then discuss the physical meanings of the higher order effects, $R_{\rm S2}$, $R_{\rm S3}$ and $R_{\rm S4}$. By taking into account the contribution of the thermal spin injection under the temperature gradient ∇T, Eq. (2.5.4) can be expanded as follows.

$$V_S \approx \frac{P_F(P_F I + \lambda_F S_S \nabla T/R_{SF})R_{SF}^2}{R_{SN}\sinh(L/\lambda_N)} \tag{5.4.4}$$

Here, 1st term of the denominator in Eq.(2.4.7) is neglected by considering the condition $R_{SN} \gg R_{SF}$. $\rm S_S$ is the spin-dependent Seebeck coefficient for CFA. We also consider the influence of the reduction of λ_N due to the increase of the dc bias current by using the following relationship $\lambda_N = \lambda_{N0} - \Delta\lambda_N$. Here, λ_{N0} is the spin diffusion length for the Cu at room temperature and $\Delta\lambda_N$ is its change due to the temperature rising. By using the approximation $\frac{L}{\lambda_{N0}-\Delta\lambda_N} \approx \frac{L}{\lambda_{N0}}\left(1 + \frac{\Delta\lambda_N}{\lambda_{N0}}\right)$ with Taylor expansion of $\sinh x$, Eq. (5.4.4) can

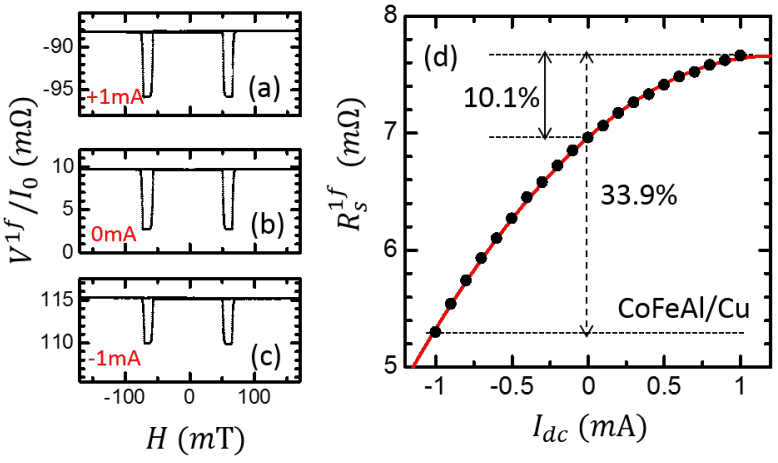

Figure 5.5: (a) ∼ (c) The detected first harmonic spin signal under various DC bias current by sweeping external filed under the small AC current. The insets show the value of DC bias currents. (d) First harmonic spin signal $R_{\mathrm{S}}^{1\mathrm{f}}$ as a function of DC bias current (I_{dc}) in CFA/Cu LSV with the interval distance 400 nm. The solid line is obtained by fitting Eq.(5.4.3)

.

be extended to

$$V_{\mathrm{S}} \approx \frac{R_{\mathrm{SF}}^2}{R_{\mathrm{SN}}} P_{\mathrm{F}}(P_{\mathrm{F}} I + \lambda_{\mathrm{F}} S_{\mathrm{S}} \nabla T / R_{\mathrm{SF}}) \left(\frac{1}{\sinh(L/\lambda_{N0})} - \frac{\cosh(L/\lambda_{N0})}{\sinh^2(L/\lambda_{N0})} \frac{L}{\lambda_{N0}} \frac{\Delta\lambda_N}{\lambda_{N0}} \right) \tag{5.4.5}$$

Since the temperature change due to the dc bias current is caused by Joule heating, it is natural to assume $\nabla T = aI^2$, where a is the constant conversion factor. $\Delta\lambda_{\mathrm{N}}$ is also caused by the temperature change due to the Joule heating. In the temperature range above 50 K, the spin diffusion length monotonically decreases with increasing the temperature [8–10]. Therefore, when the temperature variation ΔT due to the Joule heating is much smaller than the base temperature T_0, in the present case 300 K, we obtain $\Delta\lambda_{\mathrm{N}} \propto \Delta T$ from the Taylor series approximation. Since the temperature variation is proportional to the Joule heating, we also obtain $\Delta\lambda_{\mathrm{N}} = bI^2$, where b is the constant conversion factor. where the a and b are the constant conversion factors.

Then, the first harmonic spin signal $R_{\mathrm{S}}^{1\mathrm{f}}$ can be expressed by the following equation:

$$R_{\mathrm{S}} = \frac{V_{\mathrm{S}}}{\mathrm{I}} \approx \frac{P_{\mathrm{F}} R_{\mathrm{SF}}^2}{R_{\mathrm{SN}} \sinh(L/\lambda_{\mathrm{N0}})} \left(P_{\mathrm{F}} + \frac{a\lambda_{\mathrm{F}} S_{\mathrm{S}}}{R_{\mathrm{SF}}} I - \frac{bL \coth(L/\lambda_{\mathrm{N0}})}{\lambda_{\mathrm{N0}}^2} \left(P_{\mathrm{F}} I^2 + \frac{a\lambda_{\mathrm{F}} S_{\mathrm{S}}}{R_{\mathrm{SF}}} I^3 \right) \right) \tag{5.4.6}$$

From the comparison between Eq.(5.4.3) and Eq.(5.4.6), The second, third and fourth resistances R_{S2}, R_{S3} and R_{S4} are found to stem from the thermal spin injection, influence of the reduction of the spin diffusion length of Cu on the electrical spin injection and that on the thermal spin injection, respectively. Especially, the comparisons of the first and second terms yield the following relationship.

$$\frac{2R_{\mathrm{S2}}}{R_{\mathrm{S1}}} = \frac{a\lambda_{\mathrm{F}} S_{\mathrm{S}}}{P_{\mathrm{F}} R_{\mathrm{SF}}} \tag{5.4.7}$$

Here, R_{S1} can be given by the first harmonic spin signal without the dc current. Since the value of a can not be directly obtained from the experiment results, we'd better try to the simulation which will be discussed in the next chapter.

For further confirmation of the influence of the thermal spin injection, we also evaluated the second harmonic voltage in the same measurement configuration. This approach enables to exclude the influence of the electrical spin injection, and directly obtain R_{S2} from the signal. As shown in figure 5.6(a) $\sim$ (c), the clear spin signals with the magnitude of can be seen also in the second harmonic voltage under various AC bias currents. Since the detected second harmonic voltage is given by $R_{\mathrm{S2}} I_0^2/\sqrt{2}$, R_{S2} can be calculated as 0.6 mΩ/mA, which is exactly same as the value obtained in the results of fitting DC bias current. The base resistance is also found to be reproduced by the same manner.

For the comparison, we also evaluated $R_{\mathrm{S}}^{\mathrm{1f}}$ for various dc current injection for the Py/Cu LSV with a similar device dimension. Figure 5.7 shows $R_{\mathrm{S}}^{\mathrm{1f}}$ as a function of I_{dc} with a representative spin signal for $I_{\mathrm{dc}} = 0$. As can be seen in figure 5.7, $R_{\mathrm{S}}^{\mathrm{1f}}$ parabolically reduces with increasing I_{dc} and it is difficult to see a monotonic tendency originating from the thermal spin injection. From the fitting curve using Eq.(5.4.3) , we obtain $R_{\mathrm{S1}} = 0.79$

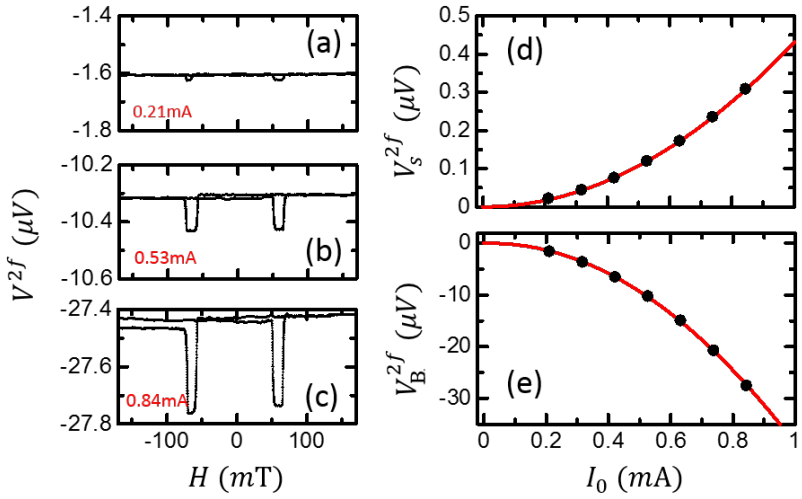

Figure 5.6: (a) $\sim$ (c) The second harmonic voltage spin signal under various AC bias current for the same CFA/Cu LSV. The insets are the exactly value of AC currents. (d-e) The second harmonic spin voltage $V_{\rm S}^{\rm 2f} = V_{\rm P}^{\rm 2f} - V_{\rm AP}^{\rm 2f}$ and base voltage of second harmonic $V_{\rm B}^{\rm 2f} = (V_{\rm P}^{\rm 2f} + V_{\rm AP}^{\rm 2f})/2$ as a function of AC bias current (I_0), respectively. The solid red curves are corresponding to the parabolic fitting.

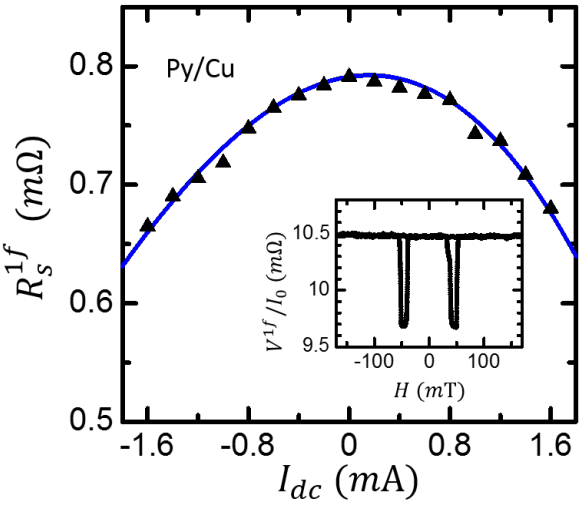

Figure 5.7: First harmonic spin signal $R_{\rm S}^{\rm 1f}$ as a function of DC bias current ($I_{\rm dc}$) in Py/Cu LSV. The solid blue line is obtained by fitting Eq.(5.4.3). The inset shows the typical lateral spin signal under 0 DC bias current in this LSV device.

mΩ, $R_{S2} = 0.0079$ mΩ/mA, $R_{S3} = -0.016$ mΩ/mA^2 and $R_{S4} = -0.00024$ mΩ/mA^3. This means that the variation of the spin signal R_S is dominated by $R_{S3}I_{dc}^2$, resulting in the parabolic reduction of the spin signal.

5.5 Summary

Let's review this chapter, three main parts have been demonstrated.

First part introduces magnetic properties of the CoFeAl film fabricated by EB evaporator. The present CoFeAl film bares large saturation magnetization ($> 1000 emu/cm^3$). The coercivity (H_C) and the damping constant (α) are larger than the crystal structures.

The second part contribute on evaluation of spin transport in CFA/Cu LSVs both in electrically and thermally driven. The electrical spin signal in CFA/Cu is 10 times larger than these in Py/Cu LSVs. The evaluated polarization of CFA is about 0.63.

The DC bias current dependence of electron spin signal results indicate that the spin signal could be significantly modulated by efficient thermal spin current. Especially, 10 percent enhancement of the spin signal under high bias current is a great advantage for generating the large spin current. From the analysis based on one dimensional spin diffusion model with considering the bias-current heating effect, we find that the contribution of the thermal spin injection is much larger than the influence of the reduction of the spin diffusion length due to the Joule heating. In addition, we know that in the Py/Cu LSV, the spin signal is significantly smeared out by anomalous Nernst-Ettingshausen effect and anisotropic magneto-Seebeck effect. Negligible spurious signals in the nonlocal signal under high-bias current for CFA/Cu LSVs is another important advantage.

In order to deeply understand the thermally driven spin transport properties, the systemically experiments and discussion will be operated in the next chapter.

Bibliography

[1] G. Bridoux, M. V. Costache, J. Van de Vondel, I. Neumann, and S. O. Valenzuela. Enhanced spin signal in nonlocal devices based on a ferromagnetic CoFeAl alloy. *Applied Physics Letters*, 99(10):102107, 2011.

[2] M. Belmeguenai, H. Tuzcuoglu, M. S. Gabor, T. Petrisor, C. Tiusan, F. Zighem, S. M. Chérif, and P. Moch. Co2FeAl Heusler thin films grown on Si and MgO substrates: Annealing temperature effect. *Journal of Applied Physics*, 115(4):043918, January 2014.

[3] Shaojie Hu, Kohei Kiseki, Satoshi Yakata, and Takashi Kimura. Ferromagnetic Resonance in Exchange-Coupled NiFe/FeMn Films and Its Control. *IEEE Transactions on Magnetics*, 48(11):2889–2891, November 2012.

[4] Schep.Kees M, Paul J. Kelly, and Gerrit E.W. Bauer. Giant Magnetoresistance without Defect Scattering. *Physical Review Letters*, 74(4):586–590, 1995.

[5] P. Zahn, I. Mertg, M. Richter, and H. Eschrig. Ab inito calculations of the giant magnetoresistance. *Physical Review Letters*, 75(16):2996–2999, 1995.

[6] T. Kimura, J. Hamrle, and Y. Otani. Estimation of spin-diffusion length from the magnitude of spin-current absorption: Multiterminal ferromagnetic/nonferromagnetic hybrid structures. *Physical Review B*, 72(1):1–6, July 2005.

[7] Takashi Kimura, Naoki Hashimoto, Shinya Yamada, Masanobu Miyao, and Kohei Hamaya. Room-temperature generation of giant pure spin currents using epitaxial Co2FeSi spin injectors. *NPG Asia Materials*, 4(3):e13, March 2012.

[8] T. Kimura, T. Sato, and Y. Otani. Temperature Evolution of Spin Relaxation in a NiFe/Cu Lateral Spin Valve. *Physical Review Letters*, 100(6):1–4, February 2008.

[9] G. Mihajlović, J. E. Pearson, S. D. Bader, and a. Hoffmann. Surface Spin Flip Probability of Mesoscopic Ag Wires. *Physical Review Letters*, 104(23):1–4, June 2010.

[10] Estitxu Villamor, Miren Isasa, Luis E. Hueso, and Fèlix Casanova. Temperature dependence of spin polarization in ferromagnetic metals using lateral spin valves. *Physical Review B*, 88(18):184411, November 2013.

Chapter 6

Thermally driven spin transport

6.1 Introduction

Spin current plays a central role in the operation of spin-based nano-electronic devices. The efficient manipulation of the spin current is essential for developing functional and energy efficient nano-spintronic devices. Recently, utilizing heat has attracted considerable attention as a new approach for controlling the spin in ferromagnetic/nonmagnetic hybrid nanostructures [1–8]. One of the representative and fascinating phenomena is thermal spin injection, in which excess heat can be used to produce the spin current because of the spin-dependent Seebeck coefficient [5–7]. So far, thermally driven spin injection has been demonstrated only by employing conventional ferromagnetic metals such as Permalloy (Py) and cobalt [2, 4]. However, the thermally excited spin current can only generate a few ten nV, which is quite low. This is due to the low spin-dependent Seebeck coefficient of conventional ferromagnetic metals. In the chapter 5, the efficient thermally driven spin injection has been observed and briefly discussed for CoFeAl. To further understand the thermally driven spin injection properties in the ferromagnet, the conceptual figures of thermally driven spin injection will be introduced. We also experimentally evaluated the spin dependent seebeck effect for CoFeAl. A combination of heat and spin transports will not only enhance the generation of spin current, but also produce unique technique to detect

the magnetic orientation indirectly. I also experimentally investigated the nonlocal thermal spin signal in CoFeAl/Cu lateral spin valve with dual spin injectors to valuable insight into how to precisely detect the magnetization switching of nano magnetic by using residual heat.

6.2 Conceptual figures of thermally driven spin injection

In electrical spin injection, the difference in the electrical conductivity between the up and down spins produces the spin current [9, 10]. However, since the moving direction of the electrons is determined by the electric field, the electrons with both up and down spins move in the same direction. Therefore, the generation efficiency of the spin current cannot exceed 100% even by using a fully spin-polarized material, namely a half-metal. On the other hand, the spin current induced by the thermal spin injection is determined by the difference of the Seebeck coefficient between the up and down spins [5, 11]. This is known as spin-dependent Seebeck effect. This effect is different from spin Seebeck effect [3, 4] although both effects produce spin current and spin accumulation from the temperature gradient. The Seebeck coefficient is strongly correlated to the band structure around the Fermi level, and, under simple approximation in metals, the coefficient is known to be proportional to the energy derivative of the logarithmic density of state (DOS) at the Fermi level [12–14]. In a ferromagnetic material, since the DOS shows different features between the up and down spins, one has to separately consider the moving directions of the up-spin electrons and the down-spin electrons.

For conventional ferromagnets, the difference in the band structure between the up and down spins can be considered approximately as a small shift of the DOS. In this case, although the up-spin and down-spin electrons produce a Seebeck effect of different magnitudes, the difference is very small. Moreover, the electrons for each spin diffuse toward the same direction, as shown in figure 6.1(a, b). Therefore, the magnitude of the

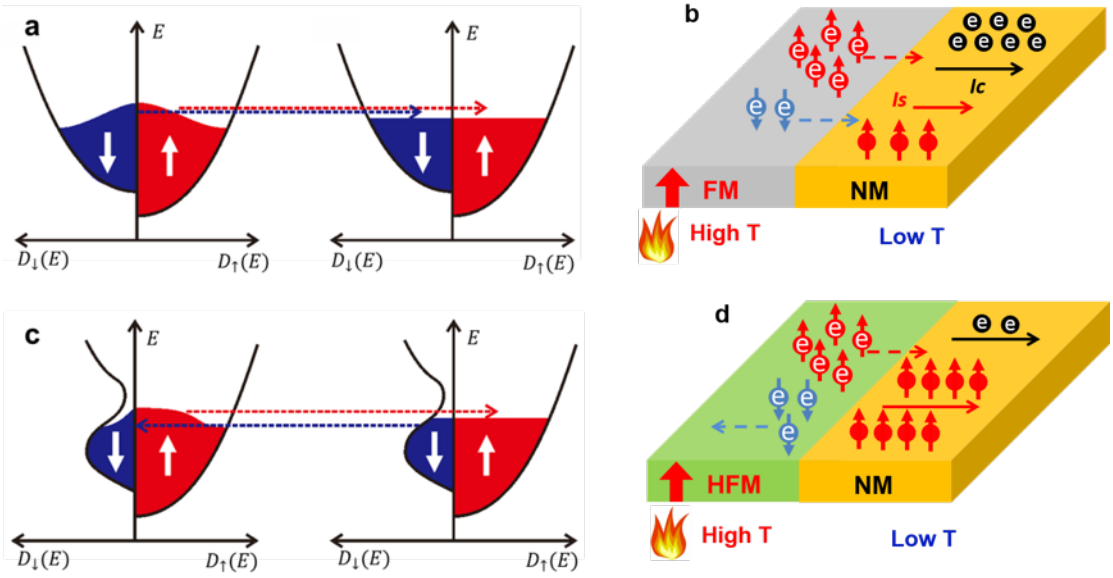

Figure 6.1: Conceptual figures of highly efficient thermal spin injection. (a) Schematic illustration of the spin-dependent DOSs for a conventional ferromagnetic metal at high (left) and low (right) temperatures. Both the up-spin and down-spin electrons diffuse from the left-hand side (the high temperature) to the right-hand side (the low temperature). (b) Charge and spin current flow in the conventional ferromagnet/nonmagnet junction under the temperature gradient. The generation and injection efficiencies are quite low because both the up-spin and down-spin electrons move along the same direction. (c) Schematic illustration of the spin-dependent DOSs for a highly spin-polarized ferromagnetic metal at high (left) and low (right) temperatures. The small DOS for the minority spin around the Fermi level reverses the moving direction of the electrons under the temperature gradient. As a result, the moving direction for the down-spin electrons is opposite that for the up-spin electrons. (d) Charge and spin current flow in the highly spin-polarized ferromagnet/nonmagnet junction under the temperature gradient. The spin current is efficiently generated and injected into the nonmagnet

spin current diminishes. On the other hand, if a ferromagnetic material has a large difference in the DOS between up and down spins, the sign reversal of the Seebeck coefficient between the up and down spins may be produced. In such a situation, the up-spin and down-spin electrons flow in opposite directions, as shown in figure 6.1(c, d). Therefore, the generation efficiency of the spin current due to thermal spin injection is significantly enhanced by the large spin-dependent Seebeck coefficient.

To realize such a favorable situation for the efficient thermal spin injection, we focused on a ferromagnetic CoFeAl (CFA) alloy, which is expected to have high spin polarization even in a simply evaporated polycrystalline film because of the local formation of a highly spin-polarized Heusler compound [15, 16]. In the next section, the thermally driven spin injection properties have been evaluated.

6.3 Evaluation of thermal spin injection

6.3.1 Evaluation of spin dependent Seebeck coefficient

We performed the thermal spin injection by using a special probe configuration in the lateral spin valve device. To create a temperature gradient across the ferromagnetic/nonmagnetic interface, which is the driving force of thermal spin injection, a large ac charge current flowed in the ferromagnetic wire, as shown in figure 6.2(a). From a numerical simulation based on COMSOL multiphysics, a large temperature gradient around the interface can be effectively produced by the large current flow in the ferromagnetic injector, as shown in figure 6.2(b). Because of the low resistivity of the Cu, a partial current flowing in the ferromagnetic injector is injected into the Cu around the junction, which may contribute to the spin accumulation via the electrical spin injection. However, such contributions can be excluded by the second harmonic lock-in technique. In addition, we confirmed that the contribution of the electrical spin injection was negligible from the first harmonic measurement in the subsection 6.3.3.

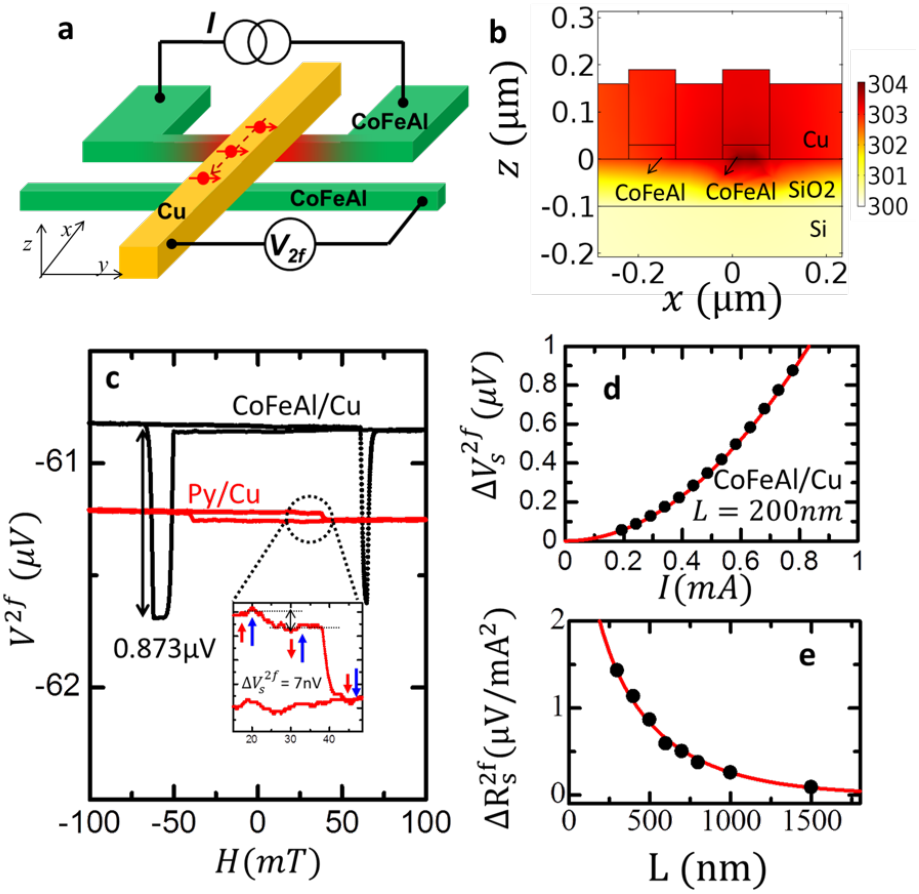

Figure 6.2: Giant spin accumulation due to thermal spin injection. (a) Schematic illustration of the thermal spin injection and detection using the LSV structure. Thermally excited spin current is generated by flowing a large current in a ferromagnetic wire (F1), which is then detected by the ferromagnetic detector (F2) with the second harmonic voltage detection technique. (b) Numerically simulated result of the spatial distribution of the temperature around the CFA/NM injecting junction under a large current of 0.78 mA. Here, the current value corresponds to the root-mean square. It is clearly confirmed that the Joule heating induced by the current flow in the ferromagnetic wire produces a temperature gradient across the FM/NM interface. (c) Field dependence of second harmonic voltage under the thermal spin injection for CoFeAl/Cu LSV (black line) with a 200 nm interval distance under a bias current of 0.78 mA, together with the second harmonic signal for the Py/Cu LSV with the same sample dimensions under a bias current of 1.08 mA. The asymmetric field dependence is induced by the anomalous Nernst effect in the Py detector. (d) Bias current dependence of the second harmonic spin voltage V^{2f} for the CFA/Cu LSV. The red line is the fitting curve assuming the parabolic dependence. (e) The thermal spin signal, defined as $\Delta R_s^{2f} = \Delta V_s^2/I^2$, as a function of interval distance L for CFA/Cu LSV at room temperature. The solid red line is a fitted curve based on Eq. (2) assuming λ_{Cu}=450 nm.

We measured the second harmonic voltage under the large ac current flow as a function of the magnetic field in the CFA/Cu LSV. As seen in figure 6.2(c), the voltage clearly reflected the relative angle between the spin injector and the detector, similar to the spin signal under the electrical spin injection. We performed similar measurements using the Py/Cu LSV with the same device dimensions. The signal was found to be dominated by the anomalous Nernst-Ettinghausen effect in the Py detector, although a tiny spin signal with a magnitude of 7 nV was observed [17].

We also confirmed that the voltage difference between the parallel and antiparallel states parabolically increased with increasing ac bias current, as shown in figure 6.2(d). In addition, the interval dependence of the voltage difference is well explained by Eq. (2.5.4) obtained from the one-dimensional spin diffusion model.

It should be noted that the parameters obtained in the electrical spin injection experiments well reproduce the experimental results in the thermal spin injection. These characteristics are clear evidence for the thermal spin injection. As shown in figure 6.2(e), by fitting diffusion function to interval dependence of the thermal spin signal, defined as $\Delta R_{\mathrm{s}}^{2\mathrm{f}} = \Delta V_{\mathrm{s}}^2/I^2$, with the COMSOL simulation results ($\Delta T_{\mathrm{F}} = 64K/\mu V$,I=0.78 mA), we obtained -72.1μV/K as the spin-dependent Seebeck coefficient for the CFA. This value is approximately 20 times larger than the value previously reported by A. Slachter[4], which implies that our CFA is a highly efficient thermal spin generator.

We can also estimate the effective Seebeck coefficient S_0 from the background of the second harmonic voltage [18]. The background voltage increased parabolically with increasing bias ac current. From the fitting with the assumption, we obtained the conventional Seebeck coefficient of -22μV/K. Notably, the spin-dependent Seebeck coefficient was larger than the conventional Seebeck coefficient. From the relationships of $S_0 = (S_\uparrow\sigma_\uparrow + S_\downarrow\sigma_\downarrow)/(\sigma_\uparrow + \sigma_\downarrow)$ and $S_S = S_\uparrow - S_\downarrow$, the Seebeck coefficients for up-spin ($S_\uparrow$) and down-spin ($S_\downarrow$) electrons

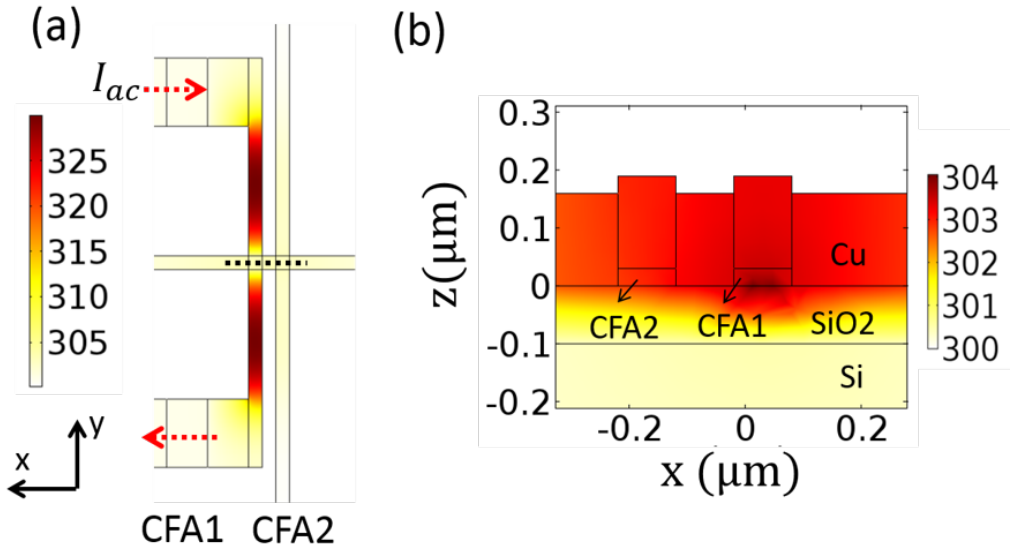

Figure 6.3: Numerically simulated spatial distributions of the temperature in the whole device (a) and in the vicinity of the CFA/Cu junction (b) under the bias current of 0.78 mA. The temperature gradient from CFA1 to Cu is clearly confirmed

were calculated as -35.7μV/K and 36.4 μV/K, respectively. Thus, the significant enhancement of the spin-dependent Seebeck coefficient is due to the sign reversal of the Seebeck coefficient. We note that some of the band structure calculations show that the sign of the energy derivatives of the density of states around the Fermi level for up and down spins are opposite each other [19, 20]. Understanding the correlation between the electrical spin polarization and the spin-dependent Seebeck coefficient may be the key for further development of the thermal spin injection and may provide a relationship between spin-dependent and spin Seebeck effect [21]. Systematic experiments for various ferromagnetic alloys with further development of the band-structure calculations are indispensable for finding more excellent material for the thermal spin injector.

6.3.2 Numerical simulation of temperature profile

We have numerically calculated the spatial distributions of the current and the temperature of our CFA/Cu lateral spin valve under the bias current I_{ac} = 0.78 mA in the CFA wire by using the finite element program Comsol Multiphysics. The current flows in the CFA wire through the top and bottom contact pads. Here, we assume that the thermal conductivities of Cu, CFA, Si, and SiO2 are 400, 29.8, 130 and 1.4 $Wm^{-1}K^{-1}$, respectively. Figures 6.3(a) and (b) show the three dimensional color plots for the calculated the temperature on lateral and vertical profile, respectively. As shown in figure 6.3(a), the temperature of the CFA injector becomes maximum at the center between the pad and the junction. However, from the magnified image shown in figure 6.3(b), we can confirmed that the temperature gradient (∇T_F=64K/μm) from the CFA to the Cu is effectively induced at the junction.

6.3.3 Confirmation of detected thermal spin signal without electrical spin injection contribution

In order to evaluate the contribution from the electrical spin injection under the thermal spin injection shown in top of figure 6.4(a), we measured the first-harmonic spin voltage together with the second-harmonic voltage. As shown in the bottom of figure 6.4(a), we can see a spin valve signal with the small magnitude of 0.06 mΩ. This value corresponds to 0.0468 μV much smaller than the magnitude in the second-harmonic signal. Therefore, the contribution from the electrical spin injection can be negligible. In addition, the parabolic current dependence of the second-harmonic signal also supports the thermal nature of the obtained spin signal. The observed tiny spin signal in the first-harmonic voltage originated from the inhomogeneous current distribution around the junction. A partial current flowing in the ferromagnetic injector is injected into the Cu channel because of the high electron conductivity of Cu. According to the one-dimensional spin diffusion mode, the contribution of spin current is canceled out because the magnitudes of the incoming and

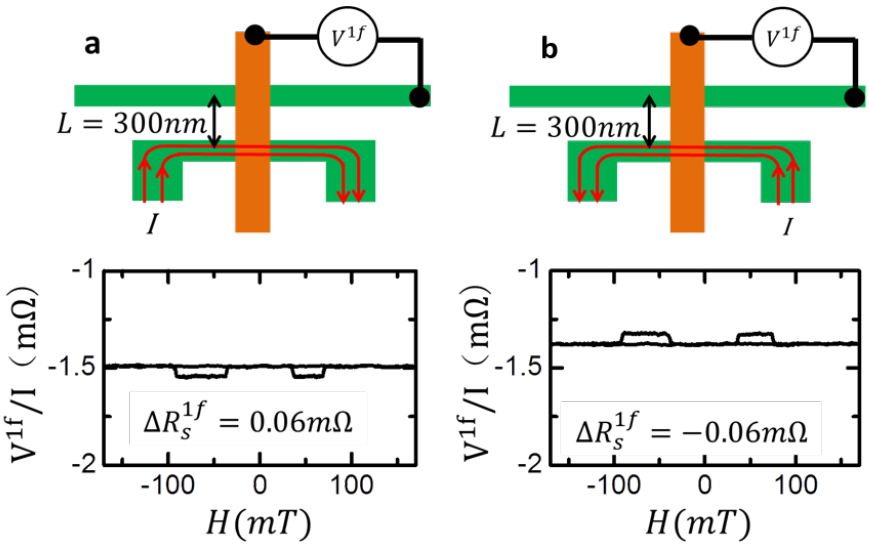

Figure 6.4: Thermal spin resistance under the thermal spin injection. (a) The first-harmonic spin valve signal under the thermal spin injection together with the schematic of the measurement probe configuration for CoFeAl/Cu lateral spin valve. Here, the interval distance between ferromagnetic wires is 300nm and (b) those under the reversed current injection.

outgoing currents at the interface are the same. However, in realistic case, the current has an inhomogeneous distribution. The nonlocal voltage cannot exclude such inhomogeneous contribution completely. We also confirmed that the reversed spin signal with the same magnitude was observed by reversing the current probe configuration as shown in figure 6.4(b). These experimental facts strongly support the above scenario.

6.3.4 Thermal spin injection in LSV with different materials

For further conformation of the origin of the enhanced thermal spin signal, we also fabricated another type lateral spin valve containing of CoFeAl and Py wires which are separated by 500nm from center to center. We compared the thermal spin signal by reversal the injector and detector. As shown in figure 6.5(a), the thermal spin signal of 0.064 μV/mA^2 is observed by using injector of CoFeAl and detector of Py. However, the thermal spin signal is only 0.018 μV/mA^2 shown in figure 6.5(b) even by using higher spin polarized detector

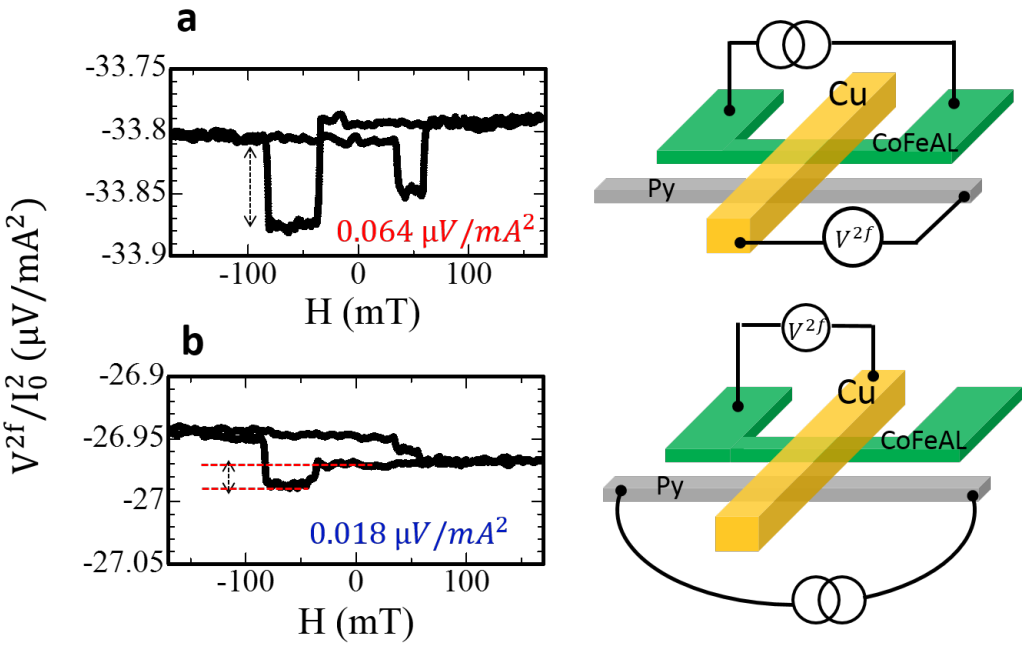

Figure 6.5: Thermal spin signal in the lateral spin valve consisting of Py and CFA wires which are separated by 500 nm between center to center. (a) Thermal spin signal observed for injector of CFA and detector of Py as shown in the right schematic of measurement configuration. (c) The thermal spin signal with measurement configuration for injector of Py and detector of CoFeAl.

of CFA and larger resistance joule heater of Py. From the qualitative analysis, the thermal spin signal could be evaluated as the proportion of the spin dependent of injector $S_{\mathrm{S}}^{\mathrm{Inj.}}$, polarization of detector $P_{\mathrm{Det.}}$ and resistance of injector wire $R_{\mathrm{Inj.}}$. It should be noted that the temperature gradient of injector is proportional to the resistance of the joule heater. So the thermal spin resistance is also proportional to the resistance of injector wire. Then we can give the following relationship by above considering,

$\Delta R_{\mathrm{S}}^{\mathrm{2f}} \propto S_{\mathrm{S}}^{\mathrm{Inj.}} P_{\mathrm{Det.}} \rho_{\mathrm{Det.}} R_{\mathrm{heater}}$

By using the value of $\mathrm{P_{Py}}$=0.36, $\mathrm{P_{CFA}}$=0.62, $\mathrm{R_{heater}^{Py}}$=490 Ω and $\mathrm{R_{heater}^{CFA}}$ = 170 Ω, we can evaluate the ratio of $S_{\mathrm{S}}^{\mathrm{CFA}}/S_{\mathrm{S}}^{\mathrm{Py}} \approx 22.7$. The giant ratio of the spin dependent seebeck coefficient is the origin of the giant thermal spin signal. By consider the value to $S_{\mathrm{S}}^{\mathrm{CFA}} = -72.1\mu V/K$, we can also obtain $S_{\mathrm{S}}^{\mathrm{Py}} \approx -3.2\mu V/K$ which is quite close to the value in the previous reports. This indicates that this method could be used to evaluated the spin-dependent seebeck coefficient for the low thermal generation efficient materials.

6.3.5 Temperature evaluation of thermal spin signal

The thermal spin injection performances were also evaluated at low temperature. Figure 6.6(a) shows the thermal spin signal as a function of external field at 5.5 K under bias current of 0.77 mA. Very clear different thermal spin signal was also observed for the parallel and antiparallel states for CoFeAl/Cu LSV with the interval distance of 200 nm.

The temperature dependence of thermal spin resistances is also plotted in the figure 6.6(b) for the CoFeAl/Cu LSV (solid dot). For comparing, the data for Py/Cu is also plotted as triangle dot. The reduction of the thermal spin resistance is gradually change with increasing temperature. However, the difference becomes increasing between the two types spin valve results. The thermal spin resistance of CFA/Cu is over 100 times larger than Py/Cu LSV from 220 K. This results indicates the CFA/Cu lateral spin valve expresses excellent properties for thermal spin injection especially at room temperature. It's also

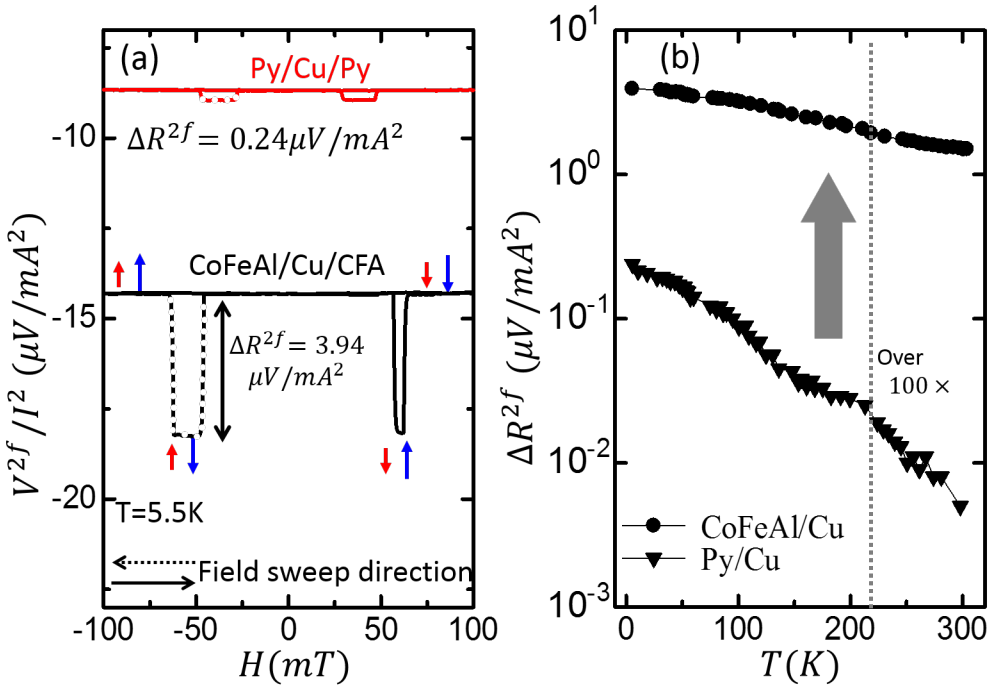

Figure 6.6: Temperature evaluation of thermal spin signal. (a) Thermal spin signal as a function of external field at 5.5 K under bias current of 0.78 mA both for CFA/Cu and Py/Cu LSVs. (b) Temperature dependence of thermal spin resistances for Py/Cu and CFA/Cu LSVs, respectively.

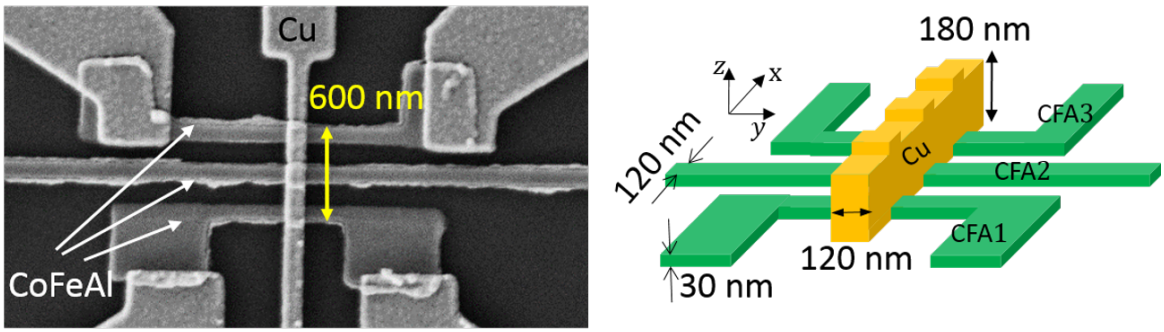

Figure 6.7: SEM image with the schematic of present LSV structure consisting of 3 CFA wires.

expected to be used in the high temperature.

6.4 Detection of the magnetic orientation by thermal spin current

6.4.1 Geometry of device

We fabricated one type lateral spin valves by two-steps lift-off processes based on the electron beam lithography. Figure 6.7 shows the scanning electron microscope (SEM) image and schematic of lateral spin valve device consisting of three CoFeAl (CFA) wires, which are separated each other by 300 nm from center to center. First, CFA wires 30-nm-thick and 120-nm-width were deposited by electron beam evaporation on a thermally oxidized Si substrate under ultra-high vacuum. Here, the different shapes of CoFeAl wires on its edges enable us to control the magnetization configuration by adjusting the magnetic field. Then, a Cu channel 180-nm-thick and 120-nm-width was deposited crossing the CoFeAl wires.

6.4.2 Results and discussion

First, we evaluated the spin transport properties of present lateral spin valve device by measuring nonlocal spin signal. Figure 6.8(a) shows the typical field dependence of nonlocal spin signals at room temperature with the schematic illustration of the measurement configuration in left. Where, sufficient large spin signal, which is defined as

$R_{\mathrm{S}}^{\mathrm{ele}} = (V_{\downarrow\downarrow}^{1\mathrm{f}} - V_{\uparrow\downarrow}^{1\mathrm{f}})/I_0 \approx (V_{\uparrow\uparrow}^{1\mathrm{f}} - V_{\downarrow\uparrow}^{1\mathrm{f}})/I_0$, is observed as 4.2 mΩ for the interval distance 300nm. Such a result is identical with our previous report for CoFeAl alloy. This indicates our device is also excellent for spin injection and detection. And then, we checked the spin absorption effect in this device.

Figure 6.8(b) shows the measured configuration and electron spin signal which is about 0.75 mΩ. Such a spin signal is much smaller than 2.56 mΩ, which is the value without middle CFA wire. This indeed indicates that most of the spins absorbed in the middle CoFeAl wire, in other words the spin current lost most of their momentum after flowing one ferromagnetic due to its large spin relaxation.

However, we couldn't see any changing in the spin signal shown in figure 6.8(b) at the switching field of the middle wire. This implies that the approach can not distinguish the magnetic orientation of middle wire because the magnitude of spin current absorption does not depend on its orientation of magnetization.

In order to confirm the values of switching field for each CoFeAl wires at same curve, we evaluated the electric spin signal in dual spin injectors as shown in figure 6.8(c). Three levels resistances are clearly obtained from the electron spin signal. In the forward sweeping (dash line), the overall distinct switching fields are observed around 33.5 mT, 47.5 mT and 70.3 mT owing to the different magnet orientation of the three CFA wires, separately. When we swept the field from one saturation field to opposite one, the first dropping of spin resistance $R_{\mathrm{S1}}^{\mathrm{ele}} = (V_{\downarrow\downarrow\downarrow}^{1f} - V_{\uparrow\downarrow\downarrow}^{1f})/I_0 \approx (V_{\uparrow\uparrow\uparrow}^{1f} - V_{\downarrow\uparrow\uparrow}^{1f})/I_0 = 0.67m\Omega$, which is the same magnitude with figure 6.8 (b). This indicates the dropping is corresponding to the magnetization (M1 ≈ 33.5 mT) switching of spin injector CFA1 wire. If continuing increasing filed, the highest value of spin resistances is observed at the states of $V_{\uparrow\downarrow\uparrow}^{1f}/I_0$ and $V_{\downarrow\uparrow\downarrow}^{1f}/I_0$. By comparing the value of switching with figure 6.8(a), this corresponds to the magnetization (M3 ≈ 47.5 mT) switching of spin detector CFA3. After all the magnetizations in these wires are parallel, the spin resistance drops again and defined $R_{\mathrm{s2}}^{\mathrm{ele}}$ as $(V_{\uparrow\uparrow\uparrow}^{1\mathrm{f}} - V_{\uparrow\downarrow\uparrow}^{1\mathrm{f}})/I_0 \approx (V_{\downarrow\downarrow\downarrow}^{1\mathrm{f}} - V_{\downarrow\uparrow\downarrow}^{1\mathrm{f}})/I_0$, which

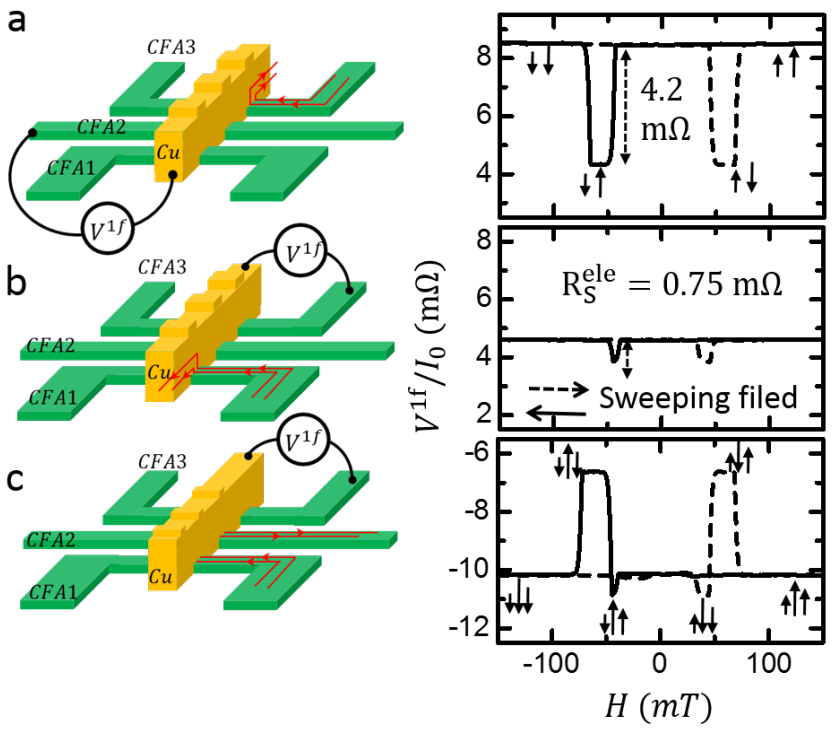

Figure 6.8: Typical electrical spin signal with various measurement configurations in the left.

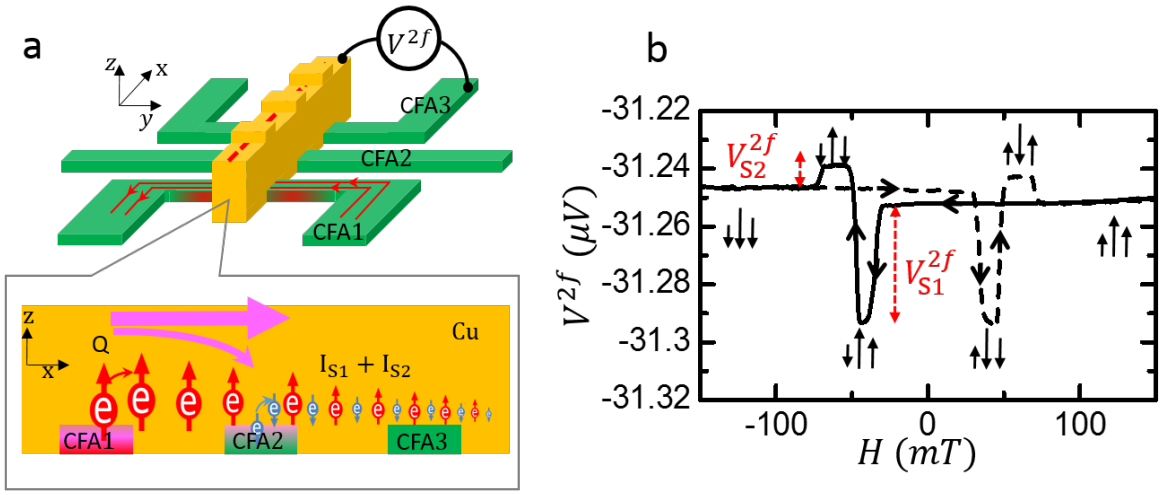

Figure 6.9: (a)Measurement configuration and the schematic of thermal spin injection for this device. (b) Second harmonic voltage as a function of sweeping field.

is about 3.55 mΩ.

So the switching magnetization (M2 ≈ 70.3 mT) of middle wire can be detected from the curve of spin signal by using such a dual spin injectors. It should be noted the negative spin resistance corresponding to the direction of the current flowing from Cu to CFA2. However this approach couldn't be used in technique without wire connection.

After that, We developed another technique which uses the injection of spins generating by local heat current as shown in figure 6.9(a). when one AC current of 0.63 mA flows into CFA1 wire, a local Joule heat current will be created and flows into Cu through CFA/Cu interface. Owing to different seebeck coefficient for spin up and down states, the heat current Q though CFA1/Cu interface enable to create the accumulation of spin momentum which diffusion apart from interface to generate a spin current I_{s1} in Cu channel. Simultaneously, the heat current propagates to the lateral CFA2 wire and through Cu/CFA2 to create one opposite temperature gradient in CFA2 wire around interface. So an additional spin current I_{s2} will be created in Cu channel. In addition, the two current model indicates that the sign

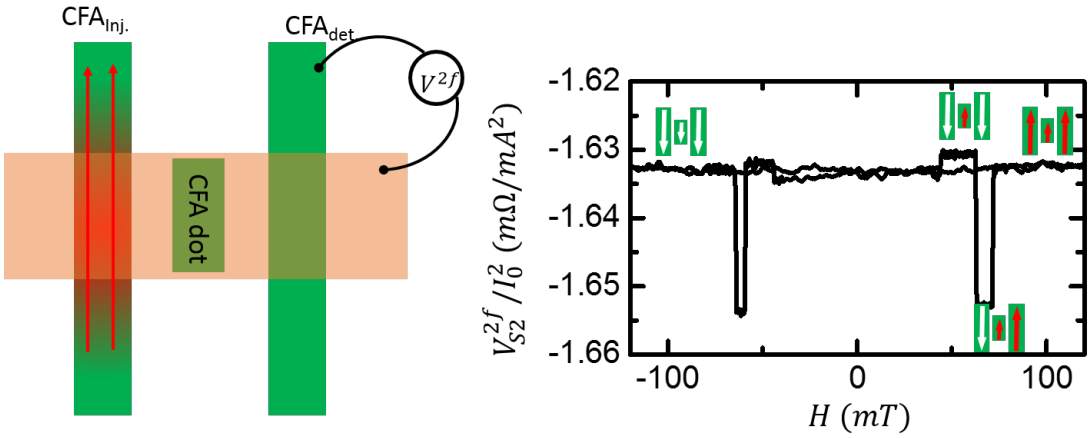

Figure 6.10: Schematic configuration and thermal spin signal of detection the magnetization of embedded CFA dot.

of the spin current is also related to the direction of magnetization. Therefore, the direction of ferromagnetic could be responded by the sign of spin current. Here, the spin current will be detected in the vicinity CFA3 wire by measuring the second harmonic voltage changing under sweeping field using standard lock-in measurement system.

We found an unique thermal signal loops which also included three levels thermal resistance with clearly distinct switching field.

The thermal spin resistance $R_{S1}^{th} = (V_{\downarrow\downarrow\downarrow}^{2f} - V_{\uparrow\downarrow\downarrow}^{2f})/I_0^2 \approx (V_{\uparrow\uparrow\uparrow}^{2f} - V_{\downarrow\uparrow\uparrow}^{2f})/I_0^2 = 0.12\mu V/mA^2$ is corresponding to the switching of magnetization of CFA1 and $R_{S2}^{th} = (V_{\uparrow\uparrow\uparrow}^{2f} - V_{\uparrow\downarrow\uparrow}^{2f})/I_0^2 \approx (V_{\downarrow\downarrow\downarrow}^{2f} - V_{\downarrow\uparrow\downarrow}^{2f})/I_0^2 = -0.023\mu V/mA^2$ is due to the switching of magnetization of CFA2. This indicates the CFA2 can also generate additional spin current, which is large enough to be detectable. The different signs of R_{S1}^{th} and R_{S2}^{th} are arising from the opposite temperature gradient at junctions of CFA1/Cu and CFA2/Cu. We can detect and distinguish the switching field of middle magnetic wire without wire connection.

However, the ratio of R_{S1}^{th}/R_{S2}^{th} is quite different from $R_{S1}^{ele}/R_{S2}^{ele}$. This can be understood

by the different heat current in CFA1/Cu and Cu/CFA2 junctions. As we know the background of thermal spin signal comes from the joule heating and Seebeck effect. Therefore we confirmed that by evaluating the background signal.

For further confirmation, we fabricated an another type device as shown in figure 6.10, one nano-dot has been buried in the 300 nm Cu channel. when we apply the current in one wire, by measuring the second harmonic resistance between the other wire and Cu, we can also see clearly three level thermal resistances. These results give us the directly evidence the orientation of the nano dot can be detected by the thermal spin signal.

6.5 Summary

The thermally driven spin signal is two folder higher than conventional ferromagnet based LSVs. The spin dependent seebeck coefficient of CFA is evaluated as $\sim -72.1\mu V/K$. Therefore,realization of the efficient generation of the spin current due to thermal spin injection provides unique architectures for wireless spintronic devices, which greatly simplify device integration. In addition, from the viewpoint of energy harvesting, utilizing heat is one of the most promising approaches for clean energy technology. Discoveries of excellent materials for thermal spin injection open a new avenue for spintronic device application.

One example of the application is indirectly detection of the magnetic orientation of nanomagnet. Here, one succeed in detecting the magnetization switching of nano dot embedded in the nonmagnetic wire. Our work demonstrates the potential of efficient thermal spin injection in the application of spintronics.

Bibliography

[1] Mark Johnson and RH Silsbee. Thermodynamic analysis of interfacial transport and of the thermomagnetoelectric system. *Physical Review B*, 35(10), 1987.

[2] Laurent Gravier, Santiago Serrano-Guisan, François Reuse, and J.-Ph. Ansermet. Spin-dependent Peltier effect of perpendicular currents in multilayered nanowires. *Physical Review B*, 73(5):052410, February 2006.

[3] K Uchida, S Takahashi, K Harii, J Ieda, W Koshibae, K Ando, S Maekawa, and E Saitoh. Observation of the spin Seebeck effect. *Nature*, 455(7214):778–81, October 2008.

[4] A. Slachter, F. L. Bakker, J-P. Adam, and B. J. van Wees. Thermally driven spin injection from a ferromagnet into a non-magnetic metal. *Nature Physics*, 6(11):879–882, September 2010.

[5] Jean-Christophe Le Breton, Sandeep Sharma, Hidekazu Saito, Shinji Yuasa, and Ron Jansen. Thermal spin current from a ferromagnet to silicon by Seebeck spin tunnelling. *Nature*, 475(7354):82–5, July 2011.

[6] Marvin Walter, Jakob Walowski, Vladyslav Zbarsky, Markus Münzenberg, Markus Schäfers, Daniel Ebke, Günter Reiss, Andy Thomas, Patrick Peretzki, Michael Seibt, Jagadeesh S Moodera, Michael Czerner, Michael Bachmann, and Christian Heiliger. Seebeck effect in magnetic tunnel junctions. *Nature Materials*, 10(10):742–746, 2011.

[7] Mikhail Erekhinsky, Fe'lix Casanova, Ivan K. Schuller, and Amos Sharoni. Spin-dependent Seebeck effect in non-local spin valve devices. *Applied Physics Letters*, 100(21):212401, 2012.

[8] S. R. Bakaul, S. Hu, and T. Kimura. Thermal gradient driven enhancement of pure spin current at room temperature in nonlocal spin transport devices. *Physical Review B*, 88(18):184407, November 2013.

[9] E. Saitoh T. Kimura S. Maekawa, S.O. Valenzuela. *Spin Current*. Oxford University Press, Oxford, 2012.

[10] Gerrit E W Bauer, Eiji Saitoh, and Bart J van Wees. Spin caloritronics. *Nature materials*, 11(5):391–9, May 2012.

[11] Benedikt Scharf, Alex Matos-Abiague, Igor Žutić, and Jaroslav Fabian. Theory of thermal spin-charge coupling in electronic systems. *Physical Review B*, 85(8):085208, February 2012.

[12] N.F.Mott and E.A. Davis. *Electronic processes in Non-Crystalline Materials*. Clarendon Press, Oxford, 1979.

[13] J.P. Hermans. . *ACTA PHYSICA POLONICA A*, 2005.

[14] C R Pichard, C R Tellier, and A J Tosser. Thermoelectric power of thin polycrystalline metal films in an effective mean free path model. *Journal of Physics F: Metal Physics*, 10(9):2009–2014, September 1980.

[15] S. Wurmehl, P. J. Jacobs, J. T. Kohlhepp, H. J. M. Swagten, B. Koopmans, S. Maat, M. J. Carey, and J. R. Childress. Local formation of a Heusler structure in CoFeAl alloys. *Applied Physics Letters*, 98(1):012506, 2011.

[16] G. Bridoux, M. V. Costache, J. Van de Vondel, I. Neumann, and S. O. Valenzuela. Enhanced spin signal in nonlocal devices based on a ferromagnetic CoFeAl alloy. *Applied Physics Letters*, 99(10):102107, 2011.

[17] Shaojie Hu and Takashi Kimura. Anomalous Nernst-Ettingshausen effect in nonlocal spin valve measurement under high-bias current injection. *Physical Review B*, 87(1):014424, January 2013.

[18] F. Bakker, a. Slachter, J.-P. Adam, and B. van Wees. Interplay of Peltier and Seebeck Effects in Nanoscale Nonlocal Spin Valves. *Physical Review Letters*, 105(13):1–4, September 2010.

[19] M. Katsnelson, V. Irkhin, L. Chioncel, A. Lichtenstein, and R. de Groot. Half-metallic ferromagnets: From band structure to many-body effects. *Reviews of Modern Physics*, 80(2):315–378, April 2008.

[20] Denis Comtesse, Benjamin Geisler, Peter Entel, Peter Kratzer, and László Szunyogh. Electronic, magnetic and transport properties of full and half-metallic thin film Heusler alloys. *arXiv:1311.1950*, November 2013.

[21] S. Bosu, Y. Sakuraba, K. Uchida, K. Saito, T. Ota, E. Saitoh, and K. Takanashi. Spin Seebeck effect in thin films of the Heusler compound Co_2MnSi. *Physical Review B*, 83(22):1–6, June 2011.

Chapter 7

Novel LSV structures for giant pure spin current generation

7.1 Introduction

Generation and Manipulation of spin current enable to realize the utilization of spin transfer properties in spintronics devices. Lateral spin valve as a conventional spintronics devices could separate charge and spin current and generate pure spin current. The conventional LSVs devices which include one nonferromagnet material and two closed ferromagnets wires are always applied as the study of spin injection, precessing and relaxation. However, such structure suffers one problem of low generation efficiency for the application.

In order to enhance the generation efficient, several approaches have been discussed in the previous chapters, such as utilization of excellent materials (CoFeAl)with high spin polarization and efficient thermally driven spin injection technique. This chapter devotes to the design of the special lateral spin valve structures combined with the excellent materials.

7.2 Multi-terminal lateral spin valves

7.2.1 Multi-terminal lateral spin valve with Py injectors

As we know the pioneer advantage of lateral spin valve is the flexible configuration to generate and manipulate pure spin current. Apart from considering the generation efficiency, the simplest method to enhance the amplitude of the pure spin current is to increase the amount of driven charge current[1–4]. However, the key bottleneck for this technique is the Joule heating in both ferromagnetic (FM) and NM channel, as the spin diffusion length and the spin polarization strongly deteriorate with increasing charge current, resulting in an overall decrease of the pure spin current. Therefore, it's naturally to expand the single injector to multi-injectors which can overcome the issue of the tolerant limitation of charge current.

Figure 7.1 (a) shows the scanning electron microscopy image of multi-terminal lateral spin valve which was fabricated on a SiO_2 substrate by three-step electron beam lithography and lift-off technique. First the four Py injectors (Py1, Py2, Py3 and Py4) width 120 nm width and 60 nm thickness and the detector (Py dot) with an area of 400 nm$\times$200 nm and 10 nm thickness were deposited after first two step electron beam lithography by using electron beam evaporator in ultra low pressure. The Cu channel with 250 nm width and 150 nm thickness was deposited bridge on the Py wires using Joule evaporation. Prior to Cu deposition, the surface of Py wires was carefully cleaned by low power Ar^+ ion milling to get good transparent interface. The performance of this device was evaluated by using lock-in amplifier system with variable DC bias current superimposed on a small AC probing current.

To understand the performance of this device, first each spin signal characteristics of four injectors were observed without DC bias current as shown in figure 7.1(b). All four figures show typical non-local spin valve signal with a high and a low resistance for parallel

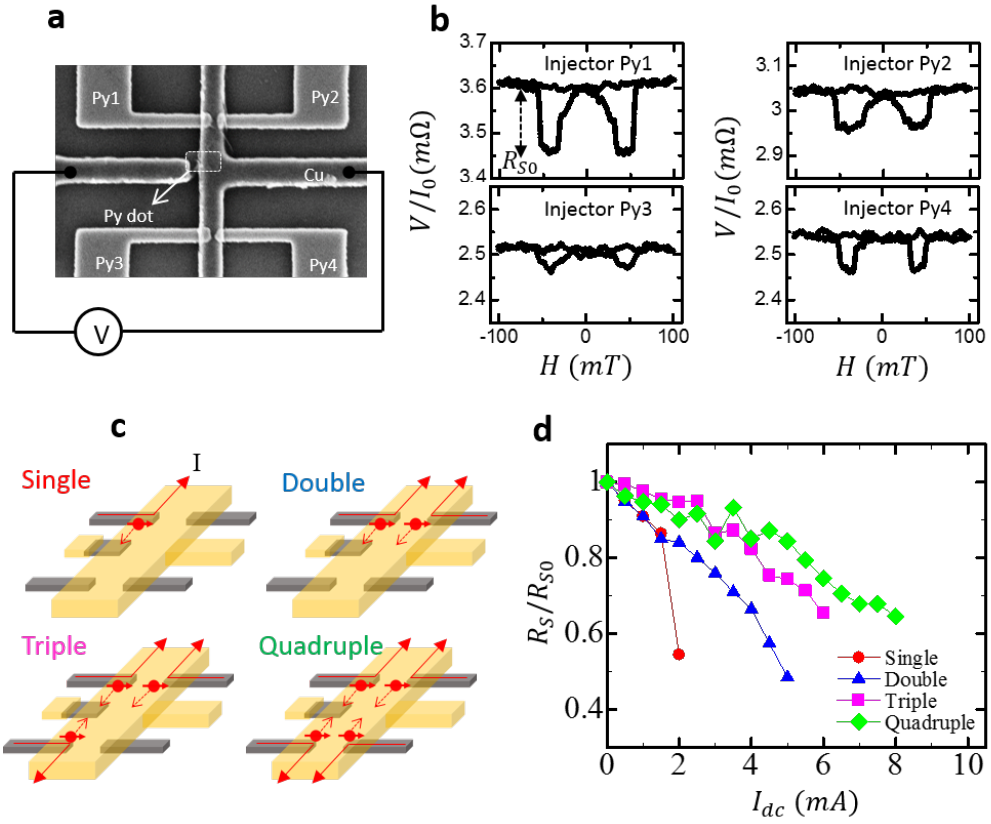

Figure 7.1: (a) SEM image of the multi-terminal spin injection device. (b) Spin signal at near zero bias for each Py injectors. (c) Schematics for signal, double, triple and quadruple spin injections. (d) DC bias current dependence of the normalized spin signals for each injections.

and antiparallel states between the injector's and detector's magnetization. The spin signal resistance R_{S0} is defined as the difference of the two states resistances at zero bias current. However, the magnitude of the spin signal is different with each other. This can be understand by the different size of the injectors and the different distance between the injectors and detector. This indicates our device is well working.

After that, the DC bias current dependent behaviors were evaluated for varying number of injectors as measurement configuration shown in figure 7.1(c). The figure 7.1(d) shows a comparative study of the DC bias dependent performances for different combinations of the injectors. Here, the bias current of spin signals were initialized by R_{S0}. As the DC bias current increases, the ratio of R_{S0}/R_S reduces due to the Joule heating. However, such effect is least pronounced for the case with quadruple injectors. For instance, when single injector is used, at 2 mA the spin signal reduces to 54%. However, the spin spin signal still possesses 95% value of zero DC bias current at this DC bias current injection for the quadruple injectors. The reason is the less heat for the quadruple Py injectors than the single injector under the same total bias current. It can be clearly confirmed that the critical current, where the spin signal starts to reduce, is improved by increasing the number of the spin injectors. Thus, by using a multi-terminal spin injector, the Joule heating problem and electromigration issue in non-local spin injection can be tackled.

7.2.2 Multi-terminal lateral spin valve with CoFe injectors

The spin transfer torque of spin current has been confirmed to be used for writing magnetic bits with high speed and and high density[5–8]. In order to demonstrate the switching of nanomagnet by pure spin current, one multi-terminal spin valve device, which consists of four CoFe injectors and one Py dot detector, has been fabricated on quartz substrate as shown in figure 7.2(a). For utilizing high performance CoFe, one 30 nm CoFe film was prepared by RF magnetic sputtering technique. Then, the 100 width CoFe injector were

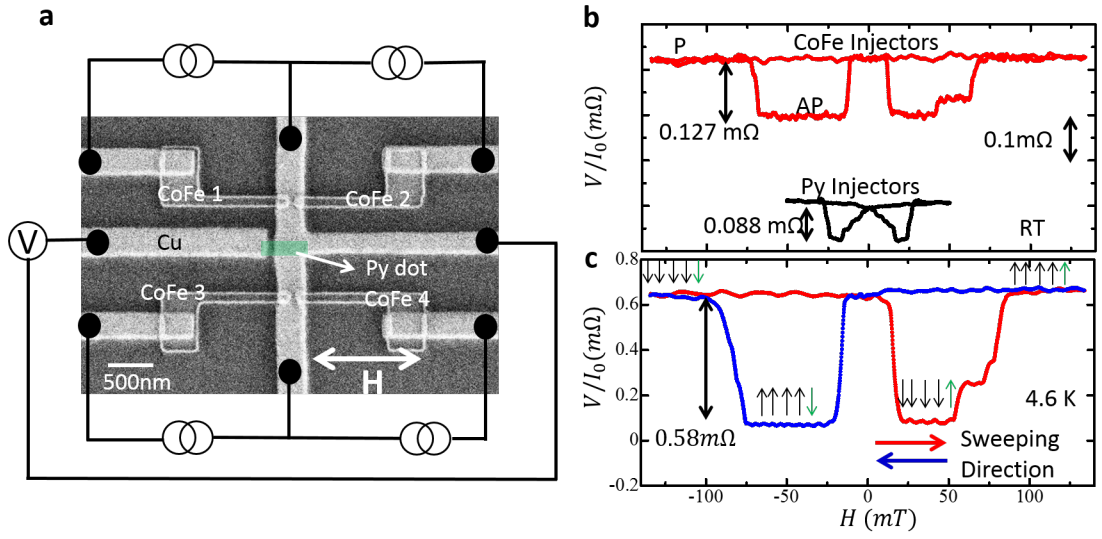

Figure 7.2: (a) SEM image of the multi-terminal spin injection device with CoFe injectors. (b) Quadruple spin signal for CoFe and Py injectors at room temperature. (c) Spin signal at 4.6K for CoFe injectors.

fabricated by using the EBL and Ar^+ ion milling and hot lift-off technique. After that, Py dot with an area of 200 nm × 500 nm and 10 nm thickness was fabricated between the CoFe injectors. Finally, Cu channel with 300 nm width and 160 nm thickness bridged over the injectors. 200 nm × 300 nm area of Py dot has been embedded in the Cu channel for much more spin absorption.

The spin transport properties have been performed by using the standard lock-in amplifier. The spin signals of both Py and CoFe based injectors are plotted at room temperature in figure 7.2(b). Even for long distance and large Py detector dot in CoFe device, the spin signal is about 0.127 mΩ which is still 1.4 times larger than Py injectors device. Further more, the low switching fields which are corresponding to the Py detector are almost same both of CoFe and Py injectors devices. However, the high switching fields which are corresponding to the injectors is quite large for CoFe which have low influence under high bias current. Figure 7.2(c) shows the spin signal which is about 0.58 mΩ at 4.6 K. This indicates

the multi-terminal device with CoFe injectors is an efficient spin current generators. But the magnitude of the pure spin current is still not large enough for the efficient application of spin transfer torque effect.

7.2.3 Multi-terminal lateral spin valve with CoFeAl injectors

Here, we use another multi-terminal device with slightly different sample structure and dimensions as shown in figure 7.3(a). The widths of the Cu and the CoFeAl injectors are 180 nm and 120 nm, respectively. The thicknesses of the Cu and the CoFeAl injectors are 180 nm and 30 nm, respectively. The detector is the elliptical-shaped Py with 10 nm thickness. The major and minor diameters are 300 nm and 150 nm, respectively. The spin signals are 2.8 mΩ at room temperature and 8.45 mΩ at 2.4 K. From the magnitude of the spin signal ΔR_S, we can roughly estimate the injecting spin current. The injecting spin current I_S into the middle Py dot can be calculated by the following equation:

$$I_S = \frac{\Delta R_S}{P_{Py} R_{SPy}} I \tag{7.2.1}$$

By using the value of $\Delta R_S = 8.45 m\Omega$, $I_S = 0.23I$ is obtained. Such efficient pure spin current generation may be applied to switch the magnetization of Py dot. Then the experiment of switching the magnetization of nano-magnet have been operated in the following.

Figure 7.4 (a) shows the illustration of the switching of magnetization by spin transfer torque of pure spin current. Firstly, all the magnetization of CoFeAl and Py dot were initialized by the large negative external field to parallel. If the positive current flows from the CoFeAl wire to Cu, the generated pure spin current with the down spin angular momentum will transfer the spin angular momentum to the middle Py dot. If the magnitude of the pure spin current is large enough, the magnetization of Py dot will be successfully reversed. In order to realize such effect, DC bias current is started to sweep from zero to

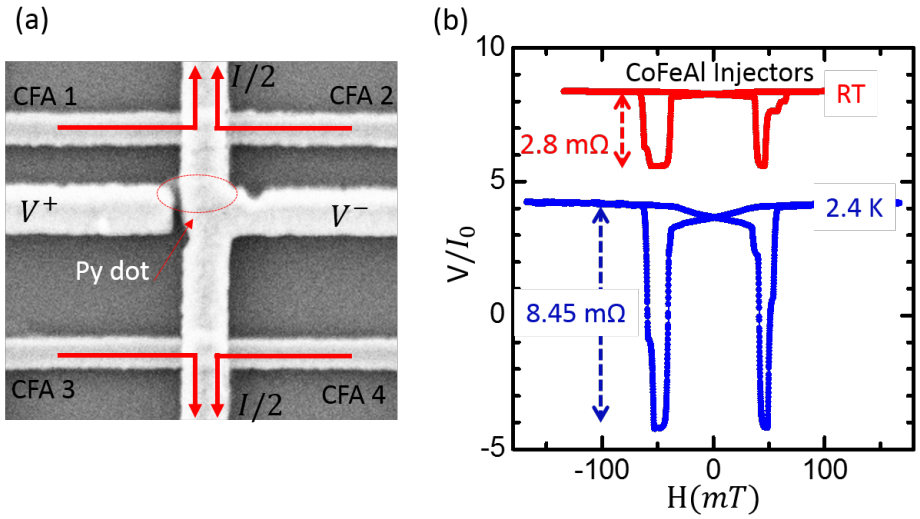

Figure 7.3: (a) SEM image of Multi-terminal lateral spin valve with CoFeAl injectors and the measurement configuration. (b) Typical nonlocal spin signal at room temperature and 2.4 K.

positive value and go back to negative value, then reduce to zero. The resistance jumping was observed at the +7.3 mA as shown in figure 7.4 (b). However, we couldn't reverse the magnetization back by using the negative bias current. In the Chapter 4, the bias current dependence of spin signal had been systemically evaluated. The positive bias current could generated additional spin current by joule heating effect and enhance the total magnitude of pure spin current. However, the negative bias current will reduce the total magnitude of pure spin current. This partial switching effect could be easily understood by considering the thermally driven spin injection.

Otherwise, only partial Py dot is explored in the pure spin current and the embedded part of Py is a bit thin because of the pre-milling process before depositing Cu. The existing no uniform domain may also influence the switching Py dot. So optimized designment is needed in the future work.

All in all, we realized the switching of magnetization for nanomagnet by efficient pure spin current in multi-terminal device with CoFeAl injectors.

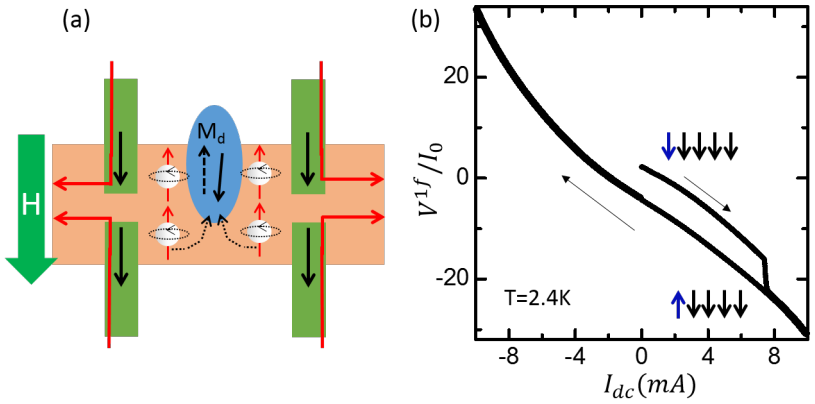

Figure 7.4: (a) Illustration of the switching of magnetization by spin transfer torque of pure spin current. (b) Resistance jumping as sweeping DC bias current at the temperature of 2.4 K. DC bias current is started to sweep from zero to positive value of 10 mA and go back to negative 10 mA, then reduce to zero.

7.3 Nanopillar based lateral spin valves

7.3.1 Fabrication of Nanopillar with different materials

One approach to efficiently produce a pure spin current is non-local spin injection by employing lateral spin valve combined with nanopillar structures. These kind lateral spin valves can over come the limitation of maximum tolerance bias current because of short current pass in ferromagnet. The disturbing effects, such as conventional thermoelectron effect and anomalous nernst effect, can be sufficiently prevented at the detector owing large heat sink of the bottom electrode. However, in the previous device which has been fabricated from a ferromagnetic (F) and nonmagnetic (N) bilayer film, it is impossible to make the injector and detector with different materials. To further explore new functionalities of pure spin current, we have developed a novel method for fabricating nanopillar-based lateral spin valve (LSV) consisting of two ferromagnetic dots with different materials and thicknesses. One high spin polarized CoFeAl and one typical soft magnet Py have been chosen in the present studies.

We employ the shadow evaporation techniques to make the novel LSV[1, 9]. First, the electron beam lithography (EBL) was performed to make Π structure patterned in the organic resist as shown in the figure 7.5(a) in the top view. The thickness of the coating resist depends on the viscosity and concentration of solution. After carefully checking, two times coating with 2000 rpm can obtain 1μ m thickness resist. After that, 150-nm-thick Cu bottom film was perpendicularly deposited to the substrate using thermal evaporation. Then, two different and closely located ferromagnetic ribbons (CoFeAl and NiFe) were deposited at different angles on Cu wire without breaking the vacuum as schematically shown in Figure 7.5(b). In this experiment, 12 nm CoFeAl and 10 nm Py films were deposited using electron beam evaporation deposition under the pressure of 10^{-6} Pa. In order to prevent the oxidation of ferromagnetic film, finally 10 nm Cu film deposited on the top layer. One SEM image of closed located ribbons is shown in figure 7.5(c) after lift-off. The nanopillars were fabricated by two steps lithography. Two rectangles resist mask had been fabricated on the two ribbons by the first step electron beam lithography. After Ar^+ ion milling off the extra ferromagnetic film, SiO_2 as isolator layer was deposited to insolate the bottom electrode with pillar. The top electrodes were fabricated after removing resist mask using second step EBL and conventional lift off processes. One final SEM device was shown in figure 7.5(d). Here, the interval distance of the tow dots is 850 nm from the center to center. The area of the dots are design as 150 nm $\times$ 300 nm. The device performances of the spin transport were evaluated by measuring the nonlocal spin signal with the measurement configuration shown in figure 7.5.

7.3.2 Evaluation of nonlocal spin transport

Figure 7.6(a) shows one clearly typical lateral spin valve signal in which the high and low resistances correspond respectively to the parallel (P) and the antiparallel (AP) magnetizations of injector and detector. The distinguished switching field (H_C) for the two dots

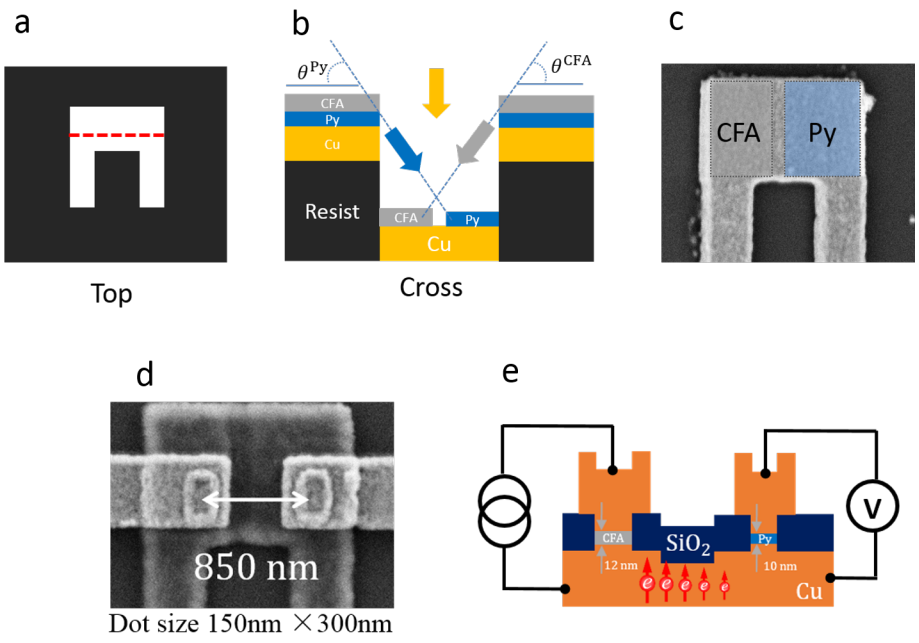

Figure 7.5: Fabrication process and measurement method (a) Top view of the resist pattern. (b) Schematic of shadow evaporation in a view of the crossing section. (c) SEM of the closed located ribbons. (d) SEM image of one device (e) Schematic of the measurement configuration

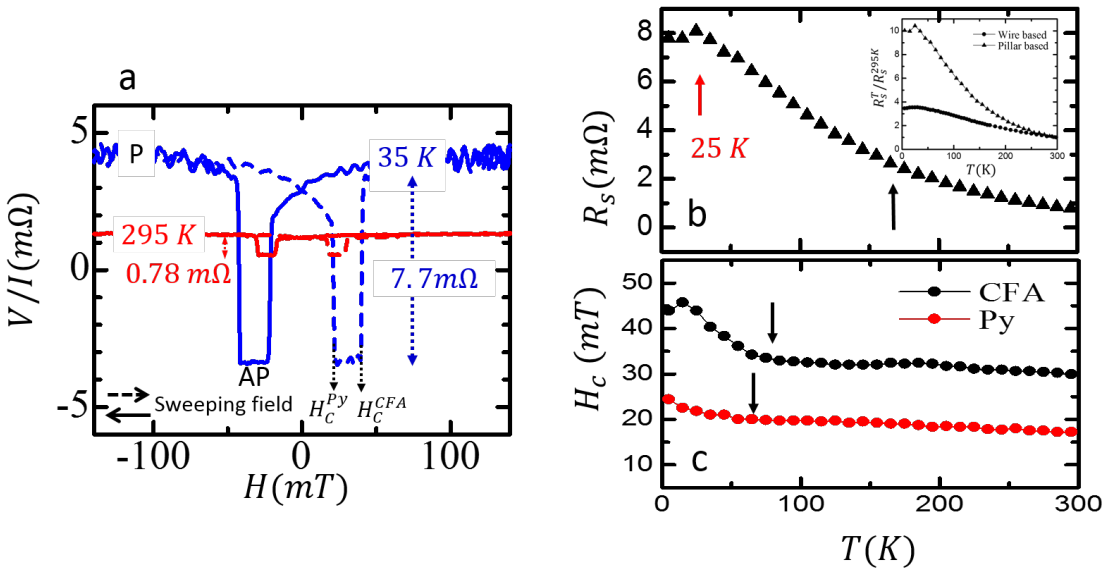

Figure 7.6: (a) Typical spin signal for the present device measured at 295 K (red) and 35 K (blue). (b) The spin signal as a function of temperature. (c) Switching field as a function of temperature for CFA (Solid black dot) and Py (Solid red dot) respectively.

come from the different anisotropy of CoFeAl and Py. The spin signal (R_S) which is the overall resistance difference between the two states is bout 0.78 mΩ at 295 K and 7.7 mΩ at 35 K. The spin signal is strongly enhanced at low temperature. The curve of temperature dependence of spin signal was plotted in figure 7.6(b). One maximum value of 8.1 mΩ was observed at 25 K, which can be explained by the spin-flip scattering of the surface. In the one dimension model, the spin signal is mainly dominated by spin polarization of spin injector and detector and the spin diffusion length in Cu. In order to understand the picture of temperature dependence of polarization, the switching field as a function of temperature , which corresponds the polarization of ferromagnet, are shown for CFA and Py dots in figure 7.6(c). The switching fields are rapidly increasing, when temperature starts to decrease from 65 K. However, the spin signal is dramatically enhanced from 165 K. This indicates the spin diffusion length dominates the enhancement of spin signal from 165 K,

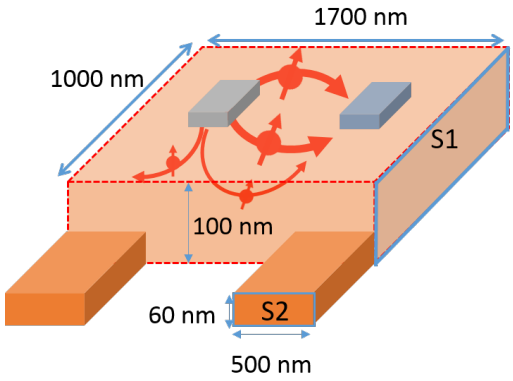

Figure 7.7: The illustration of the spin reservoir effect in the pillar based lateral spin valve.

not the polarization. The inset of figure 7.6(b) shows the normalized value of spin signal as a function of temperature for wire based (solid dot curve) and pillar based (solid triangle dot) spin valve, respectively. The normalized value is separated when the temperature reduces. This indicates our pillar structure bears unique properties at the low temperature. As mentioned, this may mainly arise from the enhanced effective spin diffusion length.

In order to explain how does the spin diffusion length work, the spin reservoir will be introduced. Figure 6.6 shows a schematic image of present device. The dimension of the reservoir box which is defined as the volume in red dash lines is shown as width of 1000 nm, length of 1700 nm and thickness of 100 nm. Since the very thin two probes channels have much larger spin resistance, the generated spins prefer to propagate in the low spin resistance channel. When the spin diffusion length is longer than the value of geometry dimensions, the efficient spin diffusion length will be enhanced because of the reflection of wall.

7.4 Summary

To summarize, we have investigated two special configurations of nonlocal spin devices, named as multi-terminal and nanopillar nonlocal devices. The key motivation for exploring

these novel configurations is to improve the spin injection efficiency by tackling the Joule heating problem. It has been demonstrated that by increasing the number and reducing the effective size of the spin injector electrodes, the Joule heating can be significantly circumvented and, thereby, a large spin signal can be generated without sacrificing the efficiency at high bias current. We also emphasize that, by using a material with high spin polarization as the spin injector, the generation efficiency of the pure spin current can be drastically improved. By combining these techniques, the generation efficiency of the pure spin current might be improved to a comparable level to that of the spin polarized current in the vertical device. Thus, the nonlocal device configurations discussed in this article are promising for implementing the pure spin current in a useful device and demand further attention from the research community.

Bibliography

[1] Tao Yang, Takashi Kimura, and Yoshichika Otani. Giant spin-accumulation signal and pure spin-current-induced reversible magnetization switching. *Nature Physics*, 4(11):851–854, October 2008.

[2] Andrew T McCallum and Mark Johnson. Film edge nonlocal spin valves. *Nano letters*, 9(6):2350–3, June 2009.

[3] J. Z. Sun, M. C. Gaidis, E. J. OSullivan, E. a. Joseph, G. Hu, D. W. Abraham, J. J. Nowak, P. L. Trouilloud, Yu Lu, S. L. Brown, D. C. Worledge, and W. J. Gallagher. A three-terminal spin-torque-driven magnetic switch. *Applied Physics Letters*, 95(8):083506, 2009.

[4] S. Nonoguchi, T. Nomura, and T. Kimura. Nonlocal spin transports in nanopillar-based lateral spin valve. *Applied Physics Letters*, 100(13):132401, 2012.

[5] M. Stiles and A. Zangwill. Anatomy of spin-transfer torque. *Physical Review B*, 66(1):014407, June 2002.

[6] Igor Žutić and S. Das Sarma. Spintronics: Fundamentals and applications. *Reviews of Modern Physics*, 76(2):323–410, April 2004.

[7] D.C. Ralph and M.D. Stiles. Spin transfer torques. *Journal of Magnetism and Magnetic Materials*, 320(7):1190–1216, April 2008.

[8] Jean-Yves Bigot, Mircea Vomir, and Eric Beaurepaire. Coherent ultrafast magnetism induced by femtosecond laser pulses. *Nature Physics*, 5(7):515–520, May 2009.

[9] Y. Ji, A. Hoffmann, J. S. Jiang, and S. D. Bader. Spin injection, diffusion, and detection in lateral spin-valves. *Applied Physics Letters*, 85(25):6218, 2004.

Chapter 8

Conclusion

This thesis devotes to experimentally study on the electrically and thermally driven spin-dependent transport properties in ferromagnet/nonferromagnet hybrid nanostructures with the purpose to enhance the generation efficiency of pure spin current. The major results of the thesis are as follows:

Influence of heat current on the transport of spin current.

The bias current dependence of nonlocal spin valve effect has been systematically investigated in Py/Cu LSVs. The large bias current is found to induce both the reduction of spin valve effect and the unconventional magnetic-field-dependent features. The former can be understood by the reduction of the spin diffusion length of the Cu channel caused by the Joule heating. Later can be explained by the anomalous Nernst-Ettingshausen effect induced by the heat current in the detected probe. Thus the heat current is important on the spin transport.

Efficient pure spin current generation using CoFeAl/Cu LSVs. CoFeAl with a specific alloy composition shows an excellent ferromagnetic materials for the electrical spin injection in LSVs. The CoFeAl/Cu LSVs can be fabricated by the conventional lift-off technique similarly to the Py/Cu LSVs. the spin valve effect obtained in the CoFeAl/Cu LSV is 10 times larger than those for the Py/Cu LSV, indicating the high efficient generation of pure spin current.

Moreover, the obtained thermal spin voltage is approximately 100 times more than the conventional injector at room temperature using such excellent CoFeAl alloy because the spin-dependent seebeck coefficient is larger than the conventional charge seebeck coefficient due to the favourite band structure. This leads to the development of an innovative method for simplifying device integration without the need for electricity, namely wireless spintronics.

Enhancement of pure spin current by mixing the electrical and thermal generation. Here, the nonlocal spin valve effect has been evaluated under bias current in CoFeAl/Cu LSV. The nonlocal spin signal is found to increase monotonically with the bias current. From the analysis based on one dimensional spin diffusion model with considering the bias current heating effect, the contribution of the thermal spin injection is much larger than the influence of the reduction of spin diffusion length in Cu channel. This indicates heat current could enhance the generation of pure spin current.

Giant pure spin current generation in novel device structures. Two kinds of novel device structures have been developed. One is a multi-terminal spin injection, in which the totally generated spin can be extended by mixing the spin currents generated from each spin injector. The divided spin injection was found to reduce the heating effect. The other one is a nano-pillar based LSV, in which a large excitation current can flow. To further explore new functionalities of pure spin current, LSVs consisting of two ferromagnetic dots with different materials and thicknesses have been successfully developed.

In briefly, Permalloy has a limitation for generating the large pure spin current because of the undesired heating effects. To overcome this serious obstacle, the CoFeAl alloy has been developed with the high spin polarization. An efficient generation of pure spin current has been realized by using the CoFeAl alloy. Moreover, the CoFeAl is found to have an extremely large spin-dependent Seebeck effect. This enables us to develop the highly efficient thermal spin injection in lateral spin valves. The novel device structures have been developed for

increasing the generation efficiency and the magnitude of the spin current. These innovative demonstrations provide important steps toward the practical application of the pure spin current.

Research Activities

Journal Publications

1. Shaojie Hu, Takashi Kimura. "Significant modulation of electrical spin accumulation by efficient thermal spin injection." Phys. Rev. B 90, 134412 (2014).

2. Shaojie Hu, Hiroyoshi Itoh, Takashi Kimura. "Efficient thermal spin injection using CoFeAl nanowire." NPG Asia Materials, 6, e127 (2014).

3. Xiaomin Cui, Shaojie Hu, Takashi Kimura. "Detection of a vortex nucleation position in a circular ferromagnet using asymmetrically configured electrodes." Appl. Phys. Lett. 105, 082403 (2014).

4. Saidur Bakaul, Shaojie Hu, Takashi Kimura. "Thermal gradient driven enhancement of pure spin current at room temperature in nonlocal spin transport devices." Phys. Rev. B 88, 184407 (2013).

5. Congpu Mu, Shaojie Hu, Janbo Wang, Takashi Kimura. "Thermo-electric effect in a nano-sized crossed Permalloy/Cu junction under high bias current." Appl. Phys. Lett. 103, 132408 (2013).

6. Shaojie Hu and Takashi. Kimura. "Anomalous Nernst-Ettingshausen effect in non-local spin valve measurement under high-bias current injection." Phys. Rev. B 87, 014424 (2013).

7. Saidur Bakaul, Shaojie Hu and Takashi Kimura. "Large pure spin current generation in metallic nanostructures." Appl Phys A, 339, 7495 (2012).

8. Shaojie Hu, K. Kiseki, S. Yakata and T. Kimura. "Ferromagnetic resonance in exchange-coupled NiFe/FeMn films and its control." IEEE Trans. on Magn. 48 , 2889 - 2891 (2012).

Conference Presentations

1. Shaojie Hu, Takashi Kimura, Efficient lateral spin valve device consisting of different ferromagnetic nanopillars (Poster), The 15th International Union of Materials Research Societies, International Conference in Asia, Aug. 24-30, Fukuoka, Japan

2. Shaojie Hu, Takashi Kimura, Significant modulation of electrical spin accumulation by efficient thermal spin injection (Accompany), Seminar in JAEA, March 24-25, Tokai, Japan

3. Shaojie Hu, Takashi Kimura, Efficient thermal spin injection using CoFeAl injectors (Oral) International Symposium on Advanced Nanodevice and Nanotechonlogy (ISANN2013), December 8-13, 2013, Hawaii, USA.

4. Shaojie Hu, Takashi Kimura, Giant thermal spin accumulation in NLSV structure using CoFeAl/Cu interface at room temperature (Oral) 58th annual conference on magnetism and magnetic materials (MMM 2013), November 4-8, 2013, Denver, Colorado, USA.

5. Shaojie Hu, Takashi Kimura, Asymmetric field dependence of nonlocal spin valve signal under high bias current injection(Poster) The 8th International Symposium on Metallic Multilayers (MML2013), May 19-24, 2013,Kyoto Research Park, Kyoto, Japan.

6. Shaojie Hu, Takashi Kimura, Giant pure spin current generation in non-local lateral spin valve structure by using multi-terminal injectors (CoFe) (Poster) The 68th Annual Meeting, The Physical Society of Japan, March 26-29, 2013 Hiroshima, Japan.

7. Shaojie Hu, Takashi Kimura, Improvement of generation efficiency of pure spin current using multi-terminal spin injection (Poster) The 21th International Colloquium on Magnetic Films and Surfaces(ICMFS2012) September 24-28, 2012, Shanghai, China

8. Shaojie Hu, Takashi Kimura, Improvement of generation efficiency of pure spin current using multi-terminal spin injection (Poster), The 19th International Conference on Magnetisim (ICM) with Strongly Correlated Electron Systerms (SCES) July 8-13,2012 Bexco, Busan Korea

9. Shaojie Hu, Takashi Kimura, Possibility for ferromagnetic resonance control using exchange-coupled NiFe/FeMn film (Poster). The International Magnetics Conference, INTERMAG 2012, May 7-11, Vancouver, Canada.